The development of a Compton camera for the imaging of gamma rays in the energy range 0.662 MeV to 6.130 MeV

Thesis submitted in accordance with the requirements of the University of Liverpool for the degree of Doctor of Philosophy

by

Martin Jones

Oliver Lodge Laboratory

2013

Acknowledgments

First and foremost I would like to thank Prof. Paul Nolan and Dr Andy Boston for giving me the opportunity to study with the Nuclear Physics group at the University of Liverpool. Without them and the E.P.S.R.C this PhD position would not have been available.

I want to thank all of my new friends and colleagues within the NPG who have made this possible and kept me levelled during my time in the group. Particularly I want to thank Carl, Ren, Grinto, Scraggo, Gaffney and Oxley who have all since left the country but it is great to stay in touch and hear all about your new ventures. Heidi, Eddie, John T, Sam, Anthony, Jamie, Bahadr, Mark, Fay, Slee, Sapple, Rob, John R, thank you all for the football, beer, lunches, Christmas parties and numerous nights out. I will remember them forever.

Dan Judson - You sir are an incredibly patient human being, you have helped me more than I could ever explain and without your physics, proof reading and programming knowledge this thesis wouldn't even be anywhere near this position. The whiskey is on me for the forseeable future.

Laura Harkness - What can I say? OK you support Man Utd but I think I can let that go. You have been a great friend throughout, you always believed I could do it and we have plenty more cake times ahead. Thank you so so much.

Ben Pietras - Even from Spain you have helped me more than I can thank you. Living with you was an honour, even with that wretched yellow dressing gown.

John Lynch - All I can say is WOW. You mate are a true hero. Whilst I was here worrying over a piece of paper you were fighting for Queen and country, risking your life for our greater good. You are an incredible human being and such a good friend.

James Convery (And Caz) - For every minute we shared throughout our University adventures, beers shared, dinners cooked (for me), Phone calls when you went travelling. You have always been there from the start and I will never forget it. I wish I could work even a little as much as you do. You are a massive inspiration.

Keeping the most important until the end, thank you to my entire family. To my

Mum, Nan, Grandad, Amanda, David, Jason and my little man Ross, your support is what keeps me going.

And finally, Emma, without you, this last 12 months certainly would not have been possible and I know without your patience, love, guidance and support I wouldn't have got this finished. I look forward to being inspired by you for years to come. Thank you so much.

"If at first you don't succeed, try, try, try again"

William Edward Hickson

Abstract

Experimental and GEANT4 simulated Compton camera images and results are presented. This thesis aims to assess the contrasting performance of two seperate detector configurations which include a two germanium Compton camera (GeGe) and a germanium caesium iodide (GeCsI) Compton camera. GEANT4 software has previously been validated. All images were reconstructed using an existsing image reconstruction algorithm which utilises a simple back projection method.

A range of experimental data were collected using a number of radioactive sources to assess the current limitations of such a device. These included, a 0.267 MBq 0.662 MeV ^{137}Cs gamma-ray point source and a 0.060 MBq 1.173 MeV and 1.332 MeV ^{60}Co gamma-ray point source. The results presented in this thesis show that the image FWHM of ^{137}Cs improves in X and Y as a function of detector separation from 26.9 $\pm$ 5.0 mm and 25.5 $\pm$ 5.0 mm at 30mm detector separation to 17.5 $\pm$ 5.0 mm and 16.7 $\pm$ 5.0 mm at 100mm detector separation. The image FWHM in X and Y of ^{60}Co improves from 34.8 $\pm$ 5.0 mm and 35.3 $\pm$ 5.0 mm to 21.9 $\pm$ 5.0 mm and 21.9 $\pm$ 5.0 mm at 100mm detector separation. The gamma-ray point sources were positioned across at the top left corner of the detector face and an assymetrical shape was seen throughout the images. ^{137}Cs improves from 32.1 $\pm$ 5.0 mm and 32.6 $\pm$ 5.0 mm at 30mm detector separation to 28.1 $\pm$ 5.0 mm and 23.9 $\pm$ 5.0 mm at 100mm detector separation. The image FWHM in X and Y of ^{60}Co improves from 41.6 $\pm$ 5.0 mm and 45.4 $\pm$ 5.0 mm to 29.6 $\pm$ 5.0 mm and 28.6 $\pm$ 5.0 mm at 100mm detector separation. It was not understood whether this was due to the physics due to detector and source positioning or attributed to the experimental analysis.

GEANT4 simulated data were taken to replicate and assess the two detector configuration performance for the GeGe system to compare with experimental results. The GeGe results and Compton images show an improved image FWHM as a function of detector separation for 0.662 MeV and 1.332 MeV. For 0.662 MeV the image FWHM

in X and Y improves from 18.1 ± 2.0 mm and 18.8 ± 2.0 mm at 30mm detector separation to 12.6 ± 2.0 mm and 12.8 ± 2.0 mm at 10mm. For 1.332 MeV the image FWHM in X and Y improves from 18.8 ± 2.0 mm and 20.6 ± 2.0 mm at 30mm detector separation to 12.5 ± 2.0mm and 13.5 ± 2.0 mm. The image FWHM values are lower than that of the experimental values due to the interaction positions within the detector being exactly defined. Experimentally the image FWHM is higher, this is attributed to not knowing the exact interaction positions within the detectors. This could be rectified in the future by introducing the method of parametric pulse shape analysis. Further GEANT4 simulated data were taken to directly compare the performace of a GeGe and a GeCsI configuration over a range of energies. These were 0.662 MeV to 6.130 MeV. The image FWHM and Compton efficiency of GeGe and GeCsI Compton cameras have been compared as a function of increasing detector separation. The Compton efficiency measurements show that a GeCsI Compton camera system is consistently more efficient as the detector separation increases. At 0.662 MeV the number of 1:1 events for GeCsI at 30mm detector separation is 30,016 compared to 14,956 for GeGe, to 10,817 for GeCsI at 100mm compared to 3,751 for GeGe. The image resolution over the range of gamma-ray energies does not significantly degrade when comparing GeCsI to GeGe but at much higher energies and 30mm and 50mm detector separation the image FWHM performance of GeCsI is not as similar in X and Y, seen by the assymetrical shape of the images. For 6.130 MeV the image FWHM in X and Y is 28.8 ± 2.0mm and 19.9 ± 2.0 mm at 30mm detector separation and 12.6 ± 2.0 mm and 18.9 ± 2.0mm at 50mm detector separation.

Contents

List of Figures

List of Tables

Chapter 1

Introduction

The main focus of this thesis is to examine the performance of High-Purity Germanium (HPGe) and Caesium Iodide (CsI) detectors in the area of Compton Imaging over a range of gamma-ray energies. Semiconductor devices have been widely used in nuclear imaging and in particular, homeland security [Vet07]. This thesis will assess the potential of a HPGe Compton Camera system and directly compare its performance with a HPGe - CsI Compton Camera.

1.1 Nuclear Imaging

Over the past two decades a lot of work has been done trying to develop new Compton imaging systems with improved energy and image resolution for homeland security and nuclear imaging applications. Work by [Vet07] [Mih09] shows the latest developments in this area using HPGe and Silicon (Si) semiconductor systems, yet are only imaging up to 2.6 MeV. Due to their unparalleled energy resolution, HPGe and other semiconductor detector systems have been utilised, yet the development of a Compton imaging system is limited by their efficiency at high energies. Significant work has also been done with Cadmium-Zinc-Telluride (CZT) detectors by [Leh03], [Du01], [Wah11], with the ability to image up to 3 MeV yet are once again limited by the efficiency at high energies. Earlier work by [Gur95] and [Gur96] uses scintillator

detector systems for Compton imaging, using Sodium Iodide (NaI) and Caesium Iodide (CsI) in their work, showing increased sensitivity but only look at energies up to 810 keV and 1 MeV respectively. The increased efficiency of a CsI detector in Compton imaging is highly desired and key for the work in this thesis. What isn't known experimentally is the ability of such a device at energies beyond 1 MeV. Throughout this thesis, energies between 0.662 MeV and up to 6.130 MeV are discussed and the ability of such a device to image these energies is tested.

1.2 The Distinguish project

The detection and identification of hazardous materials has become increasingly important in the last decade. The Distinguish collaboration aimed to develop a technique which is capable of detecting and imaging illicit substances such as explosives or narcotics hidden in luggage and vehicles in transit. Current systems such as X-ray imaging devices which are used in airports provide the user with a high level of shape and density information of objects contained within luggage or cargo yet do not provide the user with any nuclide identification. Figure 1.1 shows a typical X-ray image at an airport which shows limited specificity. Distinguish would utilise neutron interrogation of the substances under investigation exploiting the inelastic scattering of the neutrons and after neutron activation characteristic gamma rays are emitted. Pulsed fast neutron analysis (PFNA) [Vou01] [Ryn99] is utilised by using a collimated beam of 14MeV fast neutrons to excite the nuclei of common elements in the materials under investigation. The neutrons will interact via inelastic scattering with Carbon, Oxygen and Nitrogen which stimulates the emission of the characteristic gamma rays. The energies which correspond to the light elements are, (Oxygen - $E_\gamma = 6.130$ MeV, Carbon - $E_\gamma = 4.430$ MeV, Nitrogen - $E_\gamma = 1.640$ MeV, 2.310MeV and 5.110 MeV) [Goz94]. These are normally used as primary components of explosive materials. Current systems that are able to image gamma rays of such energies are gamma cameras which are based on the principle of the Anger camera. [Ang64].

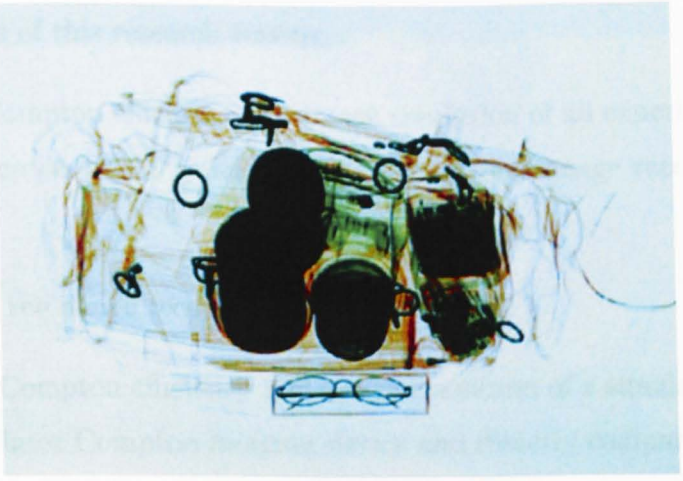

Figure 1.1: Typical X-ray image of luggage which shows the limitations of the system. Many areas in the X-ray image are not defined.

It is important to precisely measure the elemental concentrations in an object but it is also important to be able to directly image the contents and localise their position as accurately as possible. This is possible by using a Compton camera and utilising the Compton imaging technique. Compton imaging is discussed in detail in Chapter 3. The Distinguish project was a collaboration between Liverpool and Lancaster Universities with some industrial input from the Manchester airport group. The work in this thesis was a part of this project.

1.3 Thesis aims

The primary aim was to look at the ability of a Compton camera system to image high energy gamma rays in the energy range 0.662 MeV to 6.130 MeV. The work utilises the Compton imaging technique to generate images using two different detector setups and to assess the image resolution, sensitivity and limitations of a HPGe - HPGe system and directly compare the results with a HPGe - CsI system. Currently available detectors allowed experimental measurements to be taken with two HPGe detector systems.

The main focus of this research was to:

- Asess the Compton efficiency and image resolution of an experimental semiconductor Compton imaging device using the current image reconstruction algorithm.
- Investigate the image reconstruction limitations.
- Assess the Compton efficiency and image resolution of a simulated semiconductor - scintillator Compton imaging device and directly compare with simulated results of a semiconductor Compton imaging device using the current image reconstruction algorithm.

1.4 Chapter content

Chapter 2 discusses the principles of radiation detection which gives a good understanding of the work done in this thesis. Chapter 3 discusses the detailed principle of Compton Imaging and covers the limiting factors that contribute to detector performance and image resolution, the ability of an analytical reconstruction algorithm and the projection method used. Chapter 4 outlines the experimental work which is needed to understand the performance of an existing system, including a detailed report of all experimental results using a range of radiation sources over a range of distances and an increasing detector separation. Chapter 5 introduces the GEANT4 simulation toolkit and discusses the results of simulated Compton imaging devices at lower energies, comparing the performance of a HPGe - HPGe system with a HPGe - CsI system. Chapter 6 discusses the Compton imaging of intermediate gamma ray energies. Chapter 7 discusses the Compton imaging of high energy gamma rays and finally Chapter 8 concludes the thesis including the future prospects of the project.

Chapter 2

Principles of radiation detection

The operation of many gamma-ray detectors is based on the production of an electrical signal that is proportional to the energy deposited in the detector. Fundamental knowledge of the interaction mechanisms of gamma rays is needed to understand the detector response. This chapter will detail the mechanisms in which gamma-rays interact with matter, detector response and the parameters used to establish the detector performance in both semiconductor and scintillator detector devices.

2.1 Photon interactions with matter

Photons interact with a material by the transfer of part or all of their energy to atomic electrons. There are three main interaction processes through which this occurs. They are photoelectric absorption, Compton scattering and pair production. These mechanisms dominate in the energy range of $\sim$10 keV to $\sim$10 MeV.

2.1.1 Photoelectric absorption

A gamma ray interacts via photoelectric absorption when the incident photon transfers all of its energy to a bound electron. This electron is ejected from the atom and termed the photoelectron creating an ionised absorber atom with a vacancy usually in its K-shell. This vacancy is quickly filled by the capture of a free electron from the

medium that the interaction took place, or by a rearrangement of the electrons from the outer orbitals in the atom. The gamma-ray energy is entirely absorbed in this process. The photoelectron appears with an energy given by Equation 2.1,

$$E_e = E_\gamma - E_b, \tag{2.1}$$

where E_e is the energy of the photoelectron, E_b is the binding energy of the atomic electron and E_γ is the energy of the incident photon. This process is schematically illustrated in Figure 2.1. The cross section for a gamma ray undergoing photoelectric absorption is dependent on the Z value of the absorber atom and the energy of the gamma ray and is given by Equation 2.2,

$$\sigma = k\left(\frac{Z^n}{E_\gamma^m}\right), \tag{2.2}$$

where n is dependent on the incident gamma-ray energy and varies between 4 and 5, k is a constant and m is 3.5 [Kno00].

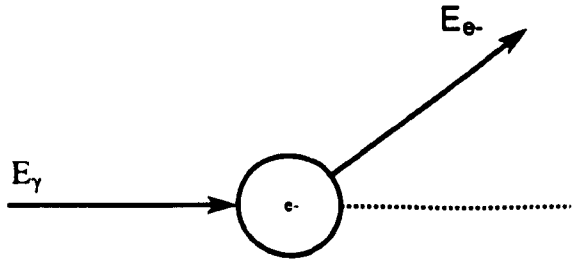

Figure 2.1: Schematic illustration depicting photoelectric absorbtion. The incoming gamma ray interacts with a bound electron creating a photoelectron. The gamma-ray energy E_γ is entirely absorbed.

2.1.2 Compton scattering

Compton Scattering is the process by which a gamma ray gives up part of its energy by interacting with an atomic electron within a material [Kno00]. The recoil electron is ejected and the scattering of the photon will range from 0° to 180°. The amount of energy which is transferred to the electron from the incident photon is related to the scattering angle. The cross section of Compton scattering per atom of the absorber material depends on the number of electrons available as scattering targets and therefore will increase linearly with Z. The relationship between the incoming photon energy (E_γ), the photon energy after scattering ($E_{\gamma'}$) and the scattering angle is given by Equation 2.3,

$$E_{\gamma'} = \frac{E\gamma}{1 + \frac{E\gamma}{m_0c^2}(1 - cos\theta)}, \tag{2.3}$$

where θ is the scattering angle, E_γ is the incident photon energy, $E_{\gamma'}$ is the energy of the photon after the interaction with the electron and m_0c^2 is the rest mass of the electron. Compton scattering is illustrated schematically in Figure 2.2.

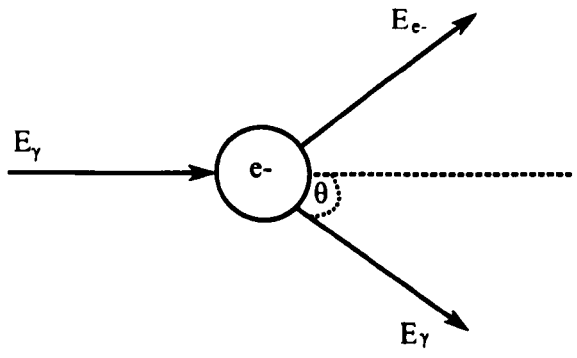

Figure 2.2: Schematic illustration depicting Compton scattering. The incoming gamma ray E_γ interacts with an atomic electron. A recoil electron E_{e^-} is ejected and the photon scatters through an angle θ depositing part of its energy. The amount of energy deposited is related to the scattering angle.

The differential Compton scattering cross section can be described via the Klein-Nishina distribution [Kno00]. This is used to predict the angular distribution of scattered gamma rays at given energies,

$$\frac{d\sigma}{d\Omega} = Zr_0^2 \left(\frac{1}{1+\alpha\,(1-cos\theta)} \right)^2 \left(\frac{1+cos^2\theta}{2} \right) \left(1 + \frac{\alpha^2\,(1-cos\theta)^2}{(1+cos^2\theta)\,[1+\alpha\,(1-cos\theta)]} \right), \tag{2.4}$$

where r_0 is the classical electron radius, Z is the atomic number and $\alpha = h\nu/m_0c^2$. The differential Compton scattering cross section is illustrated by the polar plot in Figure 2.3. It is clear to see that as the energy of the incident photon increases there is a greater likelihood of forward scattering.

2.1.3 Pair-production

Pair production is energetically possible when gamma rays have a minimum energy of 1.022 MeV [Kno00]. In this process the gamma ray interacts in the Coulomb field of the nucleus and a complex set of interactions occur. The gamma ray is converted into matter in the form of an electron-positron pair that has a rest mass of 1.022 MeV.

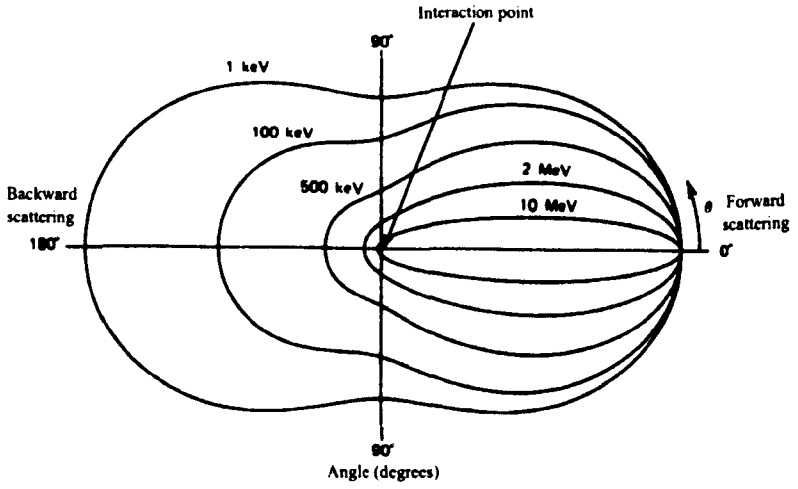

Figure 2.3: Polar plot showing the Compton scattering cross section against scattering angle over a range of gamma-ray energies. Forward scattering is shown to be more likely at higher energies [Kno00].

The electron-positron pair share any additional energy of the gamma ray as kinetic energy. The positron annihilates with a bound electron producing two back to back 511keV photons. This is given by equation 2.5 and illustrated in Figure 2.4.

$$E_{e^-} + E_{e^+} = E_\gamma - 2m_0c^2. \tag{2.5}$$

Figure 2.5 shows the relative importance of each of the three main interaction processes. The curve $\sigma = \tau$ indicates the energy at which photoelectric absorption and Compton scattering are equally as likely as a function of Z. The $\sigma = \kappa$ curve shows the energy where Compton scattering and pair production are equally likely. The energy range which Compton scattering dominates in germanium is between ~150keV and ~9MeV, as illustrated by the dotted lines in Figure 2.5 at Z=32. This is important as germanium is used as the scattering medium in this work and the

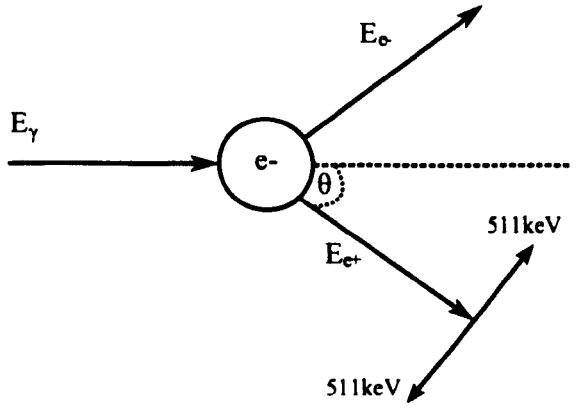

Figure 2.4: Schematic illustration depicting pair production. After initial interaction, an electron-positron pair is created. The positron annihilates with a bound electron which produces two back to back 511 keV photons.

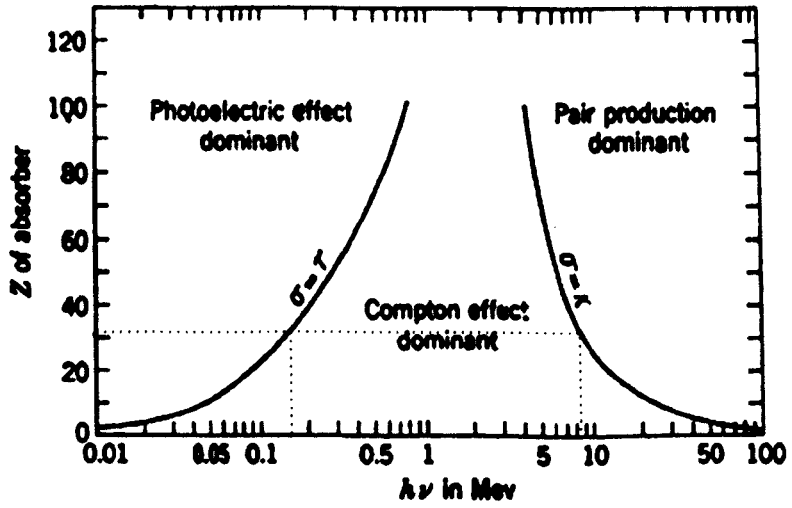

Figure 2.5: Illustration of the relative importance of photoelectric absorption, Compton scattering and pair production as a function of energy and Z. The dotted line is for Germanium (Z=32) [Kno00].

energy range of interest in this work is between 0.662 MeV and 6.130 MeV.

2.2 Gamma-ray detectors

Solid state detection systems offer many advantages over their gas based counterparts in the measurement of high energy electrons and gamma rays. The density of solid-state semiconductors and scintillators is some thousand times greater than for a gas resulting in a larger stopping power. This section will discuss the properties of both semiconductor and scintillator detector devices which feature in this thesis.

2.2.1 Semiconductor detectors

The band structure of permitted electron energies within a material is responsible for its electrical characteristics. The structure can be categorised into the conduction band, valence band and the energy gap between the two, called the band-gap. The size of the band-gap between the full valence band and the empty conduction band determines whether a solid state system is a semiconductor or an insulator. Typically the band-gap in a semiconductor is small enough so that valence electrons with a large enough excitation energy can be liberated and can cross to the conduction band. The band-gap of a typical semiconductor is $\sim$1 eV which is easier to overcome than an insulator where the band gap is greater than 5 eV. After the excitation of any valence electrons, a hole is left in the valence band. Collectively, the valence electron and the hole are known as an electron-hole pair. These are the charge carriers for a semiconductor device. The difference between an intrinsic semiconductor and an insulator is illustrated in Figure 2.6.

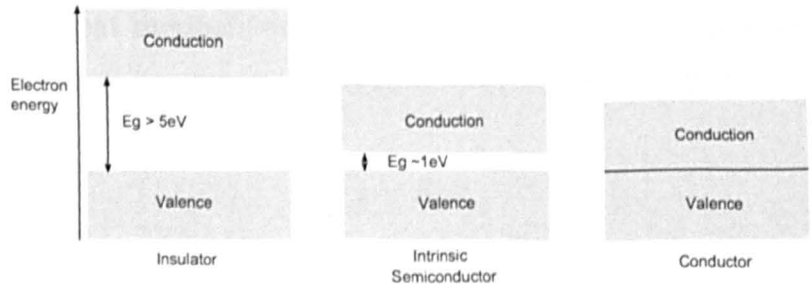

Figure 2.6: Schematic illustration of an insulator, intrinsic semiconductor and a conductor.

Semiconductors are used as detectors as only a small amount of energy is required to make an electron-hole pair, allowing a precise measurement of the energy deposited by any incident radiation. To create one electron-hole pair in germanium only 2.9eV is required (77K) and the resulting high statistics leads to good energy resolution. This creation energy is small when comparing with the energy required for scintillators (~100 eV). If small amounts of impurities are added to the semiconductor the properties can change quite drastically. This process is discussed in the next section.

2.2.2 Doping

Adding small amounts of impurities to a semiconductor material can alter its electronic properties. The band-gap structure of a semiconductor is modified by the addition of impurity atoms, introducing additional energy levels in the traditionally forbidden region between the valence and conduction band. These impurities (dopants) are either donors (atoms with an extra electron) or acceptors (atoms with one less electron). Adding impurities with acceptor (donor) atoms is known as p-type (n-type) doping and hence the detector device is said to be a p-type (n-type) semiconductor, having an abundance of extra holes (electrons). In a p-type (n-type) semiconductor, the majority charge carriers are holes (electrons) with the minority charge carriers being electrons (holes). Group III atoms (acceptor) will add a hole to the valence band whereas when a Group V atom (donor) is added, an extra electron is made available in the conduction band. Occupancy within the band gap is permitted through the addition of electrons or holes to the conduction or valence bands [Sze02]. As sufficient thermal energy exists to ensure that all impurities are ionised, the number of charge carriers can be described by equations 2.6 and 2.7,

$$p = N_A, \tag{2.6}$$

and

$$n = N_D, \tag{2.7}$$

where N_A and N_D are the acceptor and donor concentrations respectively.
Typical dopants in germanium are boron (p-type) and lithium (n-type). The subtle difference between an n-type and p-type semiconductor is illustrated in Figure 2.7.

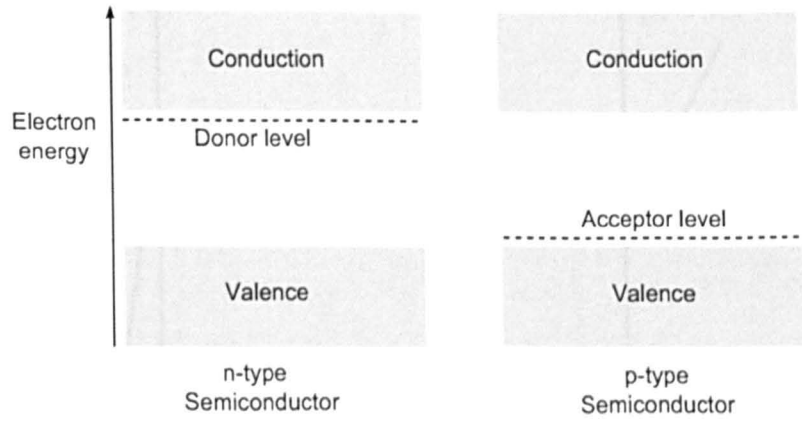

Figure 2.7: Schematic illustration of the difference between n-type and p-type semiconductors.

2.2.3 The P-N junction

The standard functionality of a semiconductor device relies on the p-n junction. Initially it is considered that both the p-type and n-type semiconductor materials are adjoined in thermal equilibrium. Once there is a good contact between the p and n-type material, electrons diffuse into the p-side and holes into the n-side. A potential of V_{bi} is obtained from this process [Lut01] and a region free from charge carriers is created at the junction. This is known as the depletion region. The depletion region is an essential basic component of any gamma-ray detector. The existing electric field across the depletion region causes any electrons to travel to the n-type material (holes to the p-side) which produces a small electric signal. The thickness of the junction is small and hence an external voltage is applied to the junction to increase the radiosensitive region. In this case the detector system runs in reverse bias mode and this voltage is large enough to deplete the entire volume of the detector making the sensitive region of the system as large as possible. The relationship between the

current flow and the applied bias voltage across the p-n junction is illustrated in Figure 2.8.

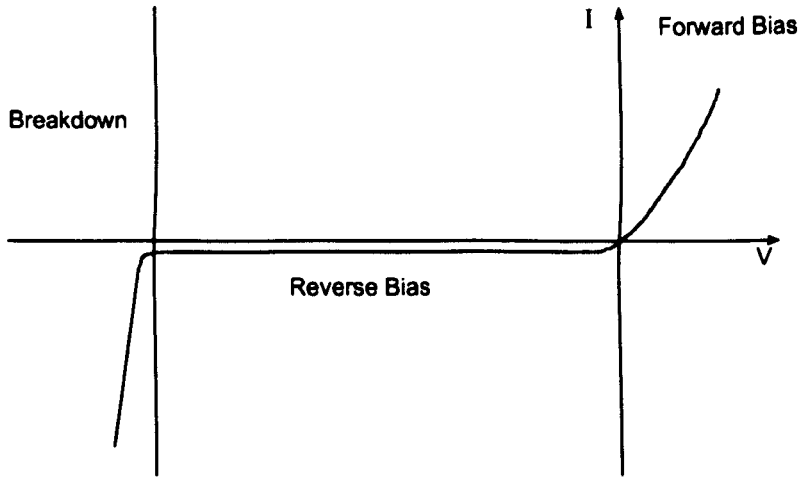

Figure 2.8: An illustration of the relationship between current flow and the applied bias voltage across the p-n junction.

A reverse bias applied accross the material makes it less likely for any excess charge to cross the depletion region. Typically the operating voltage of a radiation detector is larger than that of the depletion voltage in order to ensure complete saturation of the charge carrier drift velocity and optimise the charge collection performance. The width of the depletion region d is dependent on the impurity concentration N, the dieletric constant ϵ_r and the applied bias V. Given by Equation 2.8,

$$d = \sqrt{\frac{2\epsilon_r V}{eN}}. \tag{2.8}$$

The charge within the detector is spread through the p and n-type regions of dopant concentration. The outer regions are charge neutral and positive space-charge accumulates in the n-type region and negative space-charge accumulates within the p-type region due to the migration of holes and electrons respectively. This is illustrated in Figure 2.9.

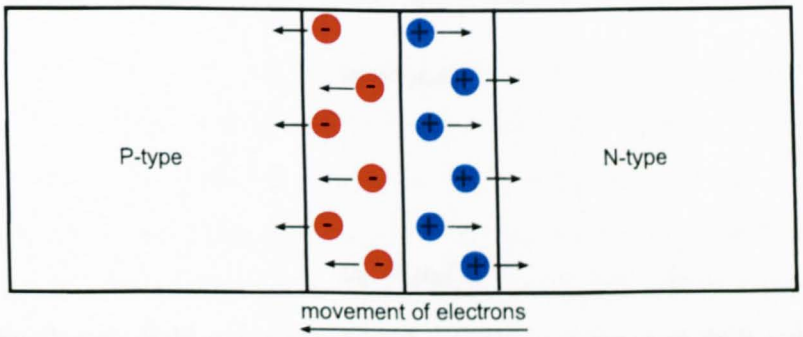

Figure 2.9: Schematic illustration of a P-N junction showing charge migration.

2.2.4 Charge carrier concentration

Following a gamma-ray interaction within the detector material a number of electrons and holes drift through the crystal from their specific bonding sites to their respective electrodes via the influence of the electric field. The number of electron-hole pairs created is dependant on the incoming energy of the incident gamma ray, E_γ and the ionisation energy of the absorber material E_{pair} given by Equation 2.9,

$$N = \frac{E\gamma}{E_{pair}}. \tag{2.9}$$

It is understood that if an electric field is applied to the detector material, then the charge carriers will undergo a net migration. The speed of this migration is called the drift velocity and the electron-hole pairs move parallel to the direction of the applied field [Kno00]. Holes move from one position to another as an electron leaves a normal valence site to fill another existing hole. The new vacancy represents the new position for the hole. The electrons are drawn in an opposite direction to the electric field while holes move in the same direction as the field. The hole represents the absence of any negatively charged electron. The net average drift velocity of electrons, μ_e and

holes, μ_h is variable for different materials according to their mobility μ.

$$v_e = \mu_e \varepsilon, \tag{2.10}$$

and

$$v_h = \mu_h \varepsilon, \tag{2.11}$$

where ε is the electric field component and v is the net average drift velocity.
As the electric field strength is increased the drift velocity increases proportionally until the drift velocity saturates, typically around 10^7cm/s. The drift velocity of electrons differs to the drift velocity of holes. In germanium, electron drift velocity saturation occurs at an electric field strength of the order of 10^3cm/s in comparison to a much higher electric field strength to saturate the drift velocity of holes. The properties of germanium are listed in Table 2.1.

Atomic Number, A	32
Atomic Weight, Z	72.6
Atoms	4.4×10^{22} cm^3
Density	5.32 g/cm^{-3}
Dielectric Constant, ϵ_r	16.2
Intrinsic Carrier Concentration (300 K)	2.0×10^{13} cm^{-3}
Energy Gap (300 K)	0.67 eV
Energy Gap (0 K)	0.75 eV
Ionisation Energy, (77 K) E_{pair}	2.96 eV
Electron Mobility (300 K)	3900 cm^{2}V/·s
Hole Mobility (300 K)	1900 cm^2/V·s

Table 2.1: Properties of germanium [Kno00].

2.2.5 The preamplifier

To be able to extract any signal generated by a gamma-ray interaction within a semiconductor, a charge sensitive preamplifier is required. The function of the preamplifier is to integrate the induced charge which results in a charge pulse with a magnitude that is proportional to the energy deposited within the detector by the gamma ray. This signal is processed using a Field Effect Transistor (FET). The output signal from the preamplifier is dependent on the charge collection characteristics of the detector where the decay time is determined by the time constant $R_f C_f$. These values are the feedback resistance and feedback capacitance which are typically $1G\Omega$ and 1pF respectively. To maximise the signal-to-noise from the detector system the preamplifier is located as close as possible to the detector. This minimises capacitive loading in connecting cables. A schematic illustration of a charge sensitive preamplifier is given by Figure 2.10.

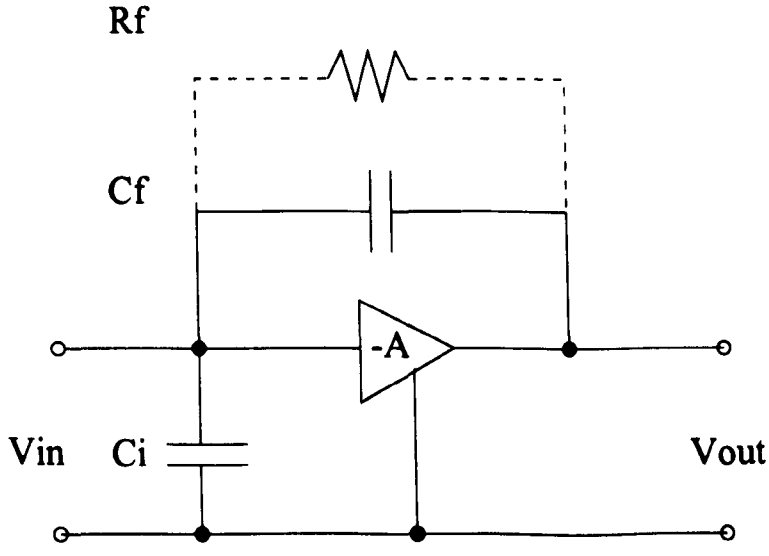

Figure 2.10: Schematic diagram which depicts the structure of a charge sensitive preamplifier. The induced charge is stored in the capacitor C_i and discharged proportional to $R_f C_f$.

2.2.6 Scintillator detectors

Scintillator detectors have been used thoroughly in radiation imaging systems since the invention of the Anger camera in the 1960's [Ang64]. Scintillation devices are still popular today due to their high efficiency, excellent light yield and short decay times. An ideal scintillation material for radiation detection applications requires the following properties [Kno00].

- A high scintillation efficiency from the ability to convert kinetic energy of charged particles into detectable light.
- A linear light yield which should be proportional to the deposited energy, over as wide a range as possible.
- The material should be of the best optical quality and be manufactured in large enough sizes appropriate for practical radiation detection applications.
- It should be transparent to the wavelength of its own emission wavelength for good light collection.
- Short decay time for fast electric signal generation.
- The refractive index should be similar to that of glass (1.5) which would allow efficient coupling of the scintillation light to a photomultiplier tube.

Detecting ionising radiation by scintillation light produced in particular materials is a very old method dating back to the early 1900's. The incident radiation raises electrons of the scintillator material from their ground state to higher lying excited states. The electrons that have moved to an excited state move back to a lower state and eventually de-excite back to the ground state. This de-excitation causes an emission of light. An ideal scintillator will have a high efficiency for converting the incident energy into light; the yield from the scintillator should be proportional to the incident photon energy. The light emitted from the scintillator can be detected in a light sensitive detector called a photomultiplier tube (PMT). The photocathode

of the PMT converts the light into photoelectrons and these are accelerated by an electric field towards the dynodes of the PMT where electron multiplication can take place. The electron is focused to a dynode, is absorbed and re-emits many more electrons. These new electrons are focused on the next dynode and the process is repeated throughout the array of dynodes. At the base of the photomultiplier tube is an anode which attracts the final large cluster of electrons and converts them into an electrical pulse which can be later analysed. A simple illustration of the process within a PMT is given by Figure 2.11.

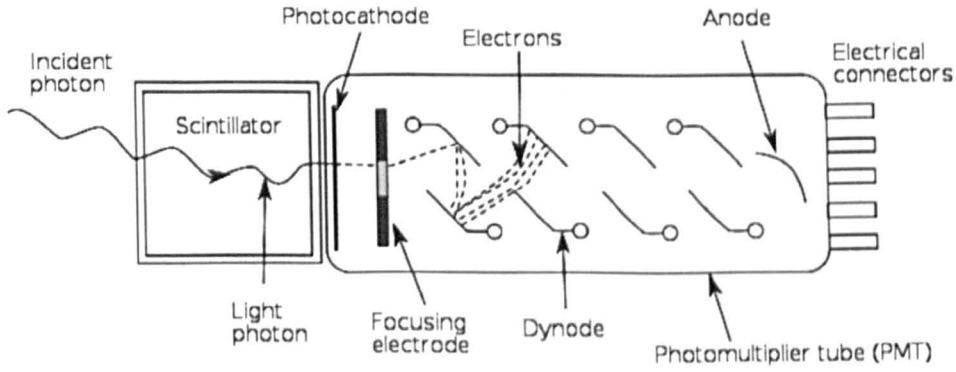

Figure 2.11: Schematic illustration depicting the process within a PMT, showing the steps from incident photon to the collection of electrons at the anode [Eng80].

Imaging systems, whether for nuclear medicine or security imaging have typically used thallium doped sodium iodide detectors, NaI(Tl). This thesis investigates the use of a thallium doped Caesium Iodide, CsI(Tl) scintillator detector for use in a radiation imaging system. Through a direct comparison of the properties of both NaI(Tl) and CsI(Tl) detectors it is clear to see why a CsI(Tl) detector is favourable in this thesis. The properties of both detectors are listed in Table 2.2.

Detector	NaI(Tl)	CsI(Tl)
Atomic Weight, Z	354.3	464.2
Density	$3.67\,g/cm^{-3}$	$4.51\,g/cm^{-3}$
Emission wavelength (nm)	415	550
Light yield (Photons/MeV)	38,000	65,000
Decay constant (μs)	0.23	0.68,3.34
Refractive index	1.85	1.80

Table 2.2: Properties of Sodium Iodide and Caesium Iodide [Kno00].

2.3 Detector performance parameters

The performance of a gamma-ray detector system can be quantified using the detector efficiency and the energy resolution. It is very important to understand these parameters as they are of significance when wanting to directly compare the performance of the detector systems discussed throughout this thesis.

2.3.1 Detector efficiency

The counting efficiency of a gamma-ray detector is defined by three primary metrics: Absolute efficiency, intrinsic efficiency and relative efficiency.

The absolute efficiency is given by the relationship between the count rate and the gamma disintegration rate of a particular nuclide (N_{emmitt}) and is dependent on the source and detector geometry. This is given by Equation 2.12,

$$\epsilon_{abs} = \frac{N_{det}}{N_{emitt}}, \tag{2.12}$$

Intrinsic efficiency is given as the number of photons detected relative to the number of incident photons on the detector (N_{inc}) and is dependant on the physical properties of the detector as well as the energy of the incident photons and the detector geometry. This is given by Equation 2.13,

$$\epsilon_{int} = \frac{N_{det}}{N_{inc}}, \tag{2.13}$$

Relative efficiency is quoted as the efficiency of any given detector relative to a 3x3 inch Sodium Iodide detector (Using a ^{60}Co point source 25cm from the front face of the detector). Relative efficiency is calculated using Equation 2.14,

$$\epsilon_{rel} = \frac{\epsilon_{abs}}{1.24 * 10^{-3}}. \tag{2.14}$$

2.3.2 Energy resolution

The precision with which a detector can identify the energy deposited is given by the energy resolution. The overall energy resolution is determined by three important factors. The energy resolution W_T is given by Equation 2.15.

$$W_T = \sqrt{W_D^2 + W_X^2 + W_E^2}, \tag{2.15}$$

where W_X represents incomplete charge collection in a semiconductor and light loss in a scintillator detector system, W_E is the contribution of electronics noise and W_D arises from any statistical fluctuation in the number of charge carriers created for every interaction event N_{pair} and is combined with the Fano factor F (typically 0.08 for germanium [Kno00]) given by Equation 2.16.

$$W_D^2 = \frac{2.35^2 F}{N_{pair}}. \tag{2.16}$$

The Fano factor accounts for the deviation from Poisson statistics of the observed statistical fluctuation in the number of charge carrier pairs produced. At lower energies the contributions from electronic noise and charge collection dominate while the broadening due to carrier statistics starts to dominate at higher energies. The contribution of all of the above factors is illustrated in Figure 2.12 as a function of energy.

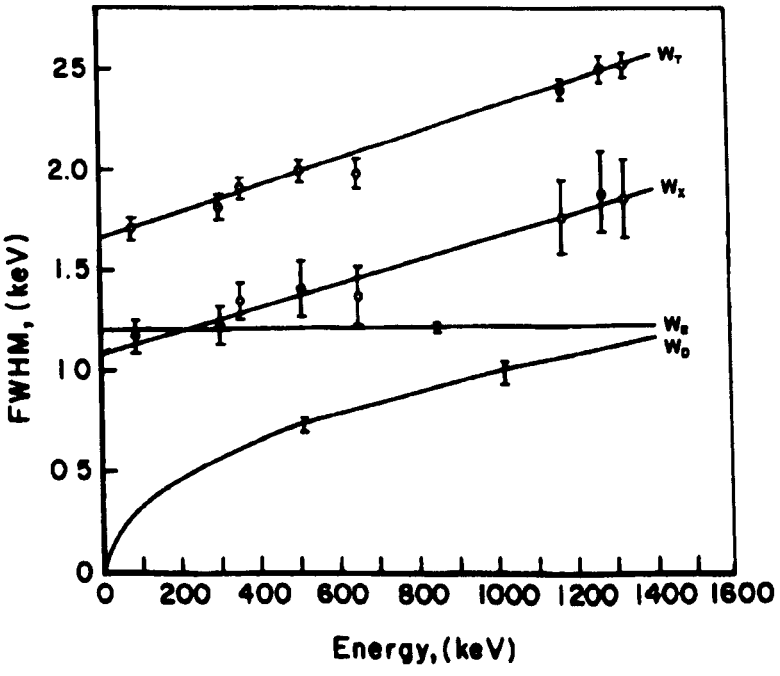

Figure 2.12: Graphical illustration of the variation in W_T, including the variations in W_X, W_E and W_D as a function of energy for a semiconductor detector. [Kno00].

Chapter 3

Compton Imaging

Since its inception in 1974 by Todd et al. [Tod74] Compton imaging has been utilised in a number of fields including Astrophysics [Sch93], medical physics [Har10] [Len08] and security imaging [Vet07]. A lot of work in security imaging [Vet00] [Vet07] [Mih09] [Du01] [Leh03] [Wah11] has looked at improving detector system image resolution by using detector systems with improved energy resolution but not looked at utilising systems with a higher absorption effiency. Chapter 5 of the current simulated work investigates the use of a CsI(Tl) scintillator as the absorber detector.

3.1 Compton camera operation

The basic concept of a Compton camera is that any single incident photon must undergo a minimum of two interactions in the detector system, via Compton scattering and photoelectric absorption. The simplest event sequence is a single Compton scatter followed by photoelectric absorption. Throughout this thesis, two energy and position sensitive detectors are used, with two different configurations. (one in Chapter 4 and the other in Chapter 5). The detectors are denoted the scatter detector, closest to the radioactive source and the absorber detector which is positioned directly behind the scatter detector as shown in Figure 3.1. A Compton camera requires a photon with energy E_0 to Compton scatter through the scatter detector depositing

a part of its energy E_1, where the remaining energy E_2 is fully absorbed within the absorber detector via photoelectric absorption, given by Equation 3.1.

$$E_0 = E_1 + E_2 \tag{3.1}$$

Utilising the conservation of energy and momentum of the deposited gamma ray, an image can be reconstructed. A cone is produced for each gamma-ray interaction by calculating three important features. The cone apex position that is defined by the interaction positions within the scatter detector, the cone apex angle, which is twice the angle of the Compton scattered gamma ray, and the cone axis which is given by the vector difference, determined by the interaction positions in both detectors. The radiation source is determined to be located in the area where there is a maximum overlap of cones. This is depicted in Figure 3.2 and each image illustrates a slice of the cone through the imaging axis (Z). Compton kinematics are used to reconstruct the cones. The cone angle, θ is calculated by introducing E_0 and E_1 into Equation 2.3 which we can rearrange to give Equation 3.2

$$cos\theta = 1 - \frac{E_1}{\alpha(E_0 - E_1)} \tag{3.2}$$

where $\alpha = \frac{m_0c^2}{E_0}$,$m_0c^2$ is the rest mass of an electron (0.511MeV) and E_0 is given by Equation 3.1

Figure 3.1 illustrates how a cone can be reconstructed from a single gamma ray.

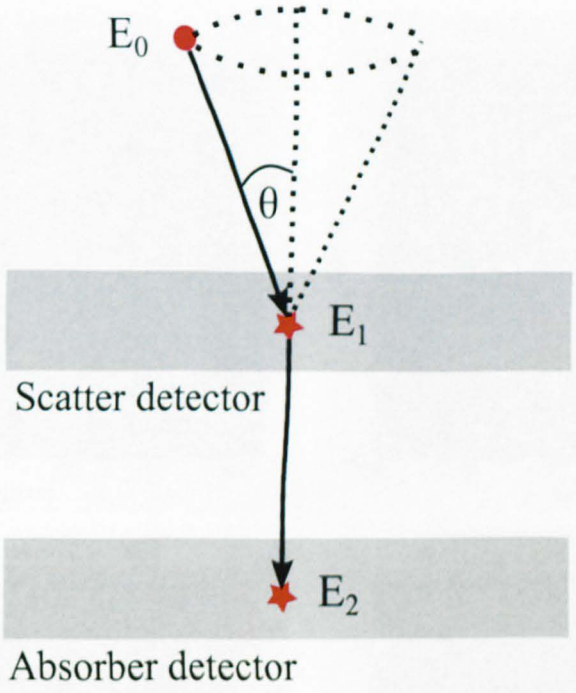

Figure 3.1: Schematic illustration of cone reconstruction for Compton imaging. The gamma ray energy is denoted by E_0, Compton scatters through the scatter detector at an angle θ depositing an energy E_1 and the remaining energy E_2 is absorbed in the absorber detector via photoelectric absorption.

Determining the position of any radiation source is governed by how many events can be reconstructed. The larger the number of events means the larger the number of reconstructed cones. The location of the radiation is depicted by the point where all the bases of the cones overlap. An example of the reconstruction of a different number of cones is illustrated in Figure 3.2.

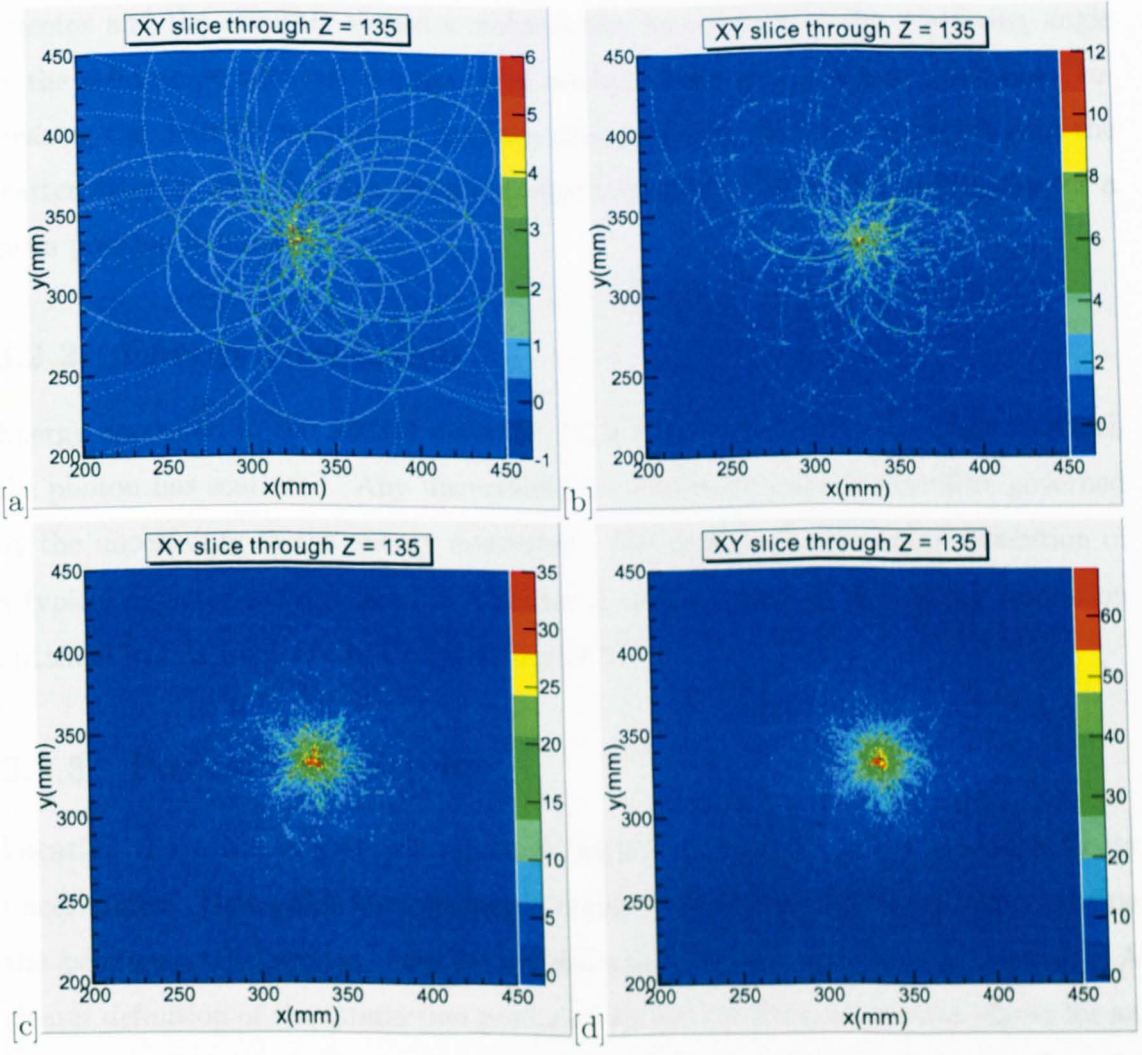

Figure 3.2: Compton images having reconstructed 50 cones (a), 100 cones (b), 500 cones (c) and 1000 cones (d). These are XY planes at a distance of 135mm from the bottom of the absorber detector. The bottom of the absorber detector is defined at Z = 0mm throughout this thesis.

3.2 Parameters affecting image resolution

3.2.1 System Geometry

The geometry of a Compton camera detector system contributes to an angular uncertainty when reconstructing an image. Increasing the separation between the scatter

detector and the absorber detector reduces the uncertainty in the scattering angle as the solid angle between the first and second interaction position decreases. Increasing the detector separation distance also decreases the solid angle between the scatter detector and absorber detector which decreases the imaging efficiency for a given position determination.

3.2.2 Energy Resolution

Energy deposited in the scatter detector, E_1 is used to calculate the angle in which the photon has scattered. Any uncertainty in scattering angle is therefore governed by the uncertainty in the energy deposited. The origins of the energy resolution of a typical detector are discussed in Chapter 2. More details of the energy resolution obtained in this work are in Chapters 4 and 5.

3.2.3 Position Sensitivity

Locating the exact interaction positions within a detector system comes with its uncertainties. Being able to reconstruct cones is dependent on being able to define the position and direction, relative to the axis in which the cone is oriented. A clearer definition of the interaction positions within the detector system allows for an improved resolution in the final image. Each of these parameters is discussed in the experimental results throughout Chapter 4.

3.2.4 Doppler broadening effects

In Compton imaging an assumption is made that any electron from which gamma rays scatter has zero momentum, which simplifies the relationship between the energy deposited in the scattering detector and the scattering angle. In reality, the electron moves and is bound to an atom in the scattering material which results in a non-zero electron momentum. The electron momentum is specific to the detector material properties and produces an angular uncertainty in the Compton scattering angle

[Ord97]. To ensure that this effect is incorporated, all simulations will be carried out using Geant4 version 4.9.2.

3.3 Image reconstruction

There are a number of reconstruction methods available, known as analytical or iterative algorithms. The most commonly used analytical method is the Filtered Back Projection (FBP). Analytical imaging methods are computationally efficienct but there is the issue of poorer image qualities as experimental characteristics of the detector properties used are not taken into account. Iterative methods estimate the source distribution over a system matrix and the detector properties are considered. Iterative techniques are known to give better image quality but due to the processing power required are typically computationally expensive to run. The reconstruction method used throughout this work utilises an analytical algorithm and is simple Back Projection (BP) where no filters or iterative techniques have been applied. For detailed information on the aforementioned imaging algorithm types the reader is referred to [Zen01]. A cone beam reconstruction algorithm has been developed in house by Dan Judson [Jud11] which can create Compton camera images by processing events where a gamma ray interacts in the scatter detector (Compton scattering) and deposits the rest of its energy in the absorber detector (photoelectric absorption). As discussed in section 3.1 a number of key features including the detector interaction positions and the apex angle are required to generate a coherent image.

3.4 The analytical imaging algorithm process

3.4.1 Previous algorithms

The previous analytical imaging algorithm developed by [Scr07] used a 2D grid of 10,000 points for every event. This grid is then converted into a 3D conical shape. The 3D cone is rotated around the Theta and Phi angles and projected into the X, Y and Z imaging space. Once all cones are projected into the 3D space a 'slice' is taken at a particular depth, Z, where projections in the X and Y profiles are produced, as an intensity profile. This algorithm was written using Matlab [MATLAB] and was computationally slow due to the complex mathematics needed to generate an image. The current analytical imaging algorithm developed by Dan Judson [Jud11] replaces the 3D cones to 2D projections of the cone using C++. This process simplifies the mathematics overall making it computationally quick. The 3D to 2D method is given by Figure 3.3.

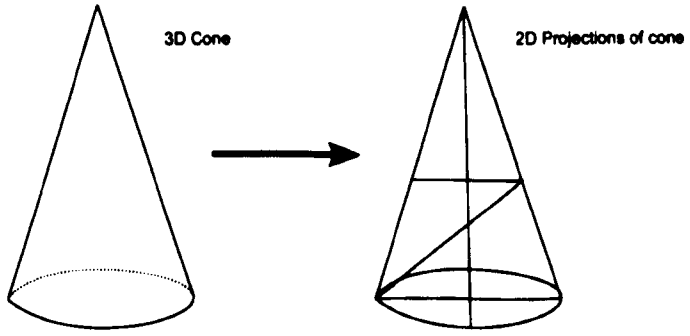

Figure 3.3: Schematic illustration showing the process of converting the 3D cone projections into 2D.

If a cone was projected perpendicular to the detector face then the intersection of the cone with the imaging plane generates a perfect circle, the size of which can be deduced by using Equation 3.3. This simple mathematical process is illustrated by Figure 3.4.

$$r = Ztan\theta \tag{3.3}$$

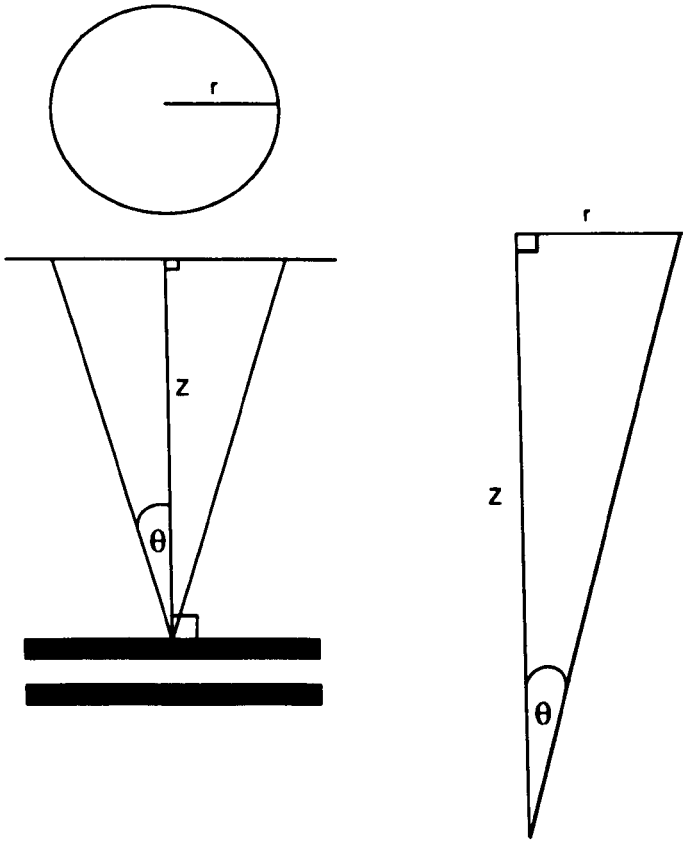

Figure 3.4: Schematic illustration of how the circle is generated using the intersection of a cone with the imaging plane.

The computationally slow process of generating the 3D transforms of the Matlab code are replaced in the C++ code using triginometry. The size and position of the 2D conics are calculated when a cone is sliced at a given angle and distance in Z. The conics are then projected onto a 2D imaging plane to produce the 2D images. The trigonometric calculations to generate the cone projections using the circle and projection lines are given by Equation 3.4, Equation 3.5, Equation 3.6 and the process is illustrated shematically in Figure 3.5 with all projection points indicated. θ_{scat} is the scattering angle of the incident gamma ray after interacting with the scatter

detector. θ_Z is the cone apex angle.

$$EAF = \theta_{scat} \tag{3.4}$$

$$AFE = \theta_Z \tag{3.5}$$

$$FY = AFTan\theta_{scat} \tag{3.6}$$

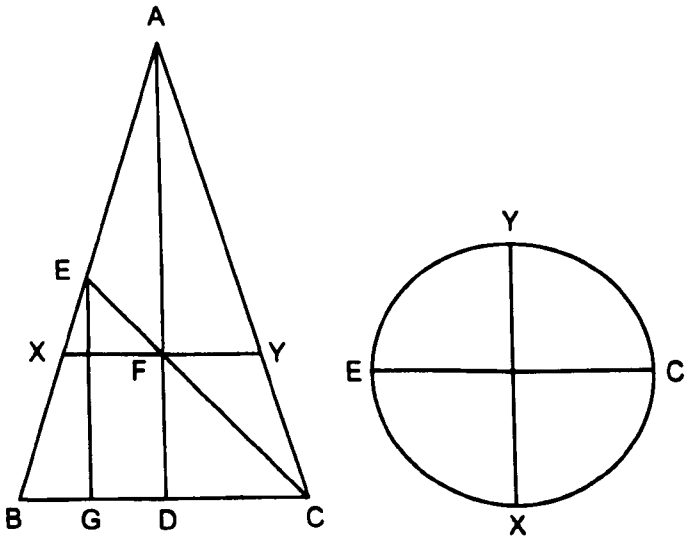

Figure 3.5: Schematic illustration of all the projection points used in the trigonometry calculations.

These features of the projections can be calculated by knowing the energy deposited, and the X, Y and Z positions within the detectors. The algorithm requires data input in the form $(X_{sc}, Y_{sc}, Z_{sc}, E_{sc})$ and $(X_{ab}, Y_{ab}, Z_{ab}, E_{ab})$. These are the energy deposition and X, Y and Z positions in the scatter detector and the absorber detector, respectively. Cones are reconstructed in a 2D matrix of 800mm(X) x 800mm(Y) at the points of maximum intensity in X and Y, where any range of image slices are created through Z space (Z slices) and are defined by the user. As previously mentioned the source location is identified as the area of with the greatest overlap of the Compton

conics, therefore the Z-slice that corresponds to the correct source location, the image FWHM will be minimal. Throughout this thesis, all source positions in Z were known and hence input as such into the algorithm.

Chapter 4

Experimental Compton imaging

A Compton imaging system has been experimentally tested. Using radiation sources available in the laboratory a range of data were taken and analysed to assess the performance of the detector system. This chapter discusses how the image resolution changes as a function of detector separation and also discusses the limitations in the ability to reconstruct images when a radioactive source is placed away from the centre of the scatter detector face.

4.1 The detectors

The detectors used in the experimental configuration were two identical planar double sided High Purity Germanium (HPGe) detectors. Germanium is widely used as a radiation detector due to its excellent energy resolution. Its properties are discussed in Chapter 2. A planar detector consists of a wafer of material which has electrical contacts on the outer surfaces. Both detectors have an active volume of 60 x 60 x 20mm, contained within a 50mm deep Aluminium case with 12 AC and 12 DC contacts in an orthogonal configuration giving a strip pitch of 5mm, providing position interaction information. (Each voxel has a size of 5 x 5 x 20mm). Each contact is coupled to its own charge sensitive preamplifier which provides an output to the pulse processing chain (discussed in section 4.2.2). The detectors are surrounded by

a 7mm guard ring that provides a uniform electric field within the active volume. The operational voltage of -1800V is applied to the AC side of the detector and the DC side is grounded. A schematic illustration of a germanium planar detector is given by Figure 4.1.

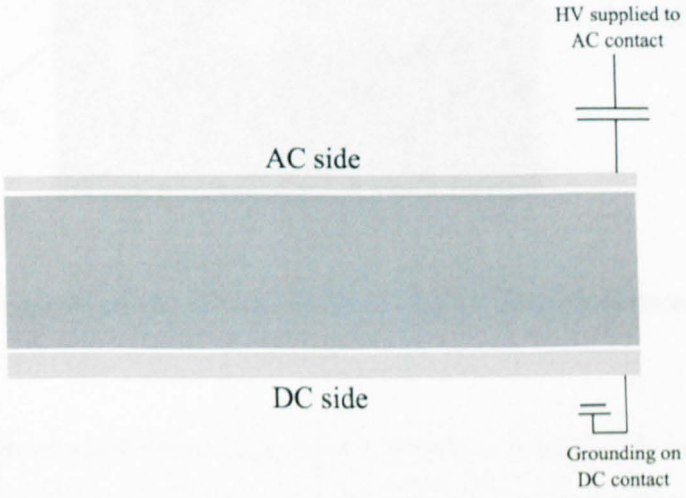

Figure 4.1: Schematic illustration of a planar detector where the AC contact has a bias voltage applied and the DC contact is grounded.

A front view of one of the detectors is illustrated in Figure 4.2 with all key features labelled.

4.2 The experiment

A range of experimental data were collected using a number of radioactive sources including a 0.267MBq ^{137}Cs (0.662MeV) gamma-ray point source and a 0.060MBq ^{60}Co (1.173MeV and 1.332MeV) gamma-ray point source.

4.2.1 Detector geometry

When developing a Compton imaging system it is important to have the optimum detector geometry. Figure 2.3 shows the Compton scattering cross section of gamma

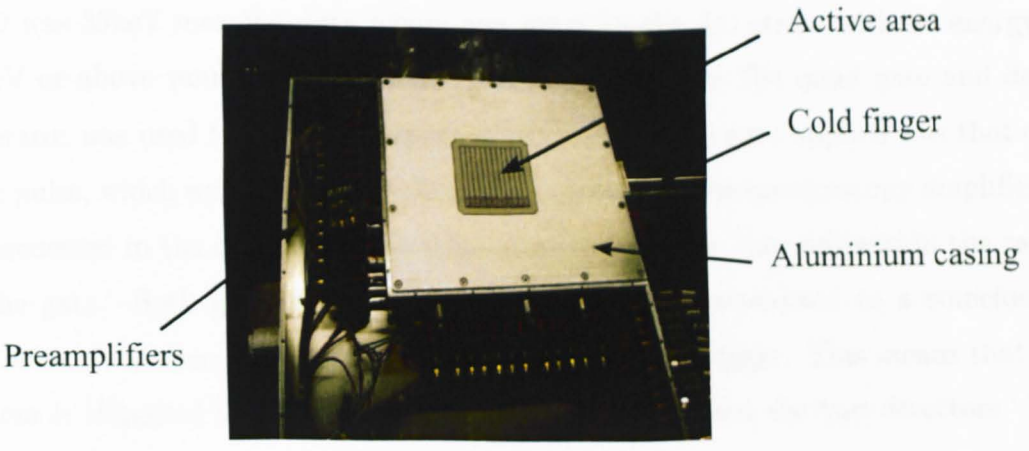

Figure 4.2: Photograph of one of the detectors used in these experiments inside the aluminium casing.

rays as a function of scattering angle over a range of energies. It is clear to see that above 500 keV the likelihood of forward scattering is more probable which is important for this work. Due to the larger probability of forward scattering the detectors are placed together with the absorber detector directly behind the scatter detector. A number of detector configurations were used, which included detector separations of 30mm, 50mm and 100mm.

4.2.2 Experimental setup

Experimental data were taken using analogue electronics. The preamplifier outputs of the AC channels of both the scatter and absorber detectors were split between the trigger and a CAEN N568 amplifier whilst the DC channels were input directly into independent CAEN N568 amplifiers. The outputs of these were input to the aquisition software MIDAS [Midas] through a CAEN V785 4K Analogue to Digital Converter (ADC). The trigger was set up using the 12 AC channels which were input to ORTEC 863 quad Timing Filter Amplifier (TFA) units where the AC preamplifier outputs were amplified. The TFA output signals are input to ORTEC 935 quad Constant Fraction Discriminator (CFD) units. The discriminator level set within the

CFD was 35keV meaning data where any event in the AC strips with an energy of 35keV or above would trigger the acquisition. A Phillips 794 quad gate and delay generator was used to join the outputs of the CFDs. The gate applied was that of a logic pulse, which was adjusted to allow any pulses from the spectroscopy amplifier to be processed in the data aquisition depending on whether they fell within the range of the gate. Both gate and delay output signals were connected to a coincidence unit which was then output to the ADC as an external trigger. This means that the system is triggered if there is any coincident event between the two detectors. The analogue electronics setup is illustrated by Figure 4.3.

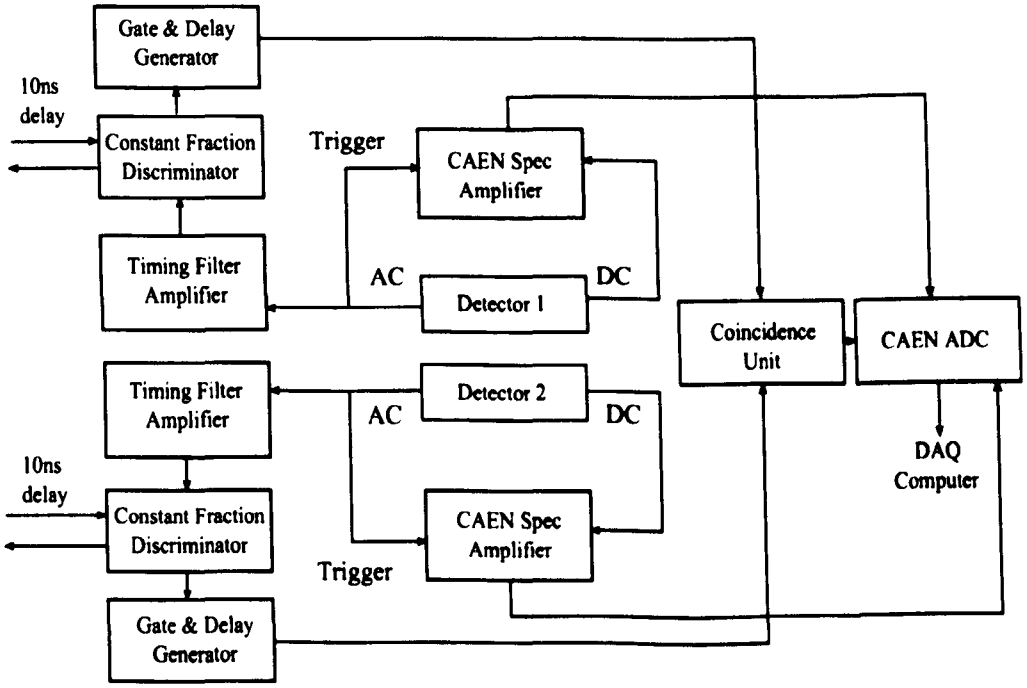

Figure 4.3: Schematic of the electronics setup used for the experiments.

4.2.3 Calibrating the detectors

All experimental data were collected using MIDAS [Midas]. Calibration data were taken for both detectors in singles mode (where only one detector is setup in the trigger at a time with the output of the gate and delay unit going to the ADC) using

a ^{152}Eu point source. A three point quadratic energy calibration was carried out and addback energy spectra were generated. (The addback energy spectrum is a collective of all energy spectra from each strip).

All events were grouped according to their fold where fold is defined as the number strips that fire and record a collective charge of a value greater than that of the energy threshold. (In this case 35keV). Figure 4.4 gives an illustrative example of Fold 1, Fold 2 and Fold 3 events.

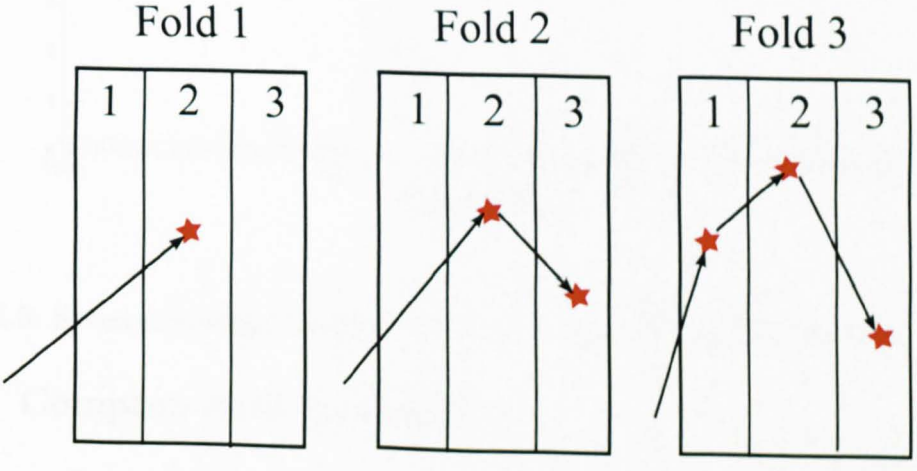

Figure 4.4: Illustrative examples of Fold 1, Fold 2 and Fold 3 with the interactions noted by the stars and the gamma-ray path given by the arrows.

4.2.4 Proportional cross-talk correction

Proportional cross-talk occurs due to the coupling between electronics channels resulting in an upward shift in energy. In terms of the addback energy spectrum, double peaking was observed and needed to be corrected. Cross-talk correction can be applied for fold 2 events using a correction factor which translates the incorrect position of the peak back to the correct position. This is done by adding a cross-talk coefficient which is calculated as the gradient of a graph of peak centroid shift as a function of energy [Coo08]. Figure 4.5 shows the uncorrected energy and the cross-talk corrected energy of the 1408 keV peak of ^{152}Eu in the scatter detector.

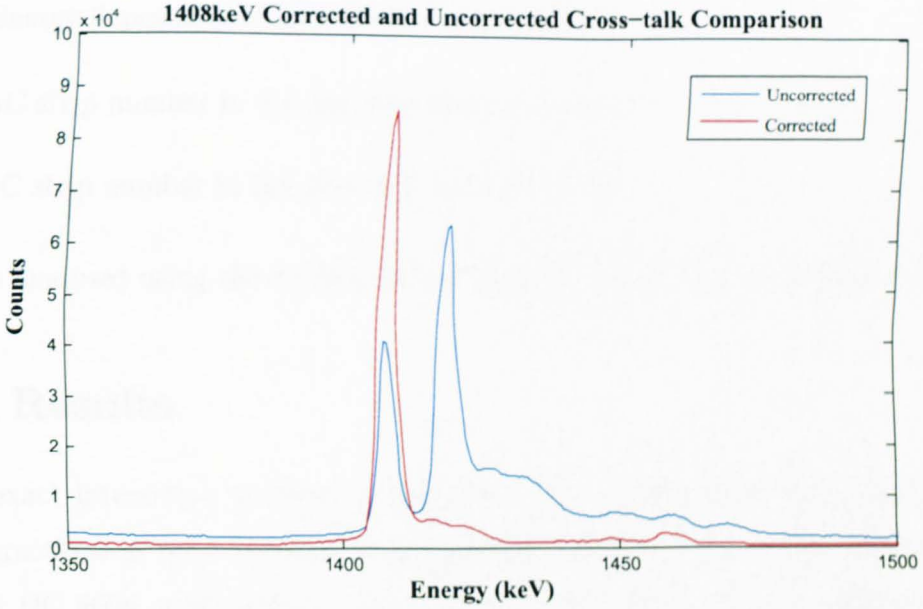

Figure 4.5: Spectra showing the uncorrected and corrected 1408keV photopeak of ^{152}Eu.

4.2.5 Compton data collection

Data were collected wherever there was a coincident event between the scatter and absorber detector. A coincident event is defined as there being an interaction in the scatter detector followed by an interaction in the absorber detector within a coincidence time window of 100ns. Coincident events include several fold possibilities. To be able to reconstruct the possible position of the source the ideal event type is fold 1 in both faces of the scatter detector and fold 1 in both faces of the absorber detector (1:1), where all of the energy of the incident gamma ray is absorbed. All of the data were sorted in MTSort [Midas] and all of the energy and strip information was output into a data stream to be analysed offline. The data stream contained the following information,

- Energy deposited in the scatter detector (E_s)
- AC strip number in scatter detector (AC_s)
- DC strip number in scatter detector (DC_s)

- Energy deposited in the absorber detector (E_a)
- AC strip number in the absorber detector (AC_a)
- DC strip number in the absorber detector (DC_a)

which is analysed using the reconstruction algorithm discussed in section 3.3.

4.3 Results

As no exact interaction position information can be calculated it is assumed that the interactions in both the scatter and absorber detector are in the centre of each AC and DC strip configuration. Each voxel has a pitch of 5 x 5 x 20mm and all interaction positions are assumed to be at 2.5 x 2.5 x 10mm within the strip. When reconstructing any images it is important that the correct Z slice is used to get the best image FWHM as this is the true representation of the source position in Z. All images in this chapter have been reconstructed using the correct Z slices. The ^{137}Cs and ^{60}Co point sources were positioned 45mm from the scatter detector AC face.

4.3.1 Experimental images

4.3.2 Point sources positioned at the centre of detector face

A ^{137}Cs and seperately a ^{60}Co point source were positioned at the centre of the scatter detector face (30mm,30mm) and 45mm away from the scatter detector in Z. A second set of experiments was undertaken with the two point sources separately positioned at the top left hand side of the scatter detector face (10mm,50mm) and 45mm away in Z. An assumption is made that for all source positions in all experiments, human error should be accounted for in the positioning of the source, as well as the error in the exact detector crystal placement within the cryostat. A further error is the definition of the interaction positions within the detectors. After the combination of these uncertainties, an assumption is made that all image FWHM values and reconstructed position values will have an error of ±5mm. The positions of the sources across the front of the scatter detector face are illustrated in Figure 4.6.

All energy and position information is input into the reconstruction algorithm and an ellipse at a distance of 45mm from the scatter detector face is created. Images have been created by the projection of 20,000 events from a ^{137}Cs point source and separately a ^{60}Co point source as a function of detector separation. The image FWHM(mm) in the X and Y projections is calculated for every image. Every reconstructed image is translated 300mm in X and 300mm in Y and the detector position is defined by the black box in every image. All X and Y projections are fitted using a Lorentzian peak fit and quadratic background fit using 300 channels, utilising a least squares minimisation fit. All image FWHM values are calculated from the fits as is the final reconstructed position in X and Y. This is consistent for all imaging results throughout this chapter and Chapter 5. The image FWHM for the X and Y projections which give us the images are given by Table 4.1. The image FWHM in both X and Y improves as a function of detectors separation as expected. It can be seen in Table 4.1 that the image FWHM in X and Y of 0.662 MeV improves from 26.9 ± 5.0 mm and 25.5 ± 5.0 mm at 30mm detector separation to 17.5 ± 5.0 mm

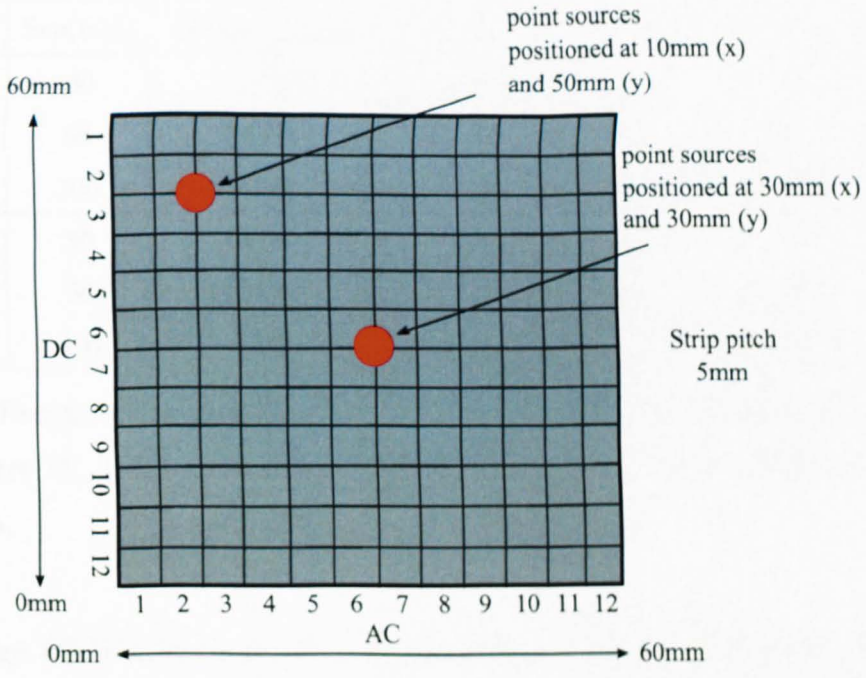

Figure 4.6: Figure showing the positions of the point sources across the front of the scatter detector face (off centre).

Energy	Sep(mm)	FWHMX(mm)	Error(mm)	FWHMY(mm)	Error(mm)
0.662MeV	30	26.9	5.0	25.5	5.0
	50	19.3	5.0	21.3	5.0
	100	17.5	5.0	16.7	5.0
1.332MeV	30	34.9	5.0	35.3	5.0
	50	28.6	5.0	28.5	5.0
	100	21.9	5.0	21.9	5.0

Table 4.1: Image FWHM(mm) for ^{137}Cs and ^{60}Co point sources positioned at the centre (X = Y = 30mm) of the scatter detector face at differing detector separations.

and 16.7 ± 5.0 mm at 100mm detector separation. The image FWHM in X and Y of 1.332 MeV improves from 34.8 ± 5.0 mm and 35.3 ± 5.0 mm to 21.9 ± 5.0 mm and 21.9 ± 5.0 mm at 100mm detector separation.

Energy	Sep(mm)	X(mm),Y(mm)	Rec X(mm)	Error(mm)	Rec Y(mm)	Error(mm)
0.662MeV	30	30,30	32.5	5.0	28.5	5.0
	50	30,30	34.3	5.0	31.3	5.0
	100	30,30	32.9	5.0	28.8	5.0
1.332MeV	30	30,30	32.6	5.0	28.8	5.0
	50	30,30	33.1	5.0	28.6	5.0
	100	30,30	31.0	5.0	28.6	5.0

Table 4.2: Reconstructed positions(mm) for ^{137}Cs and ^{60}Co point sources positioned at the centre (X = Y = 30mm) of the scatter detector face at differing detector separations.

These image FWHM improvements as a function of detector separation can be visualised in Figure 4.7. The reconstructed images of both the ^{137}Cs and ^{60}Co point sources positioned at the centre of the detector face are shown in Figure 4.8. The X and Y projections of ^{137}Cs and ^{60}Co are shown in Figures 4.9 and 4.10 respectively. The reconstructed positions in X and Y of each of the point sources is given by Table 4.2.

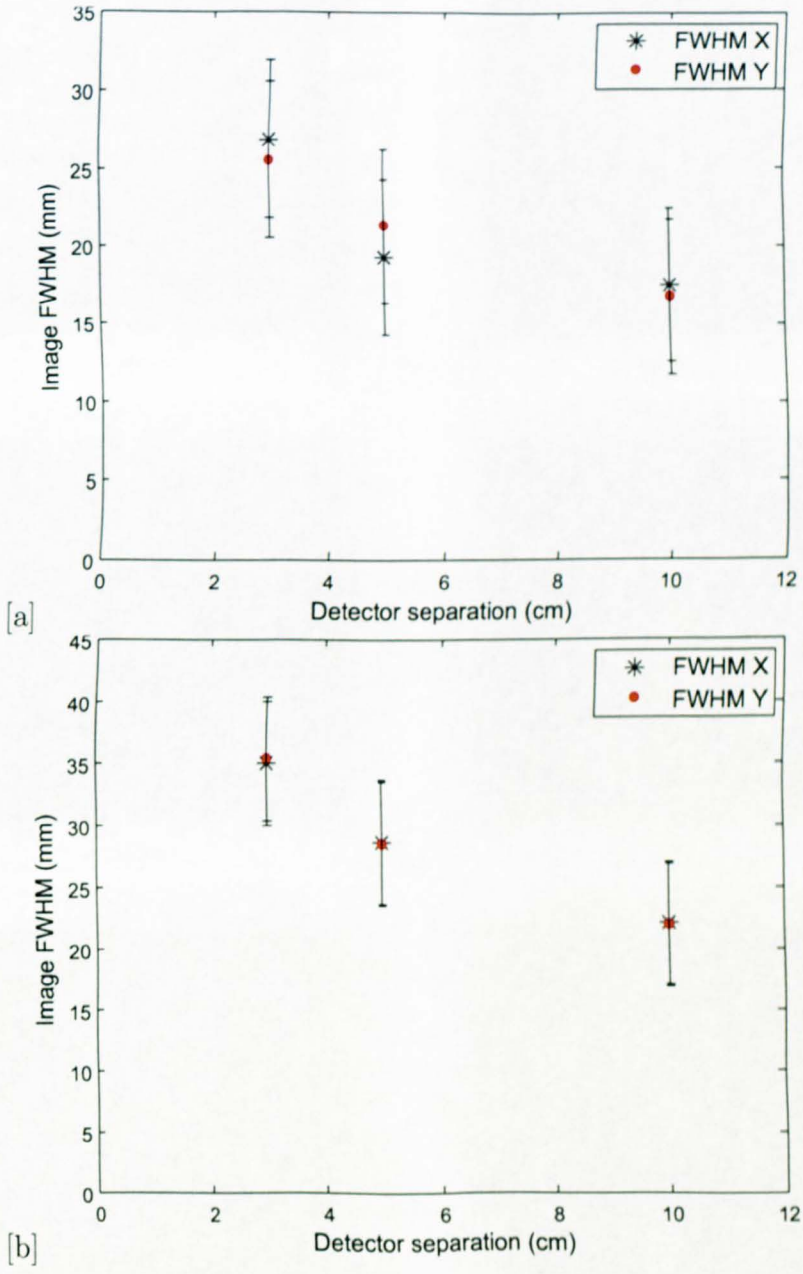

Figure 4.7: The Image FWHM (mm) as a function of detector separation for the X and Y projections of the ^{137}Cs [a] and ^{60}Co [b] with the source positioned at the centre (X = Y = 30mm) of the detector face.

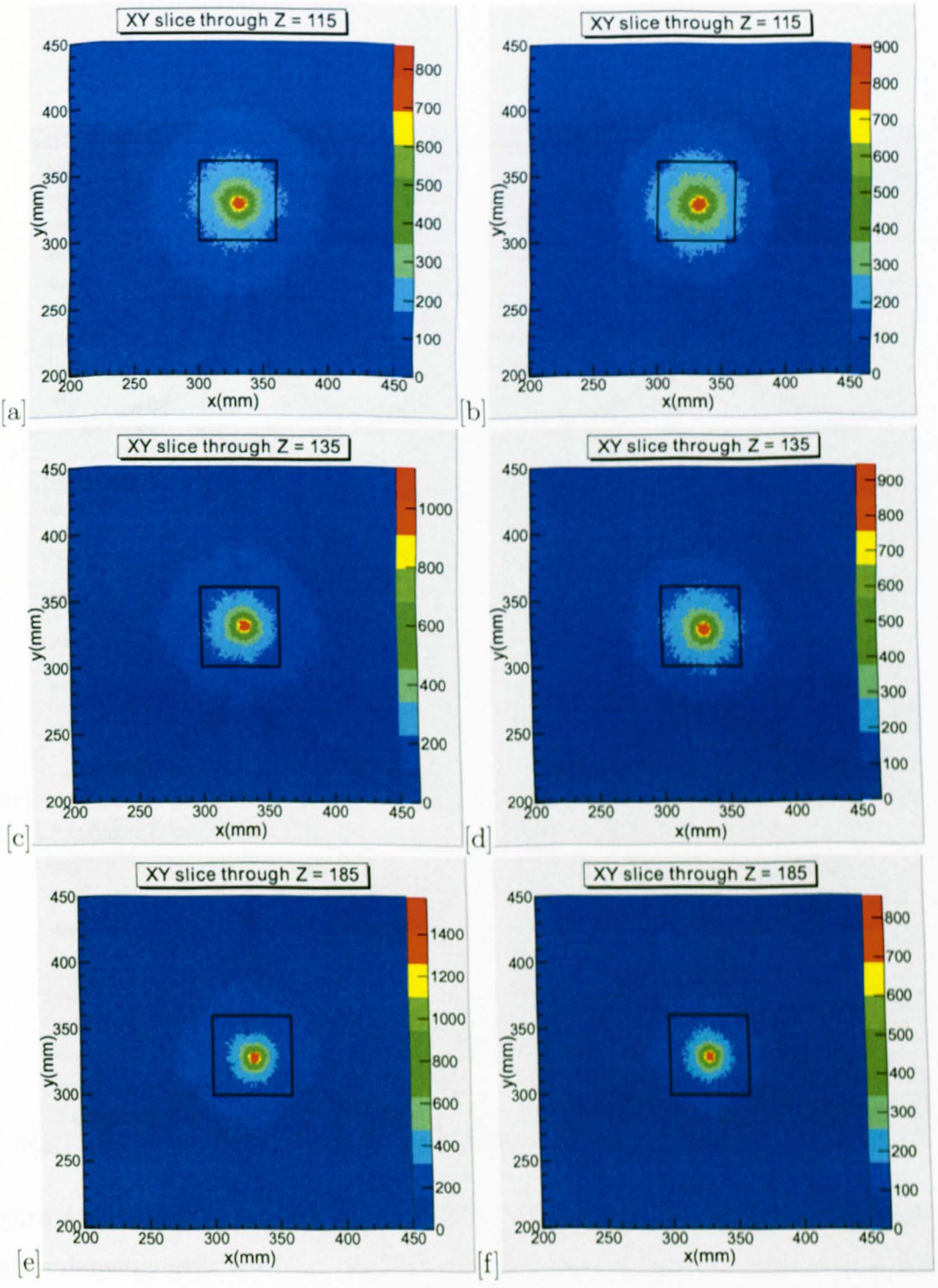

Figure 4.8: Experimental images of a ^{137}Cs point source positioned 45mm from the scatter detector with X = Y = 30mm with a detector separation of 30mm [a], 50mm [c] and 100mm [e] and images of a ^{60}Co point source positioned 45mm from the scatter detector with X = Y = 30mm with a detector separation of 30mm [b], 50mm [d] and 100mm [f].

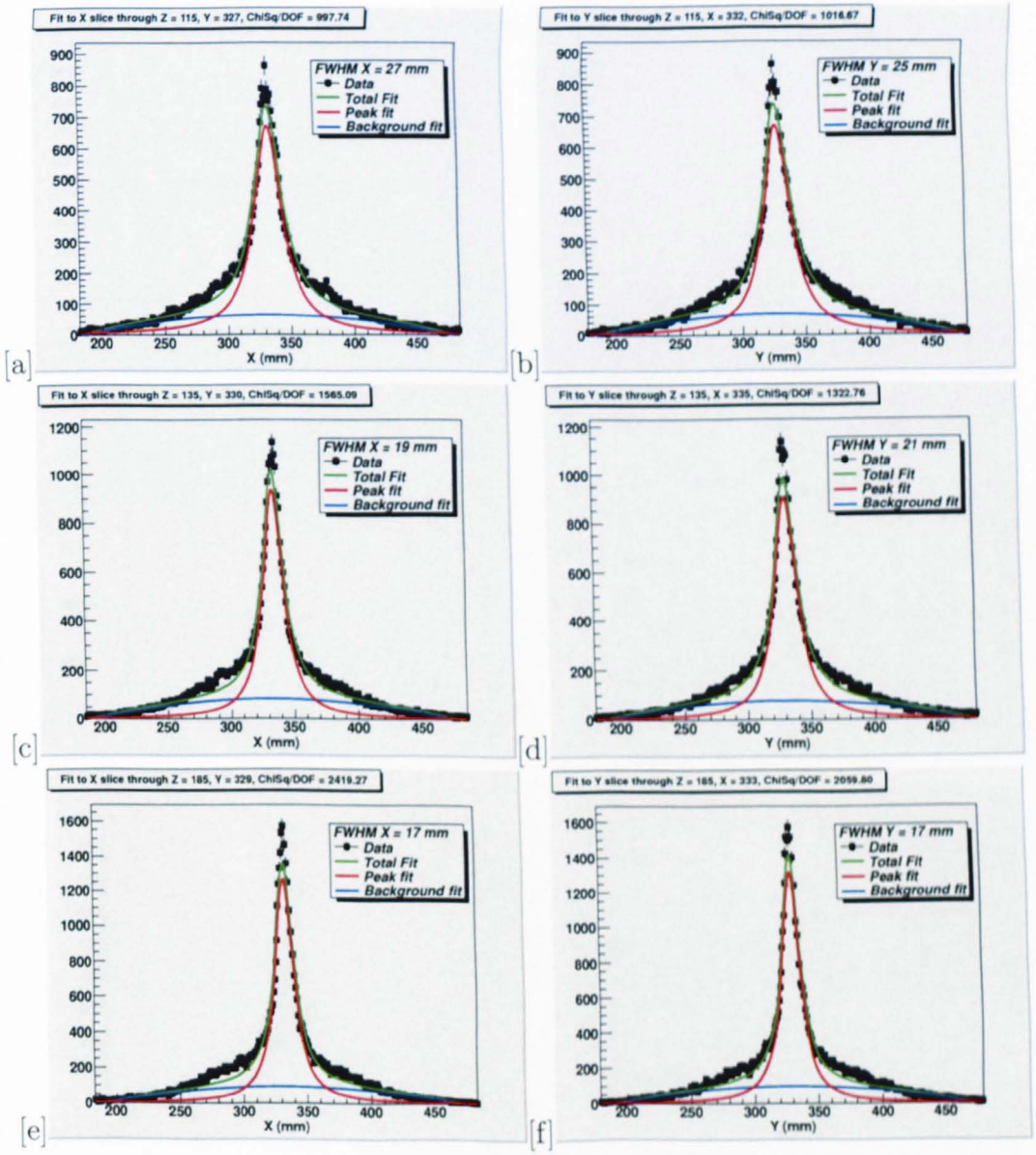

Figure 4.9: X and Y projections of a ^{137}Cs point source positioned 45mm from the scatter detector with X = Y = 30mm with a detector separation of 30mm [a][b], 50mm [c][d] and 100mm [e][f]. X projections are [a][c][e] and Y projections are [b][d][f].

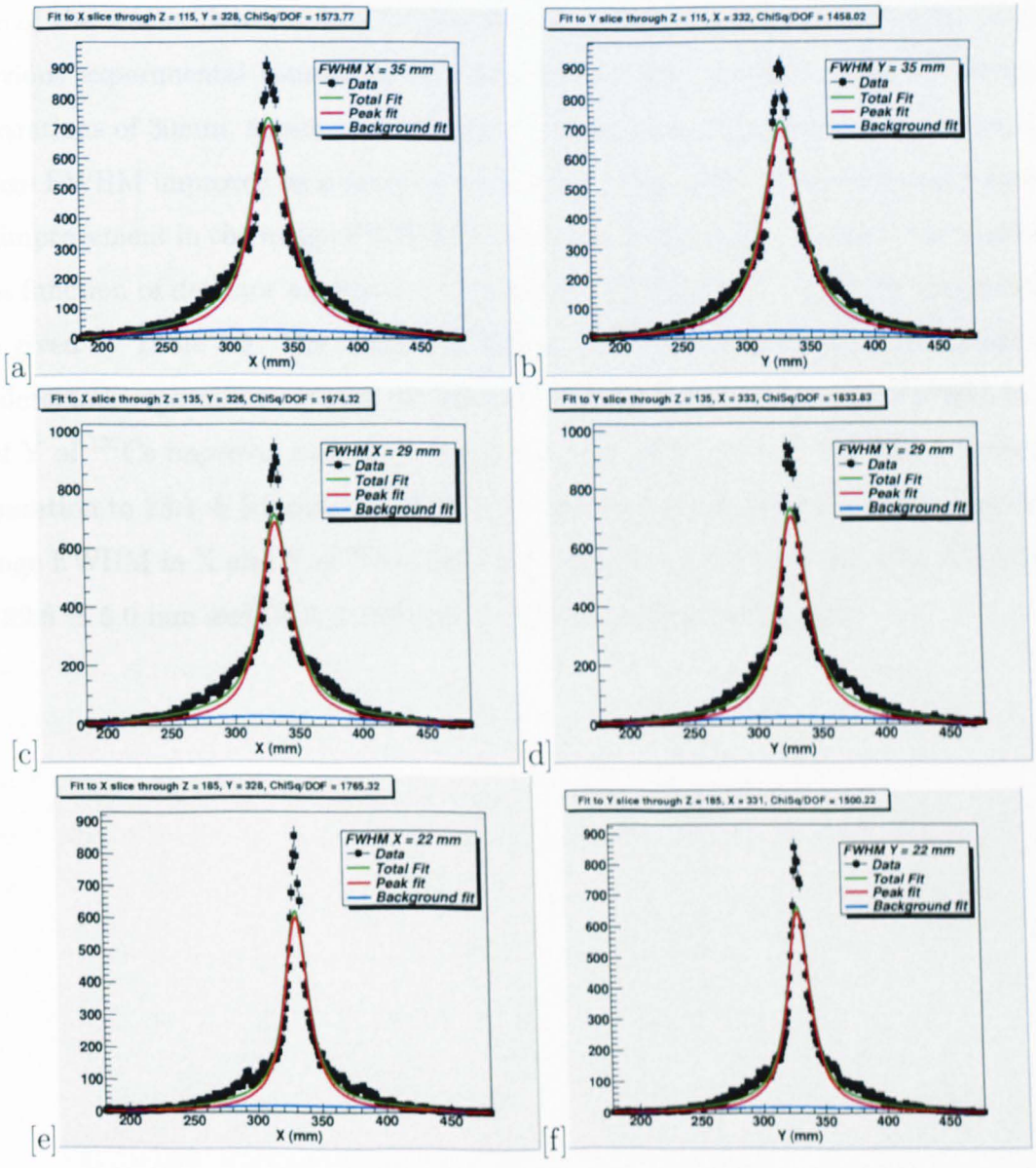

Figure 4.10: X and Y projections of a ^{60}Co point source positioned 45mm from the scatter detector with X = Y = 30mm with a detector separation of 30mm [a][b], 50mm [c][d] and 100mm [e][f]. X projections are [a][c][e] and Y projections are [b][d][f].

4.3.3 Point sources positioned at top left of detector face

A ^{137}Cs and seperately a ^{60}Co point source were positioned at the top left hand side of the scatter detector face (10mm,50mm) and 45mm away in Z. Similar to the previous experimental measurements, data were collected over a range of detector separations of 30mm, 50mm and 100mm. With the sources positioned at centre, the image FWHM improved as a function of detector separation. This experiment shows an improvement in the image FWHM for both the imaging of ^{137}Cs and ^{60}Co photons as a function of detector separation. The image FWHM for the X and Y projections are given by Table 4.3. The image FWHM in both X and Y improves as a function of detectors separation. It can be seen in Table 4.3 that the image FWHM in X and Y of ^{137}Cs improves from 32.1 $\pm$ 5.0 mm and 32.6 $\pm$ 5.0 mm at 30mm detector separation to 28.1 $\pm$ 5.0 mm and 23.9 $\pm$ 5.0 mm at 100mm detector separation. The image FWHM in X and Y of ^{60}Co improves from 41.6 $\pm$ 5.0 mm and 45.4 $\pm$ 5.0 mm to 29.6 $\pm$ 5.0 mm and 28.6 $\pm$ 5.0 mm at 100mm detector separation.

Energy	Sep(mm)	FWHMX(mm)	Error(mm)	FWHMY(mm)	Error(mm)
0.662MeV	30	32.1	5.0	32.6	5.0
	50	28.6	5.0	25.4	5.0
	100	28.1	5.0	23.9	5.0
1.332MeV	30	41.6	5.0	45.4	5.0
	50	34.1	5.0	34.9	5.0
	100	29.6	5.0	28.6	5.0

Table 4.3: Image FWHM(mm) for ^{137}Cs and ^{60}Co point sources positioned at the top left side (X = 10mm, Y = 50mm) of the scatter detector face at differing detector separations.

These image FWHM improvements as a function of detector separation can be visualised in Figure 4.11. The reconstructed images of both the ^{137}Cs and ^{60}Co point sources positioned at the top left side of the detector face are shown in Figure 4.12. The X and Y projections of ^{137}Cs and ^{60}Co are shown in Figures 4.13 and 4.14. The reconstructed positions in X and Y of each of the point sources is given by Table 4.4. The reconstructed position deviations can be seen in table 4.2 and 4.4. for X = Y = 30mm and X = 10mm and Y = 50mm respectively. They are illustrated by Figure 4.20.

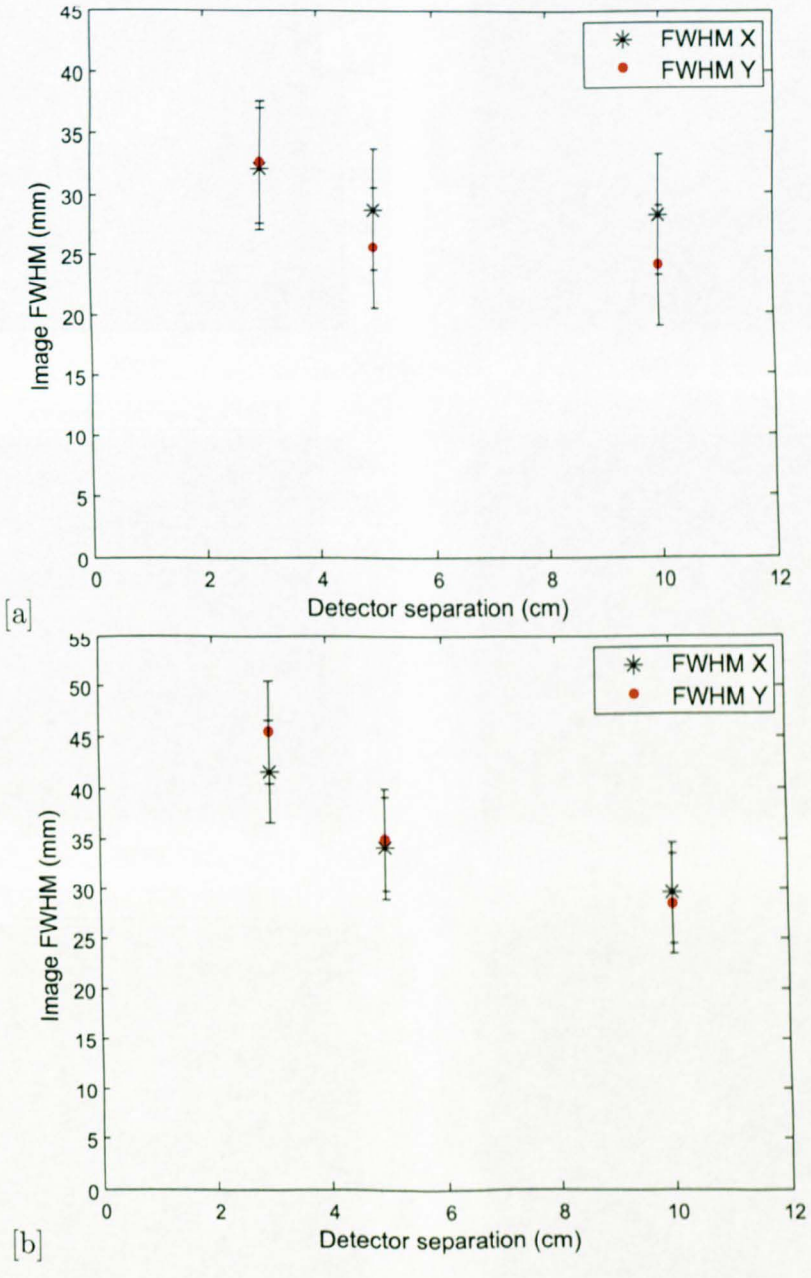

Figure 4.11: The Image FWHM(mm) as a function of detector separation for the X and Y projections of ^{137}Cs [a] and ^{60}Co [b] where the source is positioned at the top left side (X = 10mm, Y = 50mm) of the detector face.

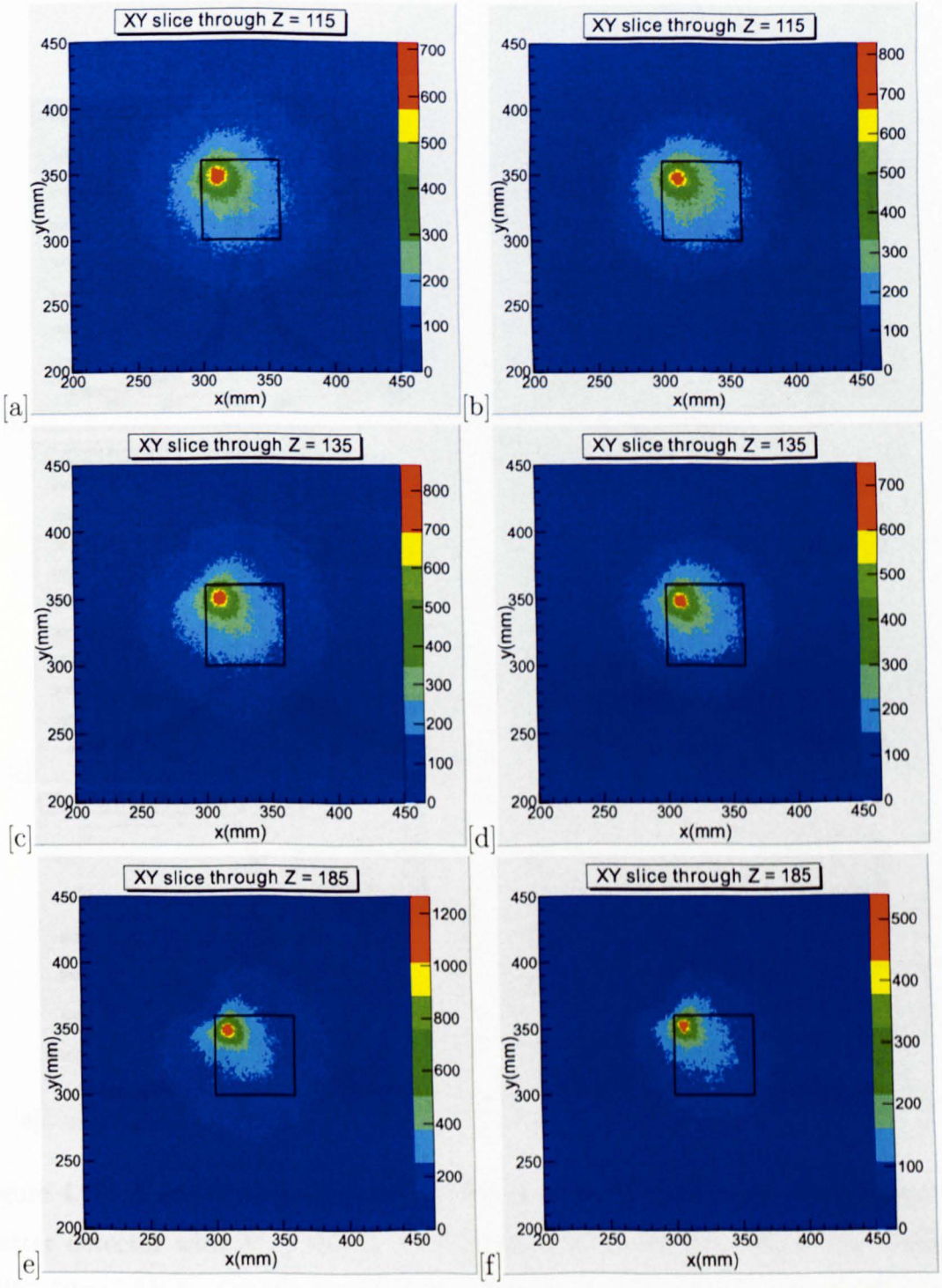

Figure 4.12: Experimental images of a ^{137}Cs point source positioned 45mm from the scatter detector with X = 10mm, Y = 50mm with a detector separation of 30mm [a], 50mm [c] and 100mm [e] and images of a ^{60}Co point source positioned 45mm from the scatter detector with X = 10mm, Y = 50mm with a detector separation of 30mm [b], 50mm [d] and 100mm [f].

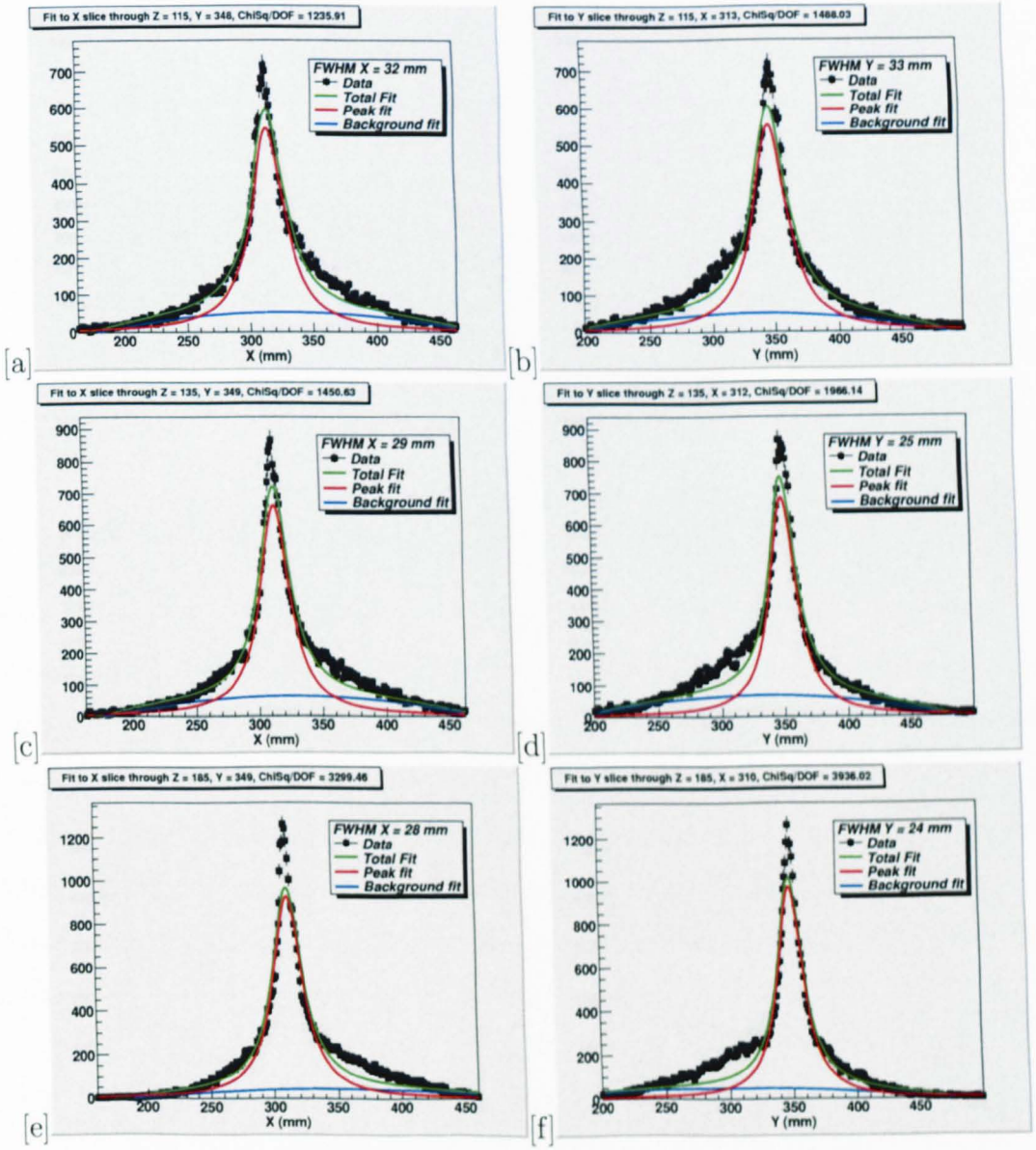

Figure 4.13: X and Y projections of a ^{137}Cs point source positioned 45mm from the scatter detector with X = 10mm, Y = 50mm with a detector separation of 30mm [a][b], 50mm [c][d] and 100mm [e][f]. X projections are [a][c][e] and Y projections are [b][d][f].

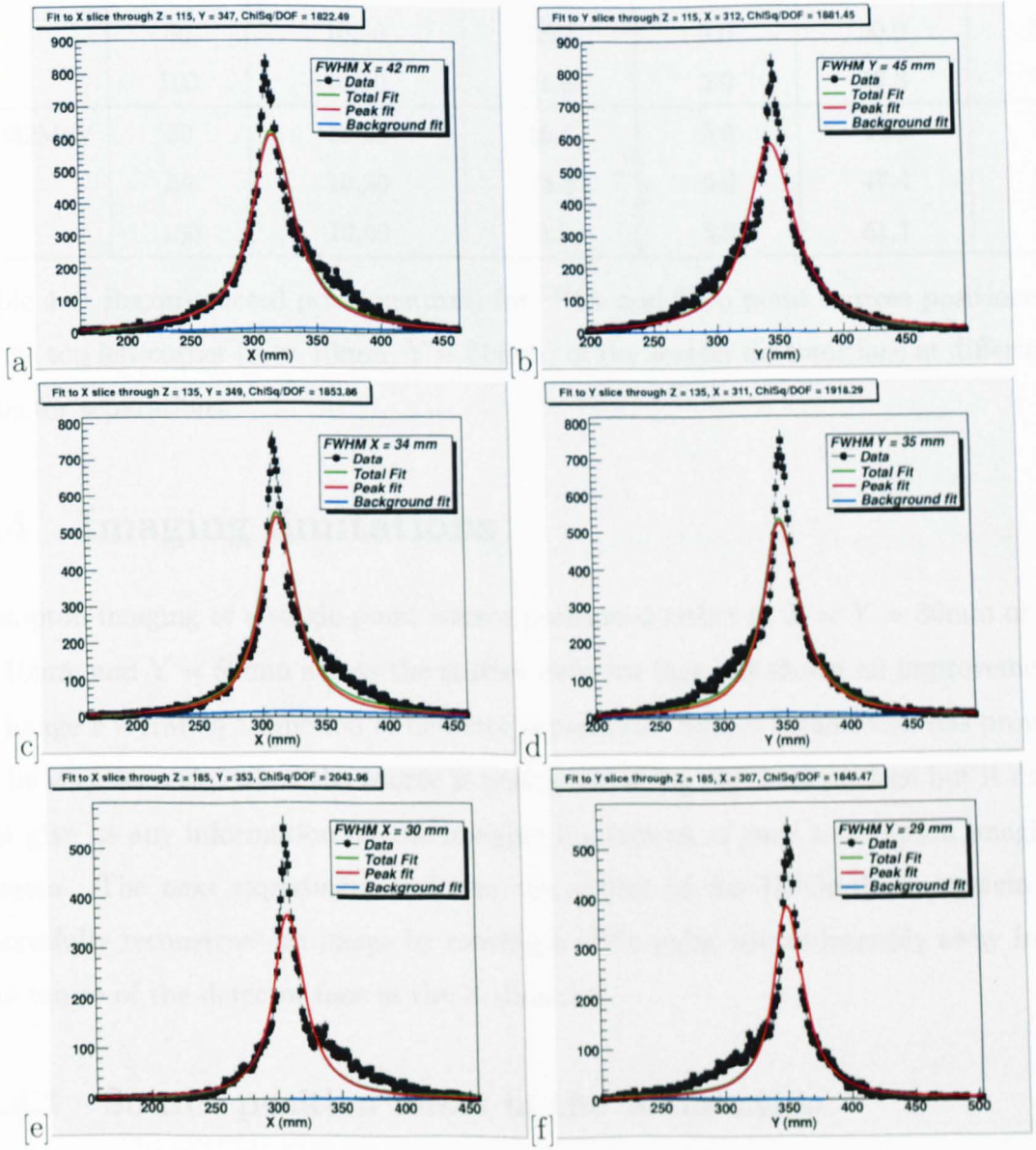

Figure 4.14: X and Y projections of a ^{60}Co point source positioned 45mm from the scatter detector with X = 10mm, Y = 50mm with a detector separation of 30mm [a][b], 50mm [c][d] and 100mm [e][f]. X projections are [a][c][e] and Y projections are [b][d][f].

Energy	Sep(mm)	X(mm),Y(mm)	Rec X(mm)	Error(mm)	Rec Y(mm)	Error(mm)
0.662MeV	30	10,50	15.3	5.0	46.5	5.0
	50	10,50	13.2	5.0	50.0	5.0
	100	10,50	11.8	5.0	49.3	5.0
1.332MeV	30	10,50	16.4	5.0	44.5	5.0
	50	10,50	13.8	5.0	47.4	5.0
	100	10,50	9.5	5.0	51.1	5.0

Table 4.4: Reconstructed positions(mm) for ^{137}Cs and ^{60}Co point sources positioned at the top left corner (X = 10mm, Y = 50mm) of the scatter detector face at differing detector separations.

4.4 Imaging limitations

Compton imaging of a single point source positioned either at X = Y = 30mm or X = 10mm and Y = 50mm across the scatter detector face has shown an improvement in image FWHM as a function of detector separation. Source localisation has proved to be very succesful when the source is positioned along the detector face but it does not give us any information on the imaging limitations of such a Compton imaging system. The next experiment looks at the ability of the HPGe-HPGe system to succesfully reconstruct an image by moving a ^{137}Cs point source laterally away from the centre of the detector face in the X direction.

4.4.1 Source position offset in the X direction

A ^{137}Cs point source was positioned at X = Y = 30mm and 45mm away in Z, at X = 80mm, Y = 30mm and finally X = 130mm, Y = 30mm to assess the image FWHM as we move the source further away from the centre of the detector face. When the source is offset from X = 30mm by 50mm and 100mm it is positioned 95mm away in Z. The source positions across the scatter detector face are illustrated by Figure 4.15.

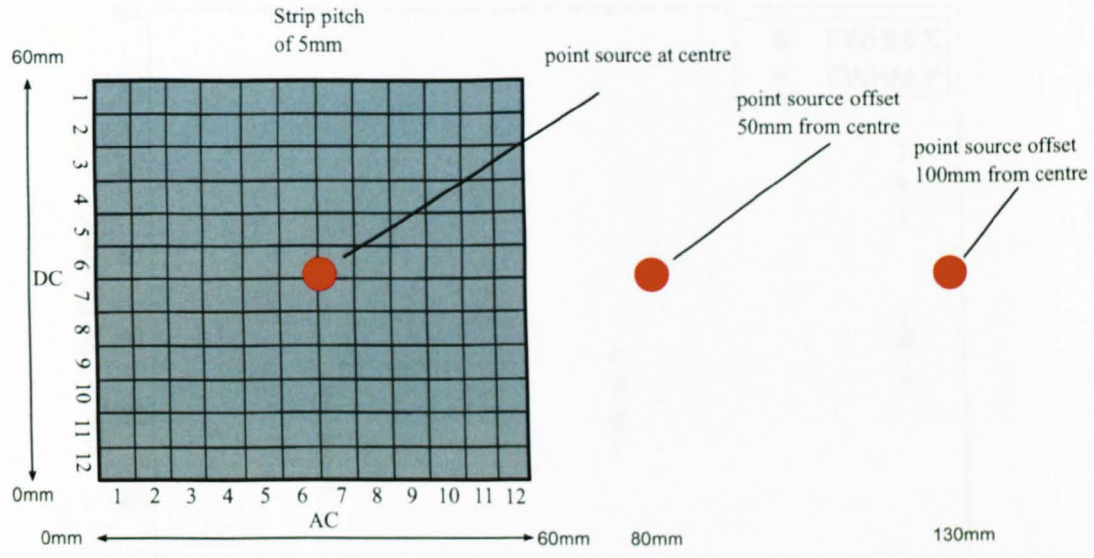

Figure 4.15: Schematic illustration of all three source positions. Positioned at Y = 30mm for all positions and X = 30mm, 80mm and 130mm.

PosX(mm)	PosY(mm)	FWHMX(mm)	Error(mm)	FWHMY(mm)	Error(mm)
30	30	26.9	5.0	25.5	5.0
80	30	29.0	5.0	32.6	5.0
130	30	38.4	5.0	57.8	5.0

Table 4.5: Image FWHM(mm) of a ^{137}Cs point source positioned at X = Y = 30mm and offset laterally in X to 80mm and 130mm, remaining at Y = 30mm.

The image FWHM for the X and Y projections which give us the images are given by Table 4.5. The image FWHM in both X and Y degrades as a function of increased lateral position. It can be seen in Table 4.5 that the image FWHM in X and Y of ^{137}Cs degrades from 26.9 ± 5.0 mm and 25.5 ± 5.0 mm at X = Y = 30mm to 29.0 ± 5.0 mm and 32.6 ± 5.0 mm at X = 80mm, Y = 30mm to 38.4 ± 5.0 mm and 57.8 ± 5.0 mm at X = 130mm, Y = 30mm. This can be viewed in Figure 4.16.

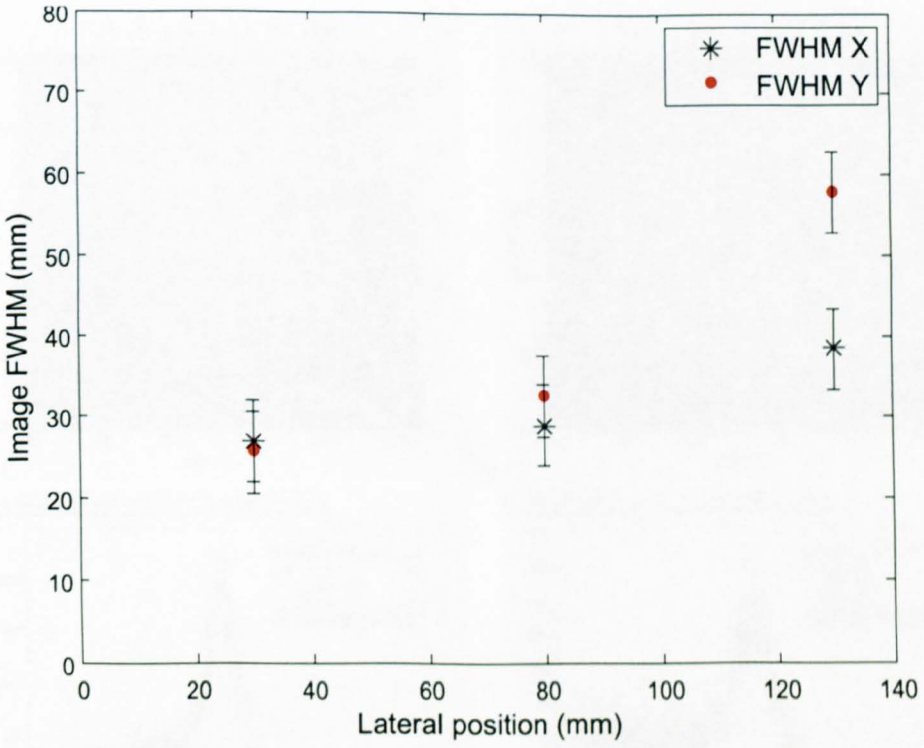

Figure 4.16: The Image FWHM(mm) as a function of the lateral position in X of a ^{137}Cs point source.

The reconstructed images of the ^{137}Cs point source at the new lateral positions and the X and Y projections are shown in Figure 4.17. The reconstructed positions in X and Y of each of the source positions is given by Table 4.6.

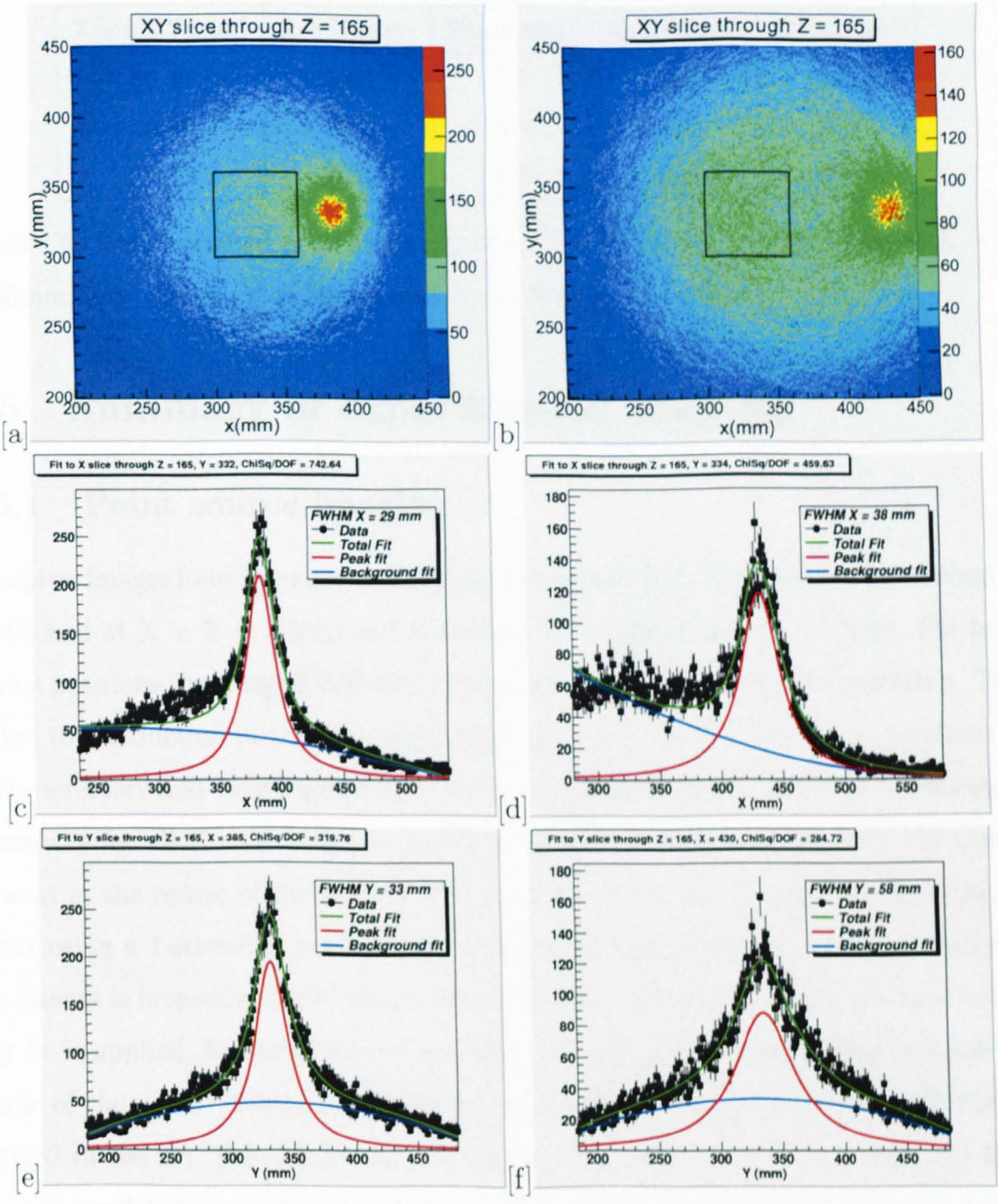

Figure 4.17: Experimental images of a ^{137}Cs point source positioned 95mm from the scatter detector in Z, with X = 80mm [a] and X = 130mm [b]. X projections at X = 80mm [c] and 130mm [d] respectively. Y projections at X = 80mm [e] and 130mm [f] respectively.

X(mm),Y(mm)	Rec X(mm)	Error(mm)	Rec Y(mm)	Error(mm)
30,30	32.5	5.0	28.5	5.0
80,30	83.4	5.0	32.2	5.0
130,30	132.2	5.0	35.0	5.0

Table 4.6: Reconstructed positions(mm) of a ^{137}Cs point source positioned at X = Y = 30mm, X = 80mm, Y = 30mm and X = 130mm, Y = 30mm.

4.5 Summary of experimental imaging

4.5.1 Point source imaging

Compton images have been successfully reconstructed for ^{137}Cs and ^{60}Co point sources positioned at X = Y = 30mm and separately X = 10mm and Y = 50mm. For both source positions the image FWHM improves as a function of detector separation. This is due to a reduction in the cone apex angle governed by the interaction positions in both detectors and here significantly in the absorber detector. There is a consistent symmetry for all X = Y = 30mm positions which is to be expected with the source located at the centre of the scatter detector face. All of the X and Y projections are fitted using a Lorentzian peak fit and quadratic background fit. This symmetry in the images is helped by their being a nice symmetrical shape to the projections before any fit is applied, however there is an issue with the fit not taking into account the whole of the peak. This can be adjusted by reducing the number of channels that is applied in the fit. This application of reducing the number of channels for the fit is done throughout the remaining chapters. This cannot be said for the images and X and Y projections for the source positioned at X = 10mm and Y = 50mm. There is an improved image FWHM as a function of detector separation but there is a clear asymmetry in the images, and X and Y projections, particularly at a larger detector separation. The images at X = Y = 30mm are shown in Figure 4.8 and X = 10mm, Y = 50mm are shown in Figure 4.12. The X and Y projections at X = Y = 30mm are shown in Figure 4.9 and 4.10. The X and Y projections for X = 10mm and Y

= 50mm are shown in Figures 4.13 and 4.14. The values of image FWHM and their errors for X = Y = 30mm are given in Table 4.1. The values of image FWHM and their errors for X = 10mm and Y = 50mm are given in Table 4.3.

It has not been possible to determine whether this asymmetry is due to any experimental effects and hence these experimental measurements will be replicated by simulation in chapter 5. To further understand this effect, simulations were carried out with a ^{137}Cs point source positioned across the scatter detector face in a variety of positions to asses whether this effect occurs consistently and is not just an experimental feature.

4.5.2 Imaging with a 50mm and 100mm offset in X

A ^{137}Cs point source was positioned at X = Y = 30mm, X = 80mm and finally X = 130mm. Compton images have successfully been reconstructed and it is seen that the image FWHM in X and Y degrades when the source is moved further away from the X = Y = 30mm position. This is due to a larger possibility of scattering angles through the scatter detector which leads to an increased cone apex angle in producing any reconstructable images. The increase in possible scattering angles as a function of lateral positioning of the source in X direction is shown schematically in Figure 4.18.

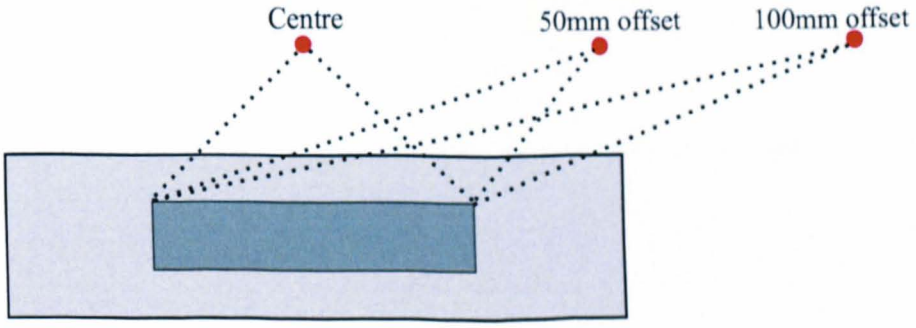

Figure 4.18: Schematic illustration of the increase in possible scattering angles as a function of lateral positioning of the source in the X direction.

Although there is a significant degradation in the image FWHM in the X and Y projections it can be seen that producing a reconstructed image is possible, and its positioning can be reconstructed very well. The reconstructed positions and their associated errors are given in Table 4.6. The images at X = 80mm and X = 130mm are shown in Figure 4.17 along with the respective X and Y projections.

4.6 Reconstruction position deviation

It can be seen in Table 4.2, Table 4.4 and Table 4.6 that for every source position, there is a reconstructed position deviation for the X and Y projections. The position deviation is illustrated by Figure 4.20 for the source positions at X = Y = 30mm and X = 10mm and Y = 50mm. Figure 4.19 illustrates the reconstructed position deviation when the source is moved laterally in X to 80mm and 130mm. These Figures show that there is a small deviation for every position. This deviation could be a feature of the ± 2.0 mm human error in positioning the source in exactly the correct position. All experimental reconstructed positions have an associated error of ± 5.0 mm.

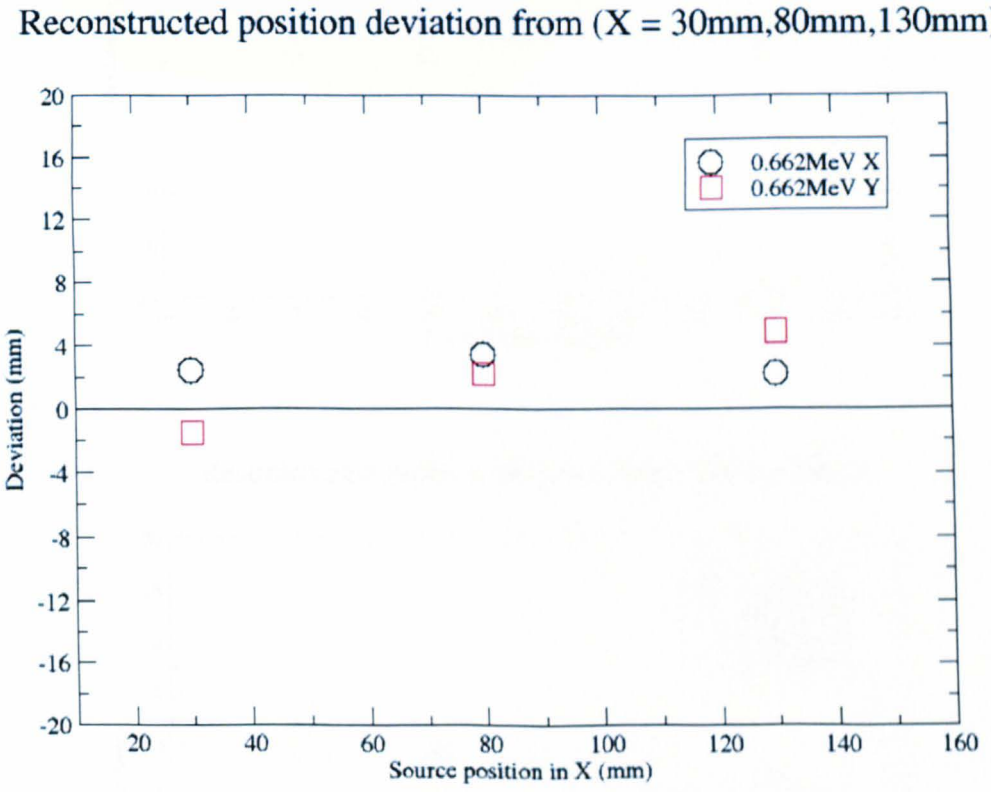

Figure 4.19: The reconstruction position deviations(mm) for X = 30mm, X = 80mm and X = 130mm

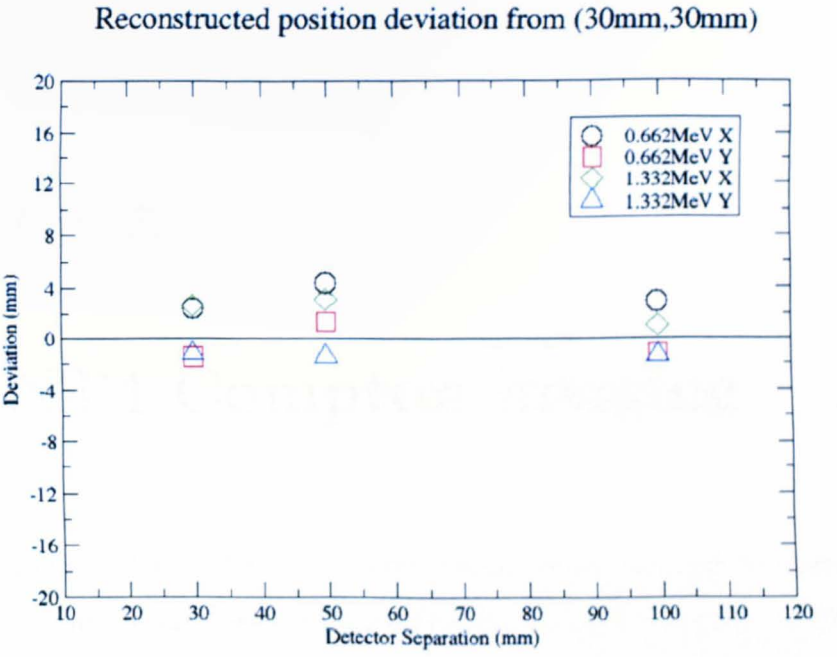

[a]

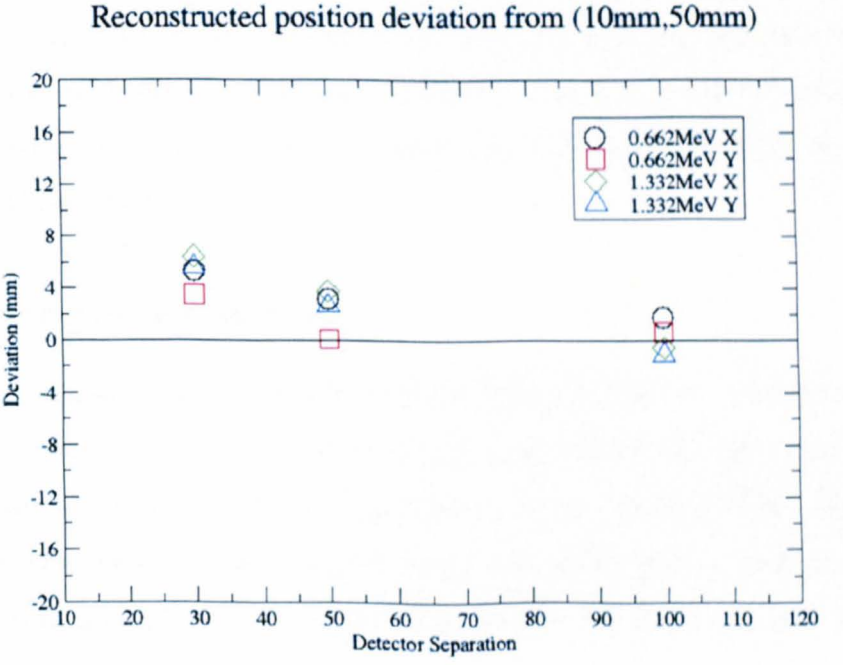

[b]

Figure 4.20: The reconstruction position deviations(mm) as a function of detector separation. [a] is the sources positioned at X = Y = 30mm, [b] is the sources positioned at X = 10mm and Y = 50mm.

Chapter 5

GEANT4 Compton imaging

A two germanium (GeGe) detector configuration and a germanium caesium iodide (GeCsI) configuration have been simulated using GEANT4 [Ago03]. GEANT4 is an object-oriented toolkit which implements the use of Monte-Carlo techniques and is programmed using C++. GEANT4 is used to simulate detailed particle interactions in matter. As GEANT4 can be customised to any application it is benificial to validate it for its purpose with experimental data. GEANT4 has been validated using a planar germanium detector across the energy range 0.08 MeV and 1.40 MeV by Harkness [Har10] and Oxley [Oxl10].

5.0.1 Detector geometry

This chapter compares the performance of two different detector configurations. The aim of this chapter is to quantify whether using a pixellated scintillator detector as the absorber material causes significant degradation to the image FWHM and how the 1:1 Compton efficiency compares to that of the two planar GeGe configuration. The planar detectors are simulated to match in geometry the detectors used in Chapter 4.

5.0.2 Simulation physics list

The low energy physics package [Cha04] is used in all the simulations. This package was chosen as it has been validated by the GEANT4 collaboration over the energy range 250 eV to 100 GeV and the energies of interest in this work are 0.662 MeV to 6.130 MeV. Gamma rays, electrons and positrons have been declared for the simulation and the low energy physics package reproduces the electromagnetic interactions at the energies of interest. These are Photoelectric absorption and Compton scattering which have been discussed in detail in Chapter 2.

5.0.3 Generating the radiation source

The General Particle Source (GPS) package has been used to generate the source of radiation. GPS allows the user to define whether the radiation is emitted isotropically, the source dimensions, the emission particle and the energy of the source. GEANT4 version 4.9.2 was used to produce 200 million primary gamma rays for each photopeak energy and is located at Z = 45mm from the scatter detector face in each simulation. A list of energies used in these simulations is given in Table 5.1. The 0.662 MeV and 1.332 MeV gamma-ray energies were discussed in Chapter 4 and the remaining energies represent those associated to the characteristic gamma rays of Oxygen, Carbon and Nitrogen.

5.0.4 Data collection and data processing

Data were collected at any time that radiation interacted in time coincidence with firstly the scatter detector and then the absorber detector. The gamma-ray energies used for the GEANT4 Compton efficiency simulations are 0.662 MeV, 1.332 MeV, 1.640 MeV, 2.310 MeV, 4.430 MeV, 5.110 MeV and 6.130 MeV. Each gamma ray and electron interaction within the detector materials was output into a data stream and contained the following information:

- Radiation type (gamma ray or electron)

- Energy deposited in the medium
- Delta energy (energy lost by the particle in any given interaction)
- Event number
- Track ID (particle origin)
- Pixel number (only for the absorber detector when it is CsI)
- AC and DC strip information (For the germanium detectors)
- x,y,z position information

5.1 A GeGe detector configuration

The detector geometry is replicated as close as possible in the simulation to that in the experiment. Experimentally the AC and DC electronic segmentation allows us to determine the interaction positions of the gamma rays within the detector. Electronic segmentation is not simulated but determining the AC and DC positions can be done offline by defining the electronic segmentation in the data analysis. The simulated geometry is as follows:

- The active volume of the detector
- The aluminium can
- The dead layer
- The guard ring that surrounds the detector material

but the simulation does not include the following:

- Any AC and DC contact segmentation (this is implemented offline)
- Preamplifiers and any other associated electronics
- The cold finger

5.1.1 GeGe Compton efficiency

GEANT4 simulated data were collected for a number of point source energies which include 0.662 MeV, 1.332 MeV, 2.310 MeV, 4.430 MeV, 5.110 MeV and 6.130 MeV. Each of these energies were simulated over a 30mm, 50mm and 100mm detector separation. The number of 1:1 events for every 200 million primary gamma rays over a different detector separation is given by Table 5.2.
It can be seen in Table 5.2 that as a function of detector separation the number of 1:1 Compton events reduces significantly. For the GeGe configuration, efficiency curves

Energy (MeV)	Sep(mm)	Events	±	Sep(mm)	Events	±	Sep(mm)	Events	±
0.662	30	14956	122	50	9473	97	100	3751	61
1.332	30	5582	75	50	3305	57	100	1234	35
1.640	30	4170	65	50	2427	49	100	841	29
2.310	30	2225	47	50	1291	36	100	474	22
4.430	30	787	28	50	494	22	100	128	11
5.110	30	490	22	50	156	12	100	77	9
6.130	30	123	11	50	61	8	100	25	5

Table 5.1: The number of 1:1 Compton events as a function of detector separation for GeGe. Energy range of 0.662 MeV - 6.130 MeV.

have been generated and are illustrated by Figure 5.1 with a closer look at 4.430 MeV to 6.130 MeV illustrated by Figure 5.2.

Chapter 4 concludes that the image FWHM improves with increased detector separation but at a cost to the efficincy of the imaging system. It is clear from Figure 5.1 that the efficiency of the GeGe system decreases as a function of energy and detector separation, where the efficiency is significantly lower at higher energies. While it is important to reconstruct the best possible image with the smallest image FWHM, it is key to have a system that is as efficient as possible.

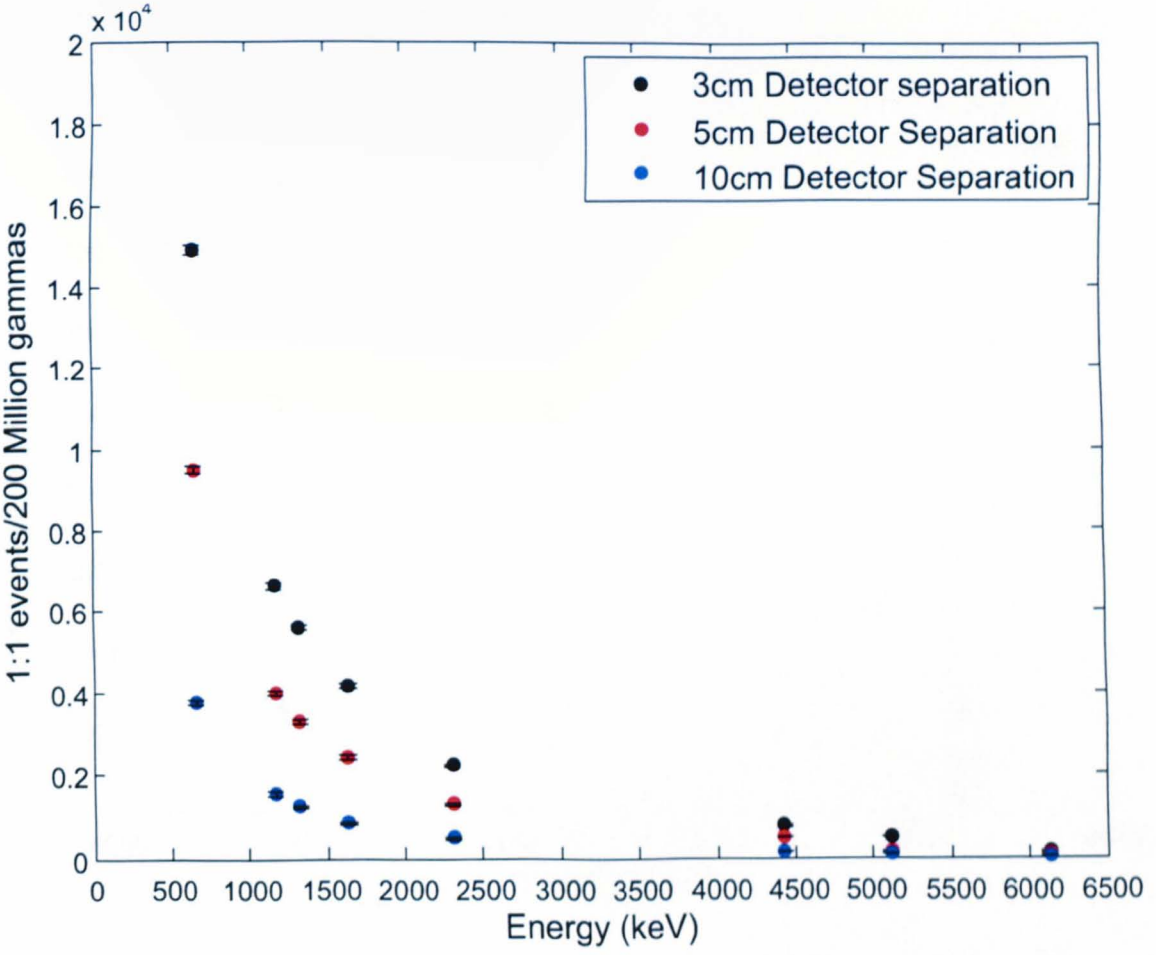

Figure 5.1: Plot showing the overall 1:1 Compton efficiency of the GeGe system in Compton imaging mode as a function of energy with detector separations of 30mm, 50mm and 100mm

5.2 A GeCsI detector configuration

The CsI detector geometry is replicated as close as possible to one that would be used experimentally. The GeCsI detector configuration has a Ge detector as the scatterer, which is the same as the detectors in the GeGe configuration. In the GeCsI configuration the CsI is the absorber. It has 64 pixels (8 x 8), with an active volume of 5.6 x 5.6 x 50 mm for each. The properties of CsI are given in Table 2.2 and given this information and that the attenuation cross section of CsI is higher than that of Ge, one would expect that the photoelectric absorbtion cross section of CsI would

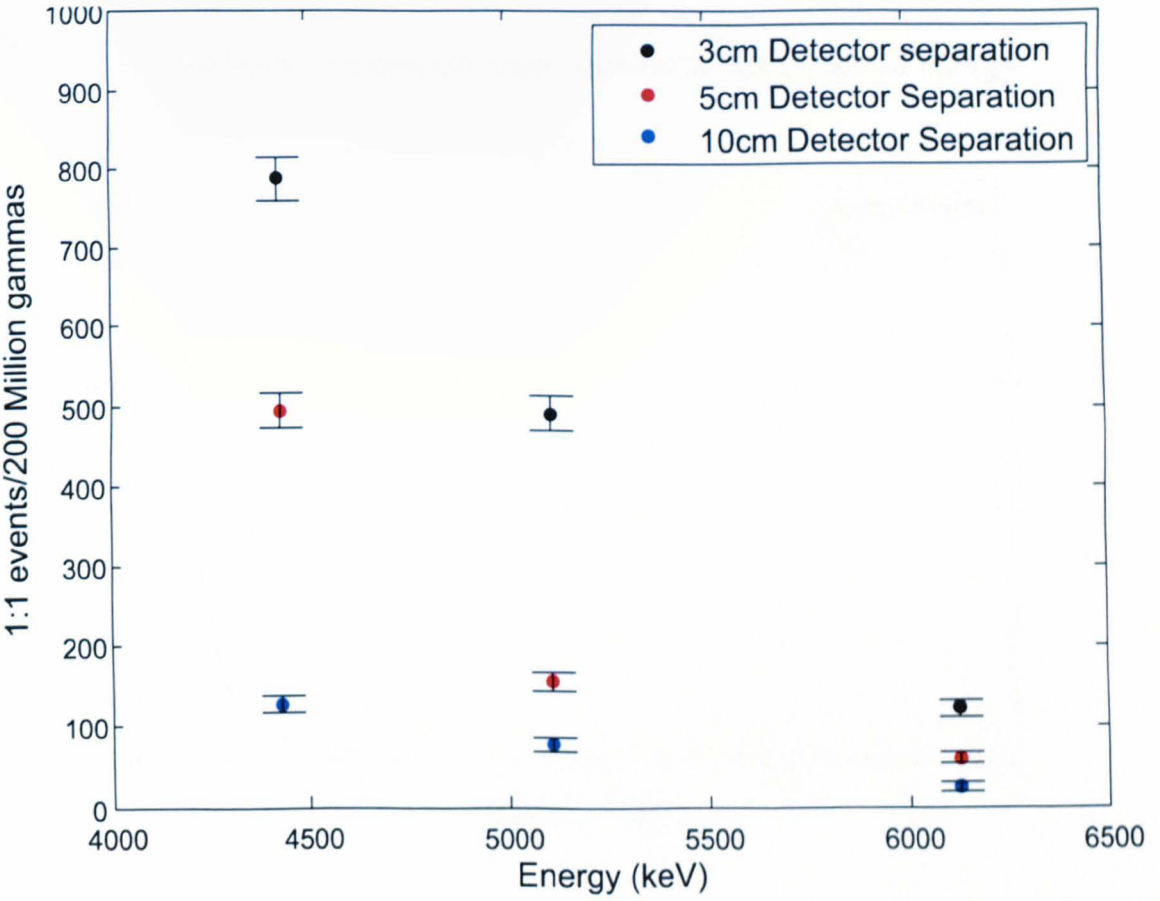

Figure 5.2: Plot showing the 4.430 MeV, 5.110 MeV and 6.130 MeV 1:1 Compton efficiencies of the GeGe system in Compton imaging mode as a function of energy with detector separations of 30mm, 50mm and 100mm.

be larger than that of Ge. A larger probability of their being more photoelectric absorbtion events is a desired feature of an absorber detector. A comparison of the photoelectric absorbtion cross sections of Ge and CsI is illustrated by Figure 5.3.

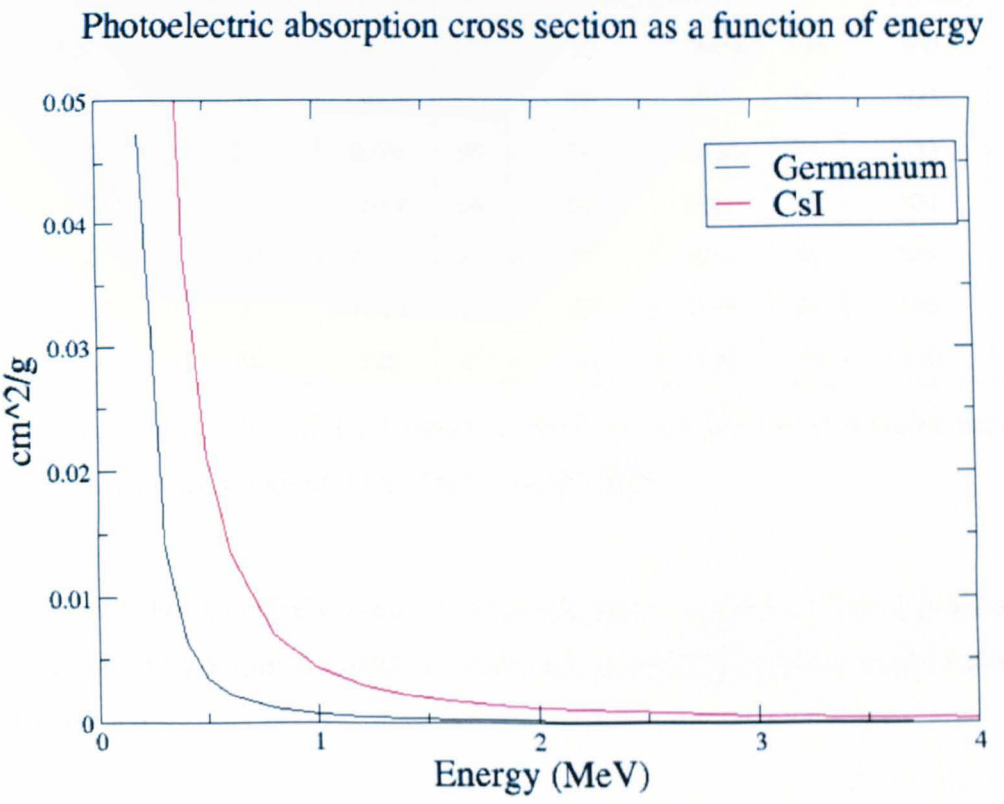

Figure 5.3: Plot showing the photoelectric absorbtion cross sections of Ge and CsI as a function of gamma-ray energy. [NIST]

5.2.1 GeCsI Compton efficiency

Similar to the GeGe Geant4 simulations, GeCsI data were collected for a number of point source energies which include 0.662 MeV, 1.332 MeV, 2.310 MeV, 4.430 MeV, 5.110 MeV and 6.130 MeV. Each of these energies were simulated with a 30mm, 50mm and 100mm detector separation. The number of 1:1 events for 200 million primary gamma rays over a different detector separation for GeCsI is given by Table 5.2.

Similarly for GeCsI, comparing this system to a GeGe system it can be seen in Table 5.2 that as a function of detector separation the number of 1:1 Compton events reduces

Energy (MeV)	Sep(mm)	Events	±	Sep(mm)	Events	±	Sep(mm)	Events	±
0.662	30	30016	173	50	18488	136	100	10817	104
1.332	30	13628	117	50	8055	90	100	3146	56
1.640	30	9070	95	50	5549	74	100	2272	48
2.310	30	4689	68	50	2868	54	100	1090	33
4.430	30	1823	43	50	1251	35	100	161	13
5.110	30	1513	39	50	312	18	100	104	10
6.130	30	229	15	50	129	11	100	35	6

Table 5.2: The number of 1:1 Compton events as a function of detector separation for GeCsI. Energy range of 0.662 MeV - 6.130 MeV.

significantly. For the GeCsI configuration, efficiency curves have been generated and are illustrated by Figure 5.4 with a closer look at 4.430 MeV to 6.130 MeV illustrated by Figure 5.5.

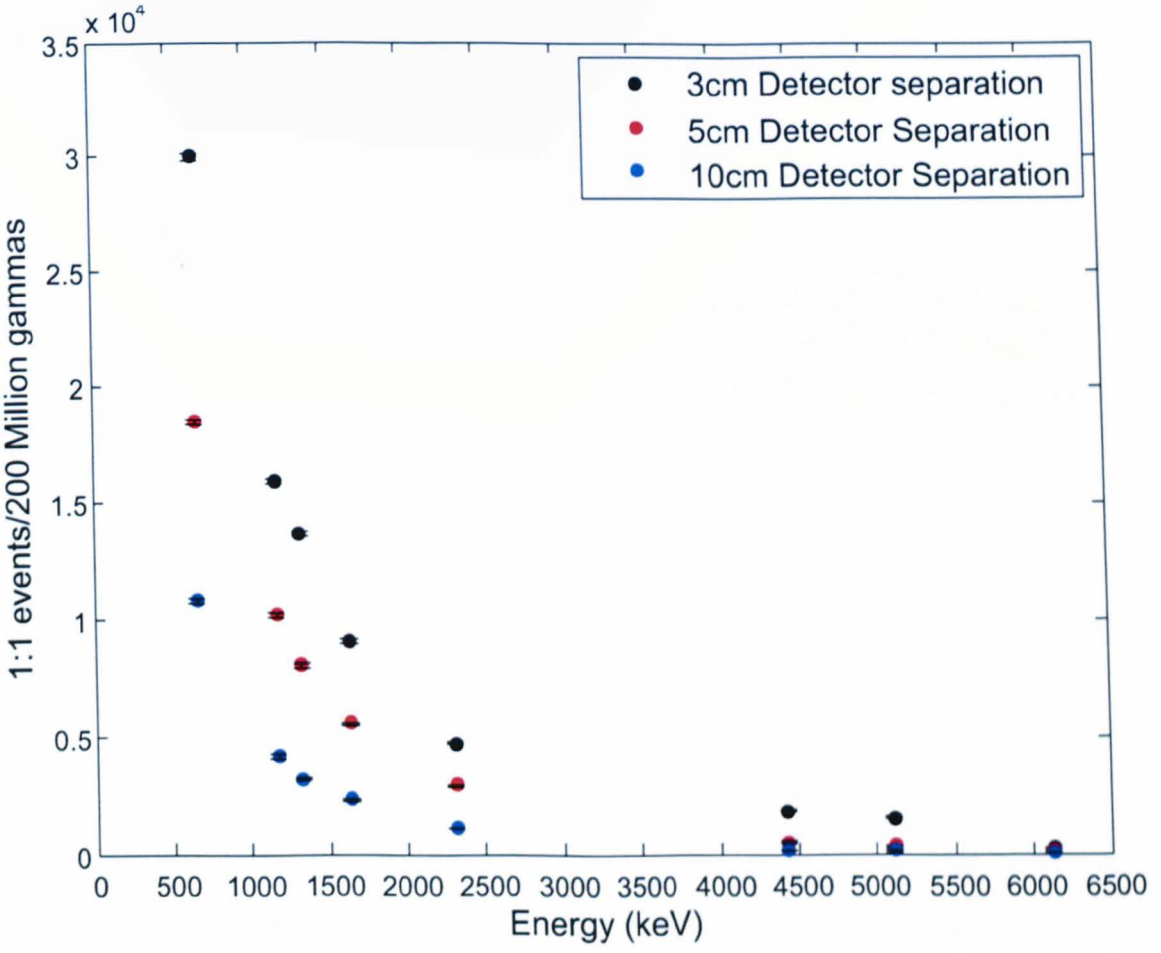

Figure 5.4: Plot showing the overall 1:1 Compton efficiency of the GeCsI system in Compton imaging mode as a function of energy with detector separations of 30mm, 50mm and 100mm

5.2.2 Comparison of GeGe and GeCsI Compton efficiency

GEANT4 simulations of 200 million primary gamma rays have been run for both detector configurations. By directly comparing Table 5.1 and Table 5.2 we can see that the GeCsI system has a systematically higher 1:1 Compton efficiency irrespective of the detector separation.

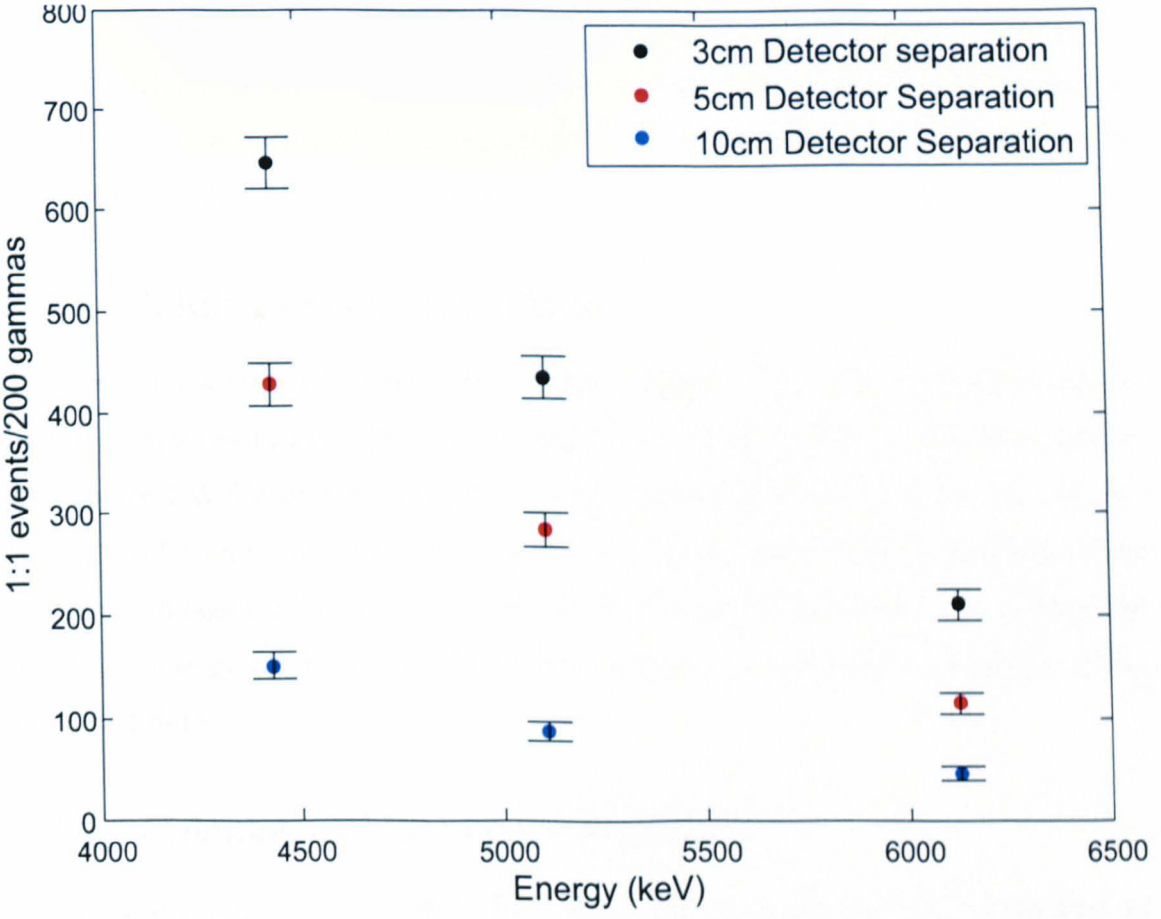

Figure 5.5: Plot showing the 4.430 MeV, 5.110 MeV and 6.130 MeV 1:1 Compton efficiencies of the GeCsI system in Compton imaging mode as a function of energy with detector separations of 30mm, 50mm and 100mm.

5.3 Geant4 simulations of experimental energies

Thus far, this chapter has compared the 1:1 Compton efficiencies of both the GeGe and GeCsI systems over a range of energies as a function of detector separation. As would be expected, the efficiency degraded as the detector separation increased. The GeCsI system is shown to be consistently more efficient than the GeGe configuration, yet the efficiency is still very low at the higher energies. Before any Geant4 simulated images can be reconstucted, it is important that the simulated data is representative of the data obtained in the experiments.

5.3.1 Adding energy resolution

The precision with which a detector is able to identify the energy deposited is given by the energy resolution. The energy resolution is one of the key contributors of the final image FWHM of any Compton image. Geant4 software does not account for energy resolution in any detectors and so this must be applied to all simulated data before any image can be reconstructed. This section will now discuss the method by which the energy resolution and % energy resolution is calculated and added to the simulated data.

5.3.2 Calculating the energy resolution

The energy resolution of a 0.662 MeV photopeak is quoted as 10% [SCIONIX] in a CsI detector built to the specifications of the simulated CsI detector. Work by [Gas09] suggests that the % energy resolution of a CsI detector as a function of energy deposited follows a rule of equation 5.1.

$$\% = \frac{1}{\sqrt{E_\gamma}} \tag{5.1}$$

Using equation 5.1 over all of the energies used in this chapter we can calculate the % energy resolution for every energy deposited in the CsI detector and also calculate an energy resolution value as a function of energy. The % energy resolution as a function

of energy for this CsI detector is illustrated by Figure 5.6 and the energy resolution of the CsI detector as a function of energy illustrated by Figure 5.7.

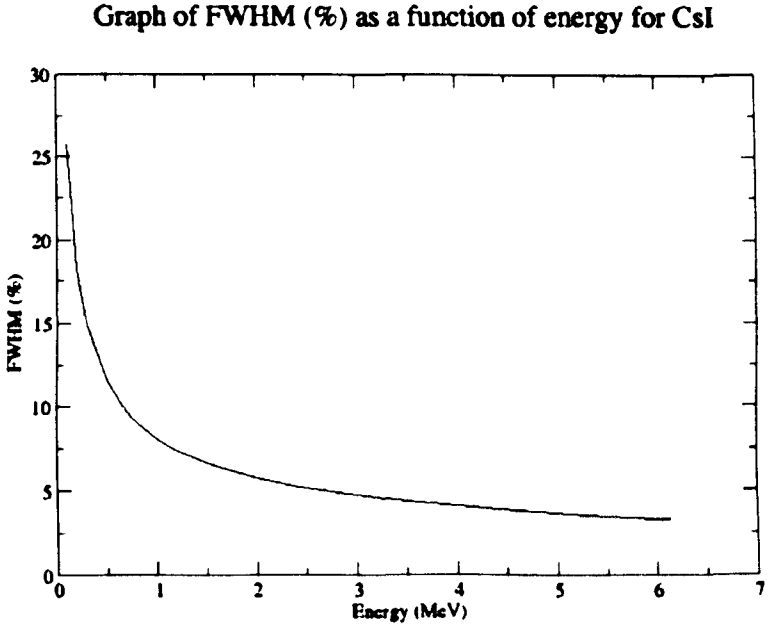

Figure 5.6: Plot showing % energy resolution of a CsI detector as a function of energy

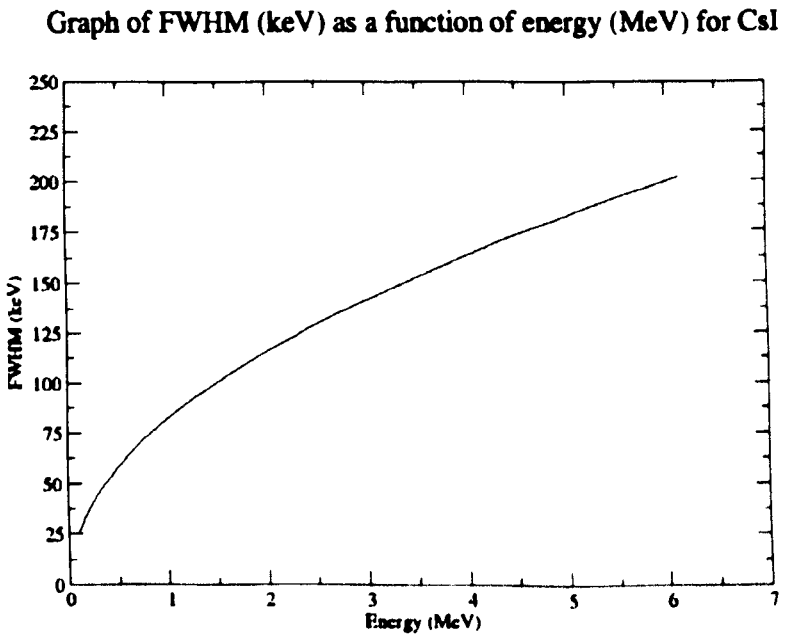

Figure 5.7: Plot showing energy resolution of a CsI detector as a function of energy

Experimentally, the energy resolution of the planar Ge detector has been measured up to 1.408 MeV. Using the rule of equation 5.1, and inputing the % energy resolution values, it is possible to calculate the % energy resolution values over the range of energies we are interested in for the simulations. Once all of the energy resolution values are calculated then the information is entered into the data analysis process and every energy deposited in the Ge and CsI detectors over both geometries is subject to an applied energy resolution value. The % energy resolution for a Ge detector as a function of energy is illustrated in Figure 5.8, and the energy resolution is illustrated in Figure 5.9. The data points at lower energies represent experimental values.

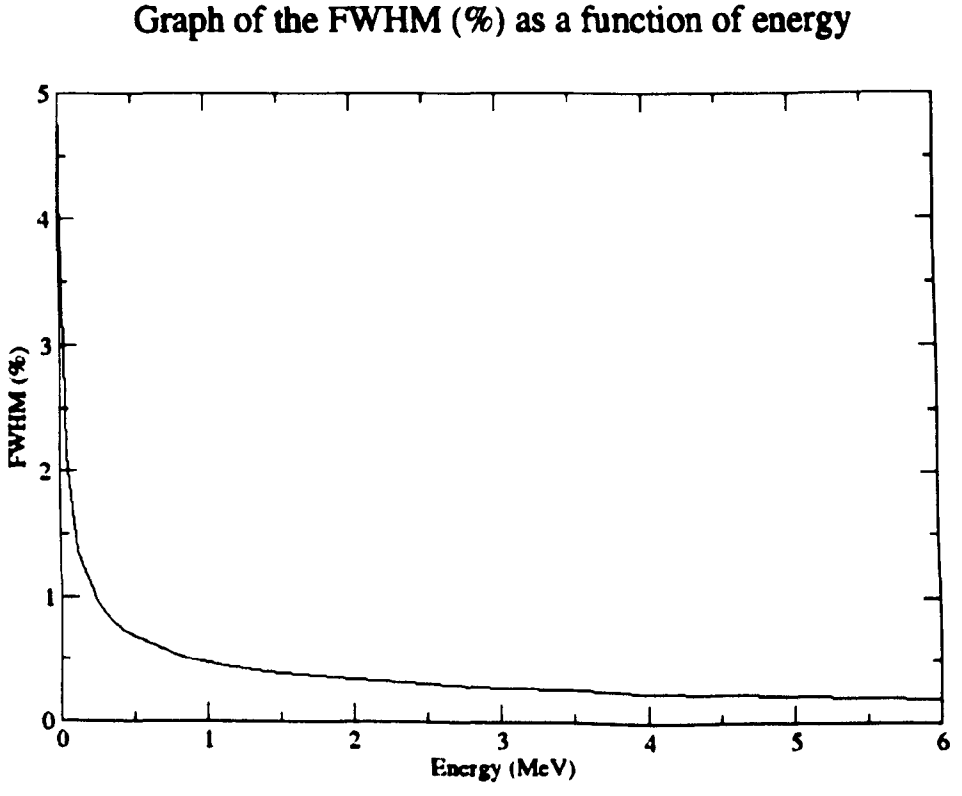

Figure 5.8: Plot showing % energy resolution of a Ge detector as a function of energy

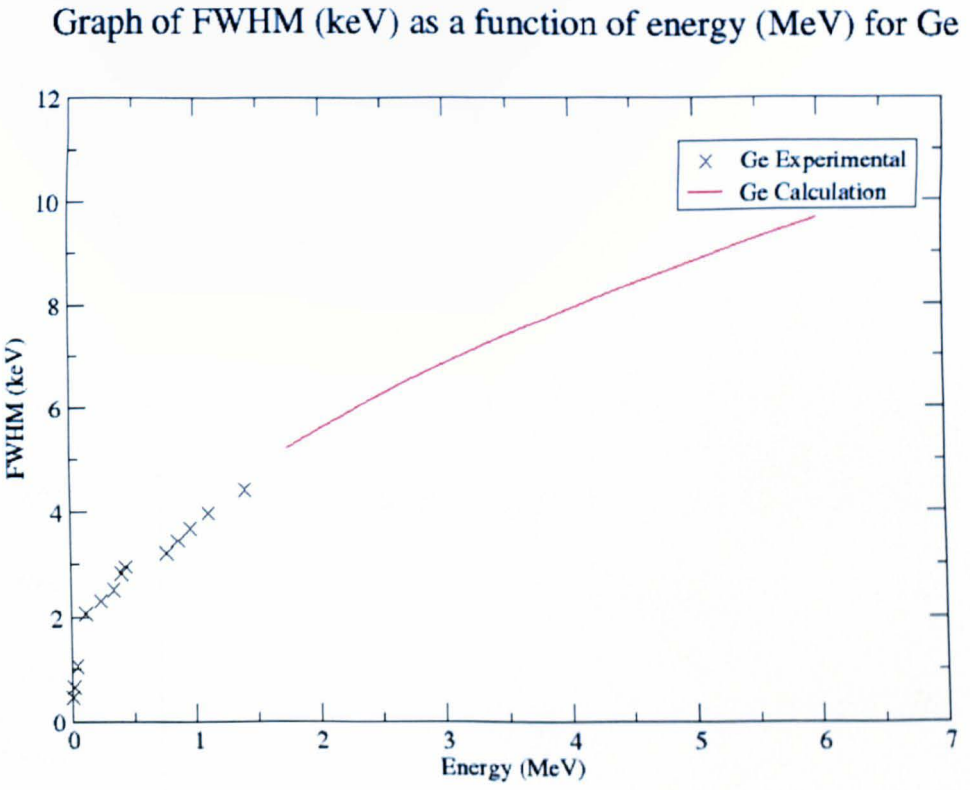

Figure 5.9: Plot showing energy resolution of a Ge detector as a function of energy. The data points at lower energies represent experimental values.

An energy spectrum from the Compton imaging of a 4.430 MeV point source using the GeGe configuration is given by Figure 5.10. Figure 5.11 illustrates the comparison between the 4.430 MeV photopeak before and after any energy resolution blurring has been added to the data.

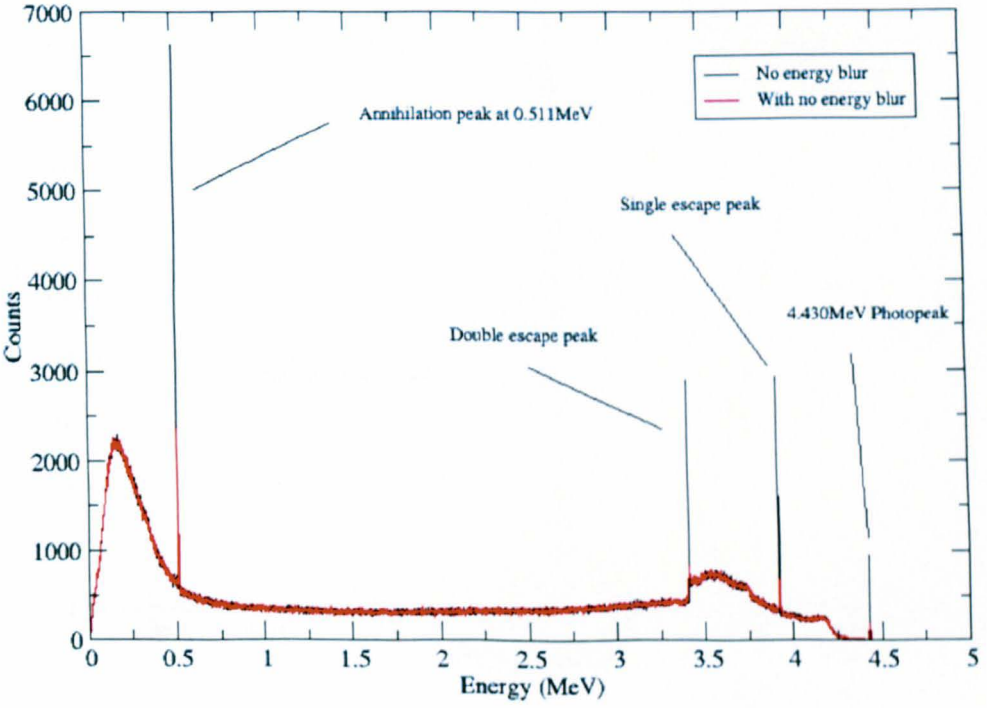

Figure 5.10: Output spectrum of 4.430 MeV 1:1 Compton data

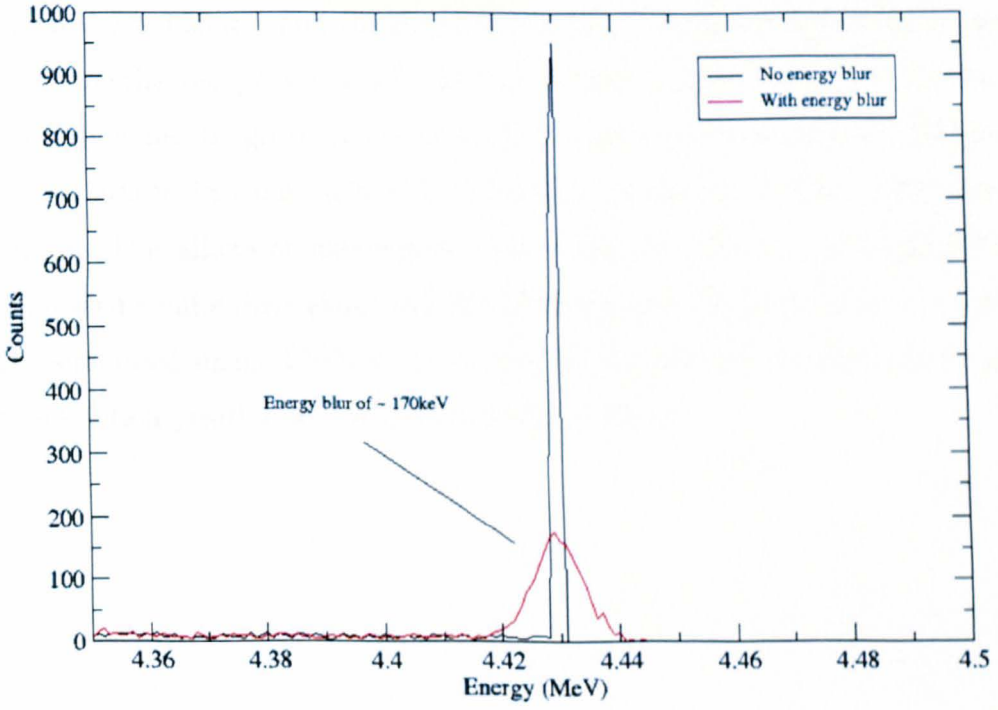

Figure 5.11: The 4.430 MeV photopeak, before and after energy resolution blurring has been added to the 1:1 Compton data.

5.3.3 GEANT4 simulation analysis

During the experimental data analysis, the lorentzian fit over a quadratic background was done with 300 channels. It is seen in the experimental X and Y projections that the fit doesn't include the entire of the peak under analysis. For the simulated work throughout the rest of this thesis the results have been compiled using a 200 channel fit. This lowers the amount of background and allows the lorenztian fit over a quadratic background to analyse more of the peak height. Compton images of a 0.662 MeV point source and the respective X and Y projections have been generated to compare the results for a 300 channel fit and a 200 channel fit for the GeGe configuration and are given by Figure 5.12. It is seen that the image FWHM improves from 22.2 mm to 18.1 mm in X and 22.3 mm to 18.8mm in Y when a 200 channel fit is applied. This allows an assumption of a $\pm$ 2.0 mm error on the image FWHM for all simulated results throughout the rest of this thesis. No other errors are attributed to the simulated image FWHM or reconstructed positions as every source position and interaction position within the detectors is exact.

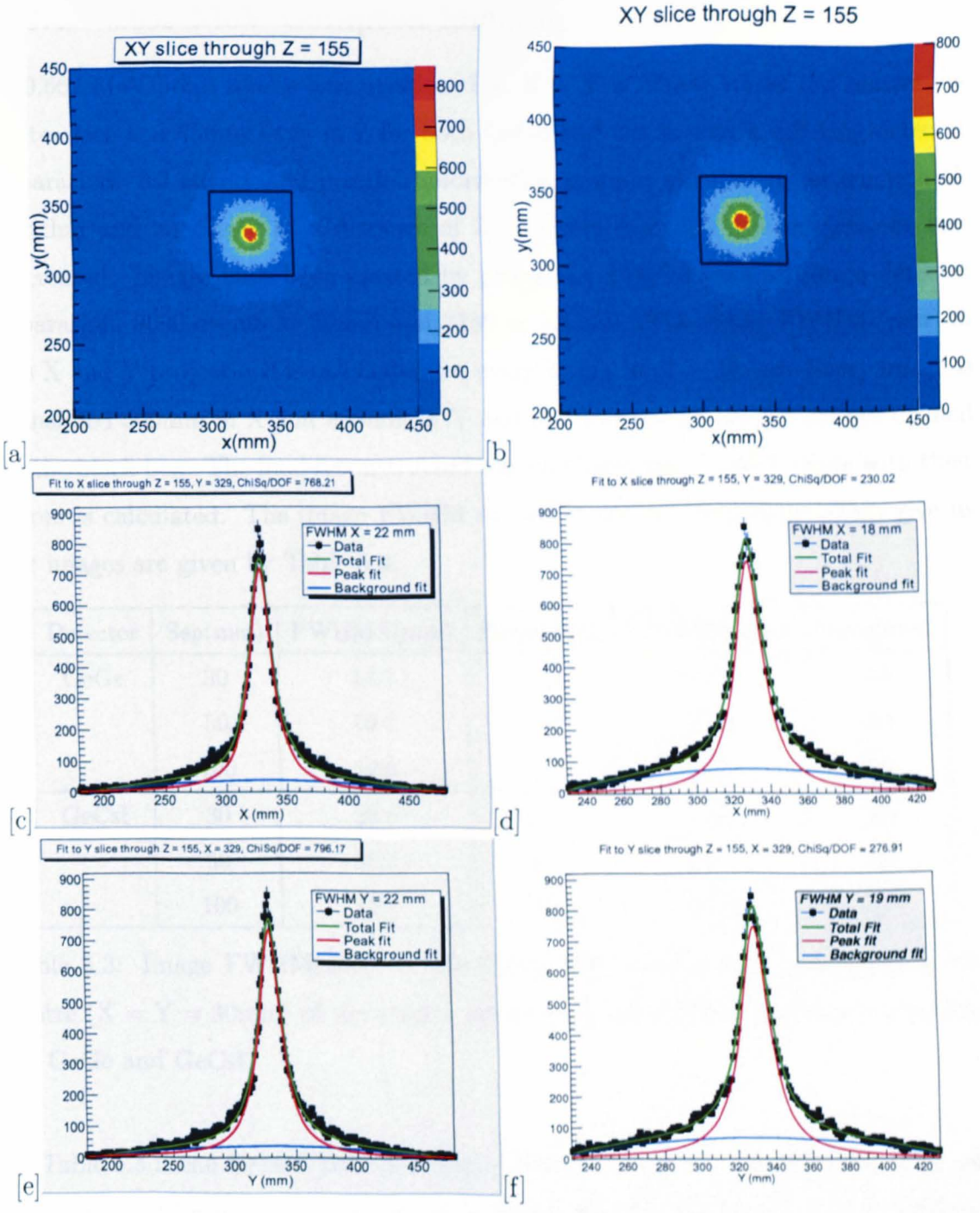

Figure 5.12: Simulated images of a 0.662 MeV point source positioned 45mm from the scatter detector with X = Y = 30mm with a detector separation of 30mm. 300 channel fit GeGe Compton image [a], X [c] and Y [e], 200 channel fit GeGe Compton image [b], X [d], Y [f].

5.3.4 0.662 MeV Compton imaging

A 0.662 MeV point source was positioned at X = Y = 30mm across the scatter detector face and 45mm away in Z for both GeGe and GeCsI over a differing detector separation. All energy and position information is input into the reconstruction algorithm and an ellipse at a distance of Z = 45mm from the scatter detector face is created. Images have been created by projecting 14500 events at 30mm detector separation, 9000 events at 50mm and 3750 at 100mm. The image FWHM (mm) in the X and Y projections is calculated for every image for Z = 45mm. Every image is translated 300mm in X and 300mm in Y and the detector position is always defined by the black box. The final reconstructed source position in X and Y along with their errors is calculated. The image FWHM for the X and Y projections which give us our images are given by Table 5.3.

Detector	Sep(mm)	FWHMX(mm)	Error(mm)	FWHMY(mm)	Error(mm)
GeGe	30	18.1	2.0	18.8	2.0
	50	15.4	2.0	15.6	2.0
	100	12.6	2.0	12.8	2.0
GeCsI	30	20.6	2.0	19.9	2.0
	50	16.5	2.0	16.8	2.0
	100	12.7	2.0	13.7	2.0

Table 5.3: Image FWHM(mm) for the 0.662 MeV point source positioned at the centre (X = Y = 30mm) of the scatter detector face at differing detector separations for GeGe and GeCsI.

In Table 5.3 it can be seen that the image FWHM in X and Y of 0.662 MeV improves from 18.1 ± 2.0 mm and 18.8 ± 2.0 mm at 30mm detector separation to 12.6 ± 2.0 mm and 12.8 ± 2.0 mm at 100mm detector separation for GeGe. The image FWHM in X and Y improves from 20.6 ± 2.0 mm and 19.9 ± 2.0 mm at 30mm detector separation to 12.8 ± 2.0 mm and 13.7 ± 2.0 mm at 100mm detector separation for GeCsI. These improvements in image FWHM for both the GeGe and GeCsI configurations as a

function of detector separation can be visualised in Figure 5.13, The reconstructed images for 0.662 MeV along with their associated X and Y projections are given by Figures 5.14 (30mm), 5.15 (50mm) and 5.16 (100mm). The reconstructed positions for the 0.662 MeV point source positioned at the centre (X = Y = 30mm) of the scatter detector face at different detector separations for both detector configurations are given in Table 5.4.

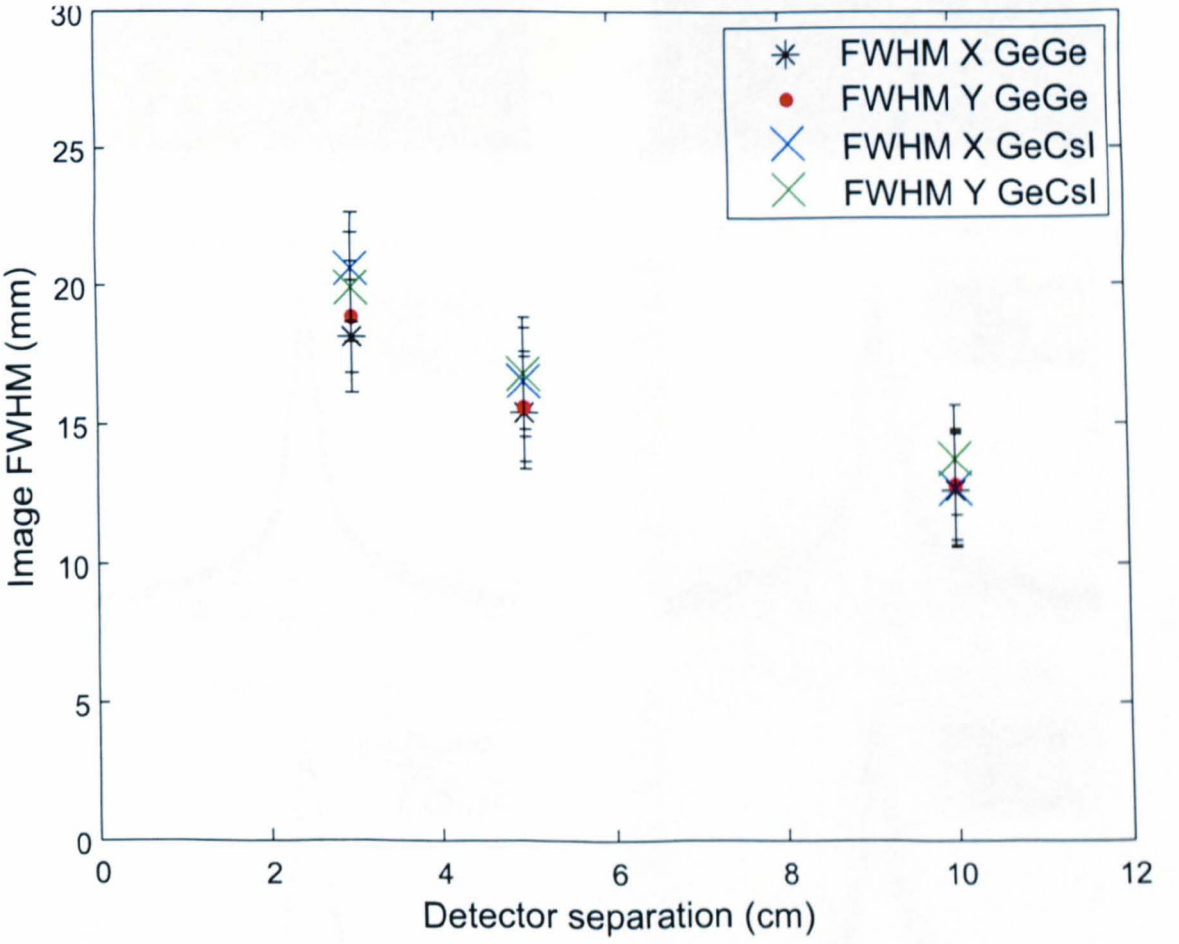

Figure 5.13: Image FWHM (mm) for the X and Y projections of the GeGe and GeCsI configurations. Given over the 30mm, 50mm and 100mm detector separations. The gamma point source energy is 0.662 MeV

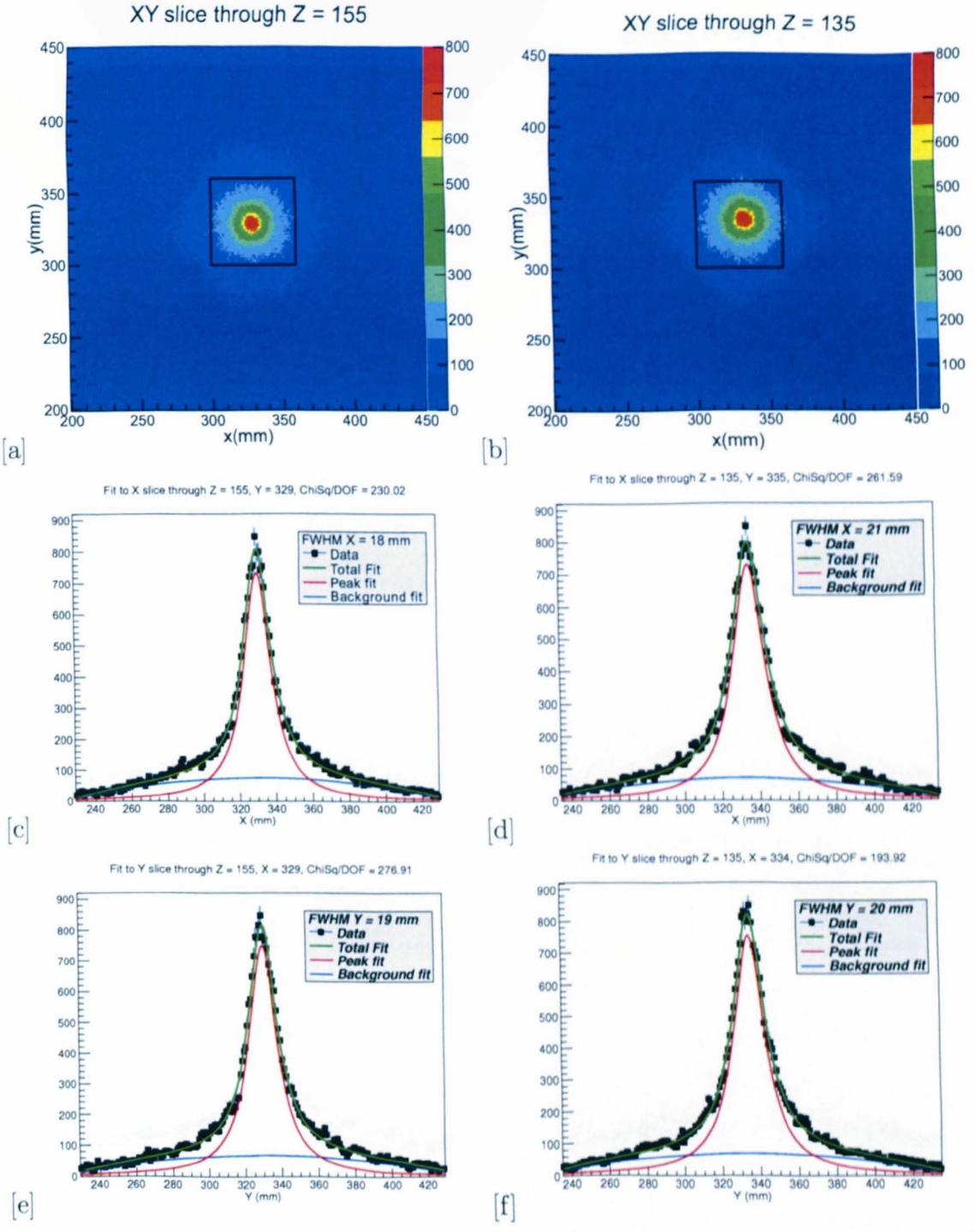

Figure 5.14: Simulated images of a 0.662 MeV point source positioned 45mm from the scatter detector with X = Y = 30mm with a detector separation of 30mm. GeGe Compton image [a], X [c] and Y [e], GeCsI Compton image [b], X [d], Y [f].

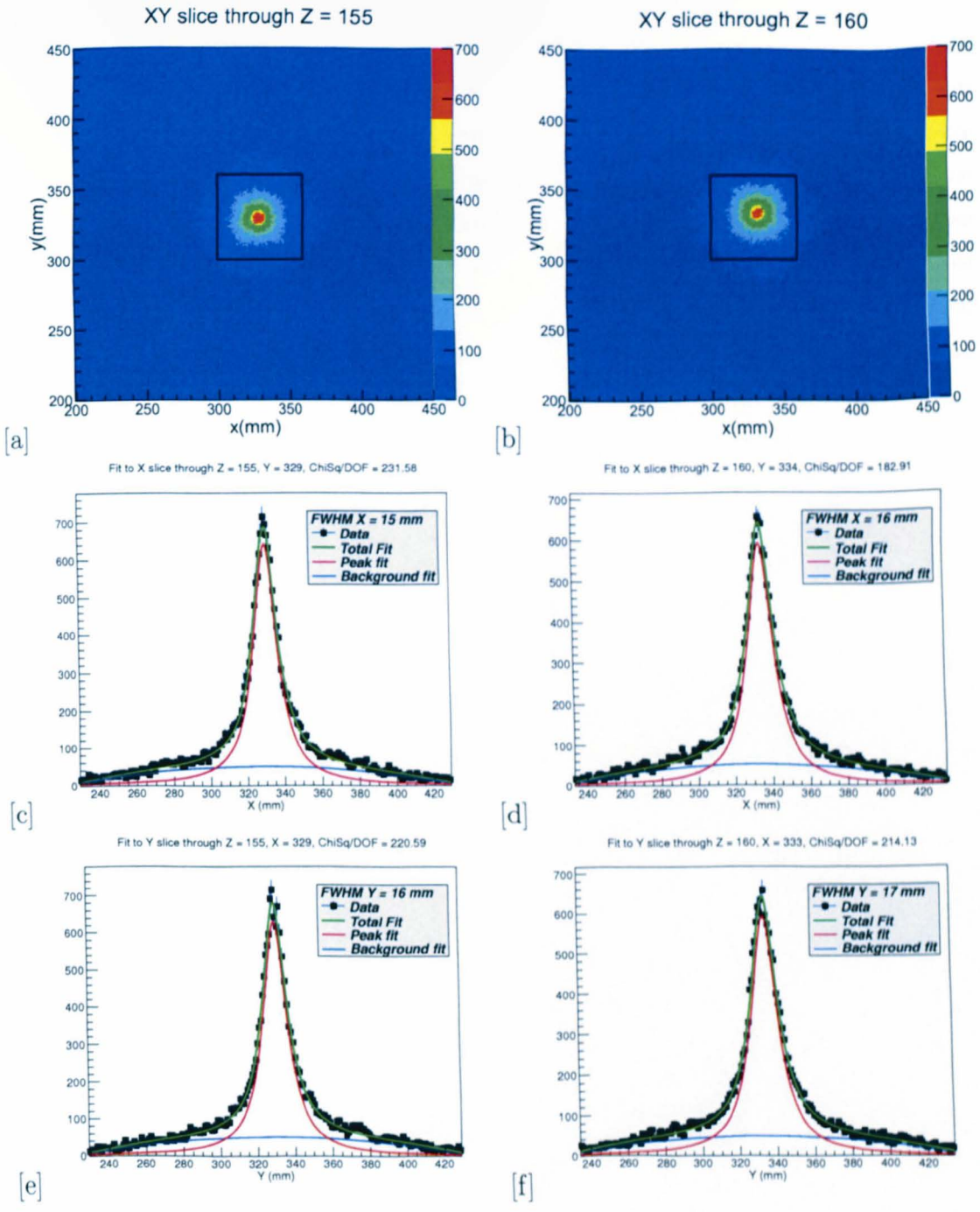

Figure 5.15: Simulated images of a 0.662MeV point source positioned 45mm from the scatter detector with X = Y = 30mm with a detector separation of 50mm. GeGe Compton image [a], X [c] and Y [e], GeCsI Compton image [b], X [d], Y [f].

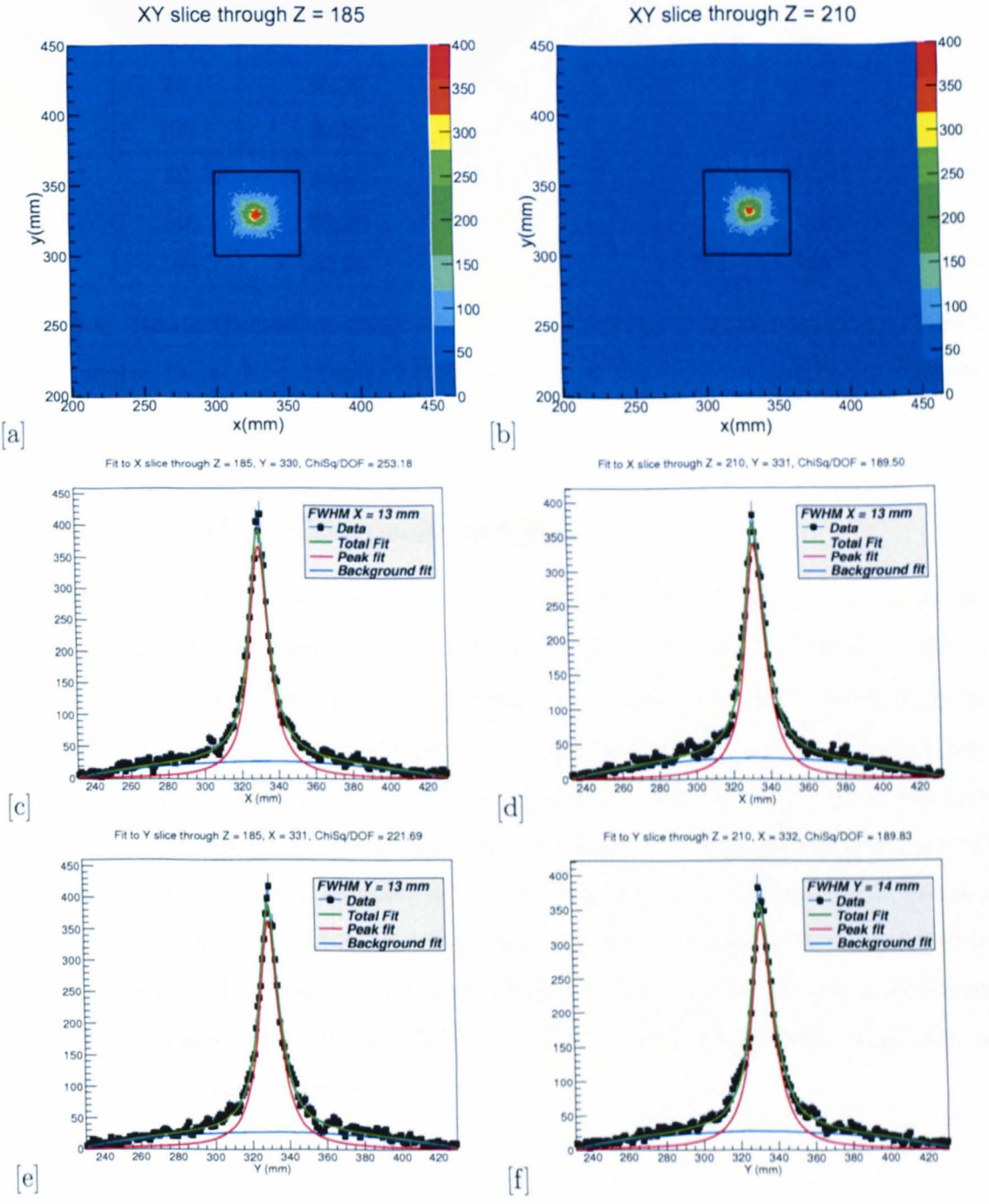

Figure 5.16: Simulated images of a 0.662 MeV point source positioned 45mm from the scatter detector with X = Y = 30mm with a detector separation of 100mm. GeGe Compton image [a], X [c] and Y [e], GeCsI Compton image [b], X [d], Y [f].

Detector	Sep(mm)	X(mm),Y(mm)	Rec X(mm)	Error(mm)	Rec Y(mm)	Error(mm)
GeGe	30	30,30	30.1	2.0	29.9	2.0
	50	30,30	30.0	2.0	30.0	2.0
	100	30,30	30.2	2.0	29.7	2.0
GeCsI	30	30,30	34.4	2.0	34.4	2.0
	50	30,30	34.0	2.0	34.0	2.0
	100	30,30	32.5	2.0	32.3	2.0

Table 5.4: Reconstructed positions(mm) for a 0.662 MeV point source positioned at the centre (X = Y = 30mm) of the scatter detector face at differing detector separations.

5.3.5 1.332 MeV Compton imaging

A 1.332 MeV point source was positioned at X = Y = 30mm across the scatter detector face and 45mm away in Z for both GeGe and GeCsI over a differing detector separation. All energy and position information is input into the reconstruction algorithm and an ellipse at a distance of Z = 45mm from the scatter detector face is created. Images have been created by projecting 5500 events at 30mm detector separation, 3300 events at 50mm and 1200 at 100mm. The image FWHM (mm) in the X and Y projections is calculated for every image for Z = 45mm. Every image is translated 300mm in X and 300mm in Y and the detector position is always defined by the black box. The final reconstructed source position in X and Y along with their errors is calculated. The image FWHM for the X and Y projections which give us our images are given by Table 5.5.

Detector	Sep(mm)	FWHMX(mm)	Error(mm)	FWHMY(mm)	Error(mm)
GeGe	30	18.8	2.0	20.6	2.0
	50	14.3	2.0	14.6	2.0
	100	12.5	2.0	13.5	2.0
GeCsI	30	21.1	2.0	17.9	2.0
	50	16.7	2.0	16.9	2.0
	100	13.4	2.0	12.7	2.0

Table 5.5: Image FWHM(mm) for the 1.332 MeV point source positioned at the centre (X = Y = 30mm) of the scatter detector face at differing detector separations for GeGe and GeCsI.

In Table 5.5 it can be seen that the image FWHM in X and Y of 1.332 MeV improves from 18.8 ± 2.0 mm and 20.6 ± 2.0 mm at 30mm detector separation to 12.5 ± 2.0 mm and 13.5 ± 2.0 mm at 100mm detector separation for GeGe. The image FWHM in X and Y improves from 21.1 ± 2.0 mm and 17.9 ± 2.0 mm at 30mm detector separation to 13.4 ± 2.0 mm and 12.7 ± 2.0 mm at 100mm detector separation for GeCsI. These improvements in image FWHM for both the GeGe and GeCsI configurations as a function of detector separation can be visualised in Figure 5.17, The reconstructed images for 1.332 MeV along with their associated X and Y projections are given by Figures 5.18 (30mm), 5.19 (50mm) and 5.20 (100mm). The reconstructed positions for the 1.332 MeV point source positioned at the centre (X = Y = 30mm) of the scatter detector face at different detector separations for both detector configurations are given in Table 5.6.

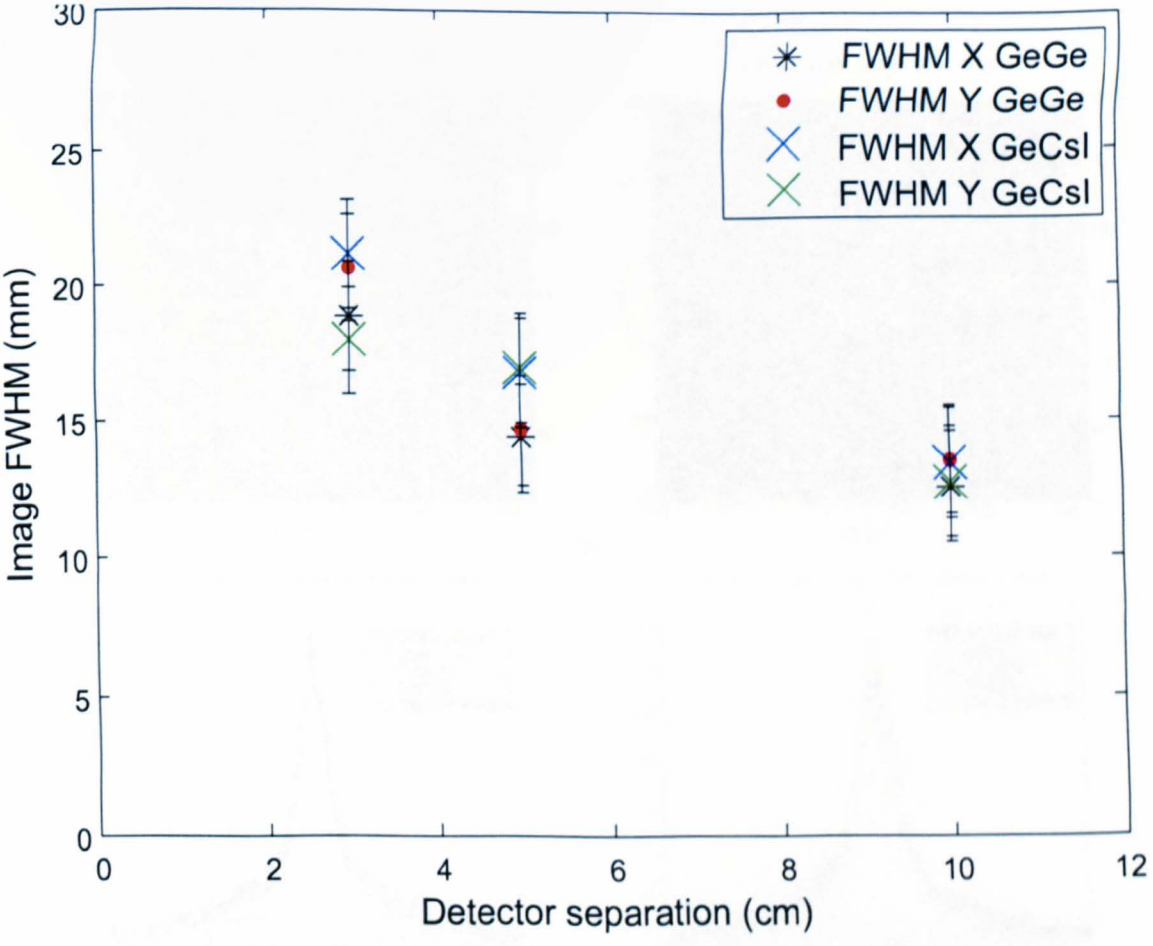

Figure 5.17: Image FWHM (mm) for the X and Y projections of the GeGe and GeCsI configurations. Given over the 30mm, 50mm and 100mm detector separations. The gamma point source energy is 1.332 MeV

The reconstructed positions as a function of detector separation of the 1.332 MeV point source are given by Table 5.6. Figure 5.21 illustrates the reconstructed position deviation from the X = Y = 30mm position across the scatter detector face for both GeGe and GeCsI and it can be seen that there is a very small amount of deviation from 30mm to 100mm detector separation. One thing of note is that there is a small deviation in both X and Y in the GeCsI positions, yet it seems to improve with a larger detector separation.

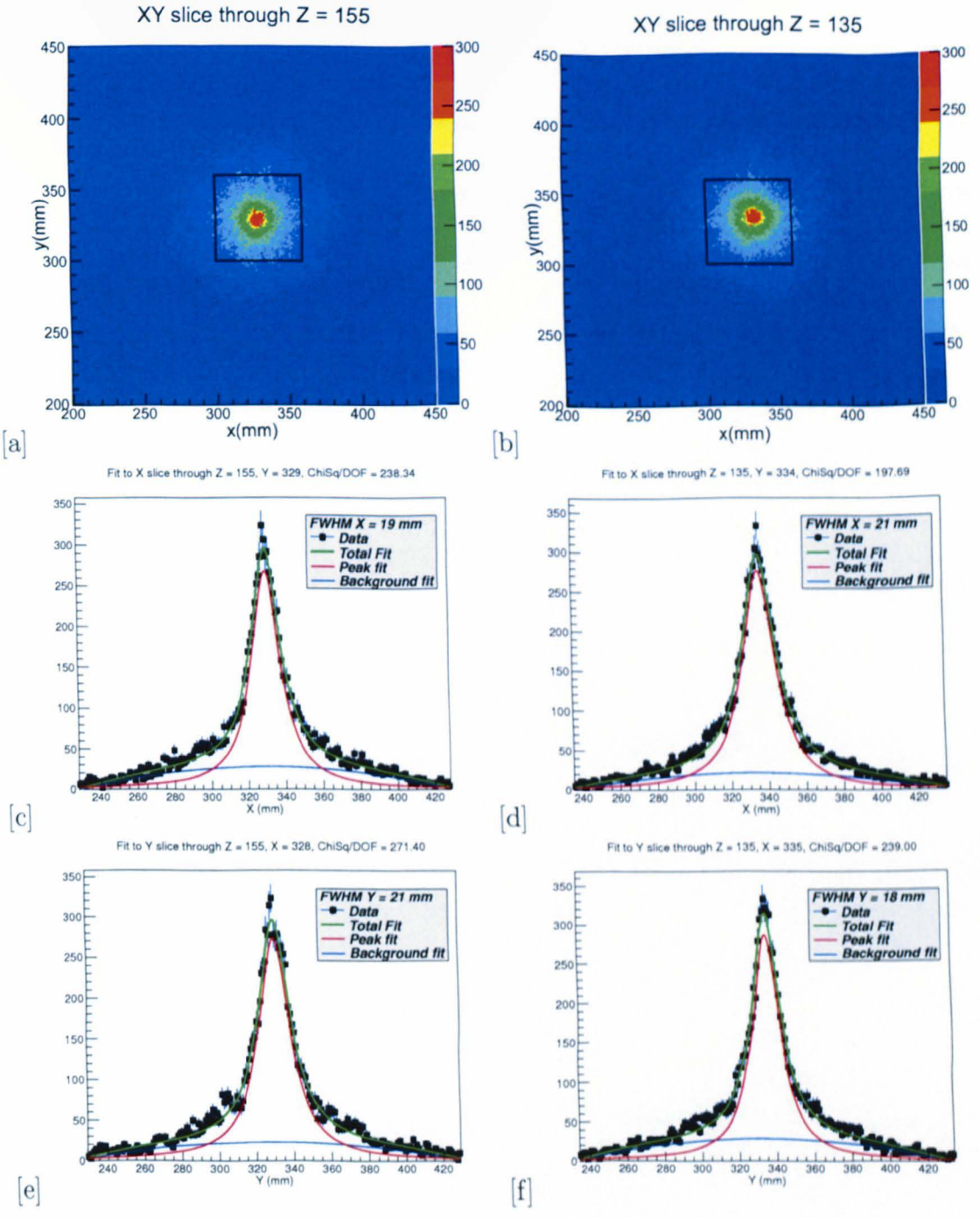

Figure 5.18: Simulated images of a 1.332 MeV point source positioned 45mm from the scatter detector with X = Y = 30mm with a detector separation of 30mm. GeGe Compton image [a], X [c] and Y [e], GeCsI Compton image [b], X [d], Y [f].

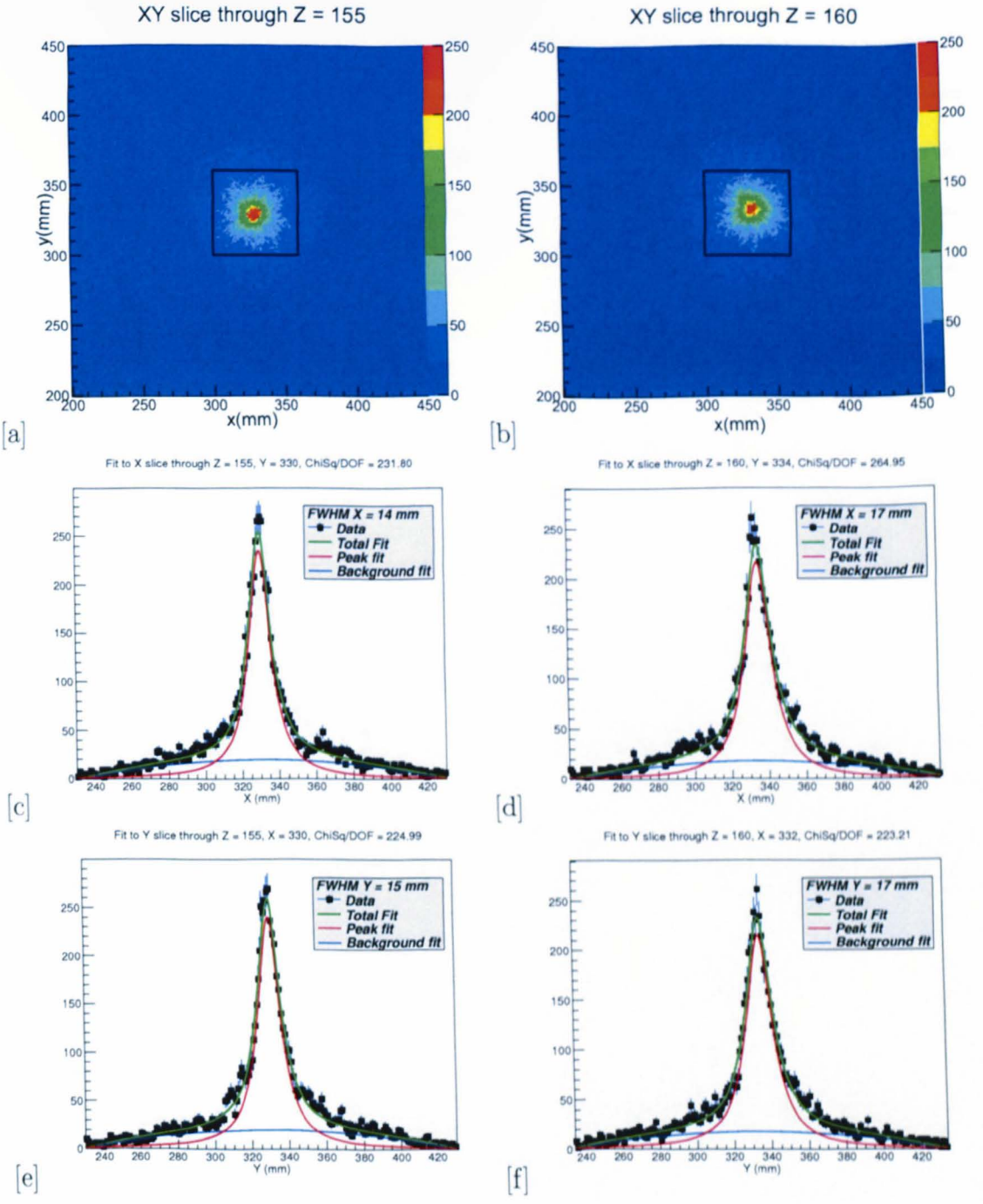

Figure 5.19: Simulated images of a 1.332 MeV point source positioned 45mm from the scatter detector with X = Y = 30mm with a detector separation of 50mm. GeGe Compton image [a], X [c] and Y [e], GeCsI Compton image [b], X [d], Y [f].

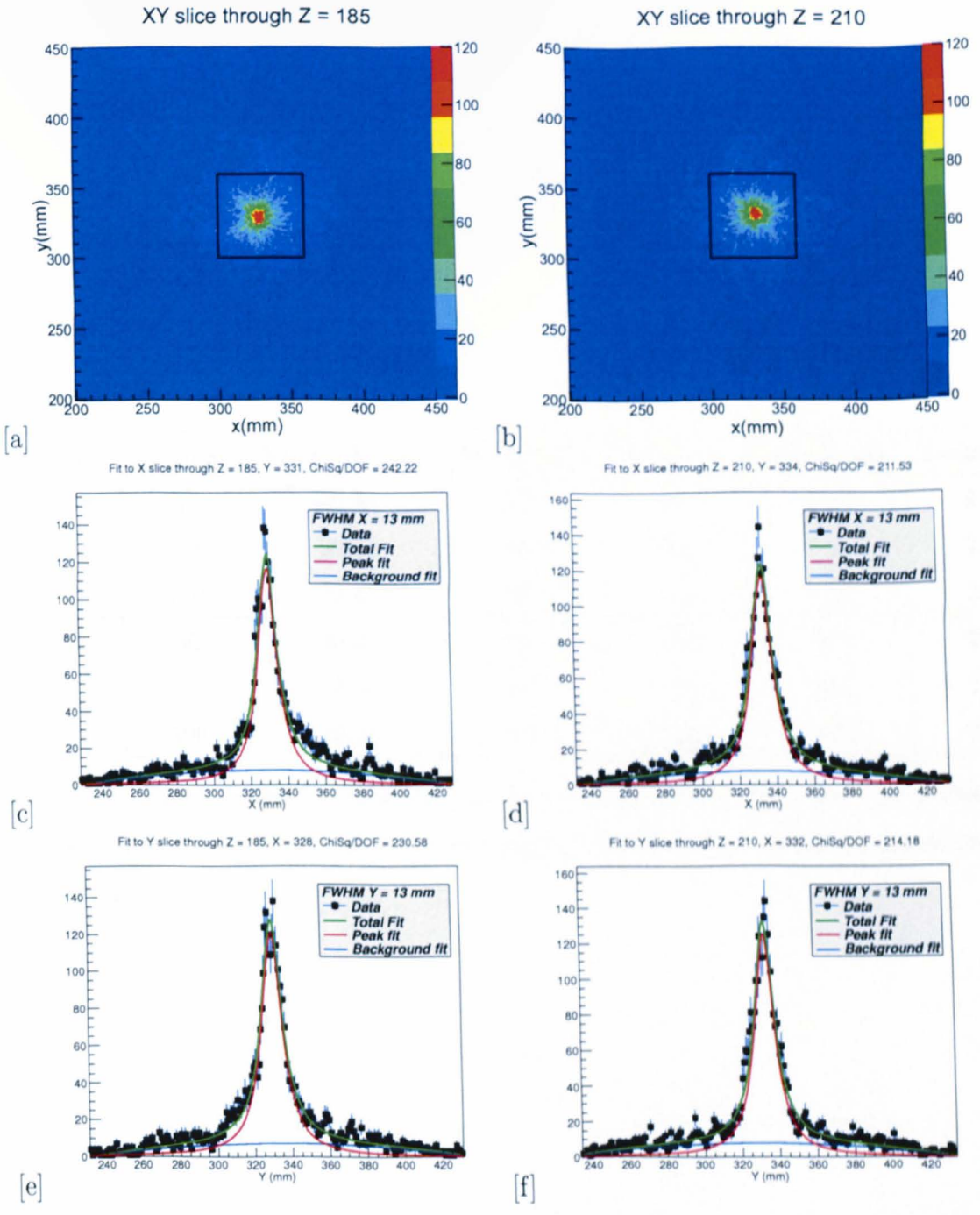

Figure 5.20: Simulated images of a 1.332 MeV point source positioned 45mm from the scatter detector with X = Y = 30mm with a detector separation of 100mm. GeGe Compton image [a], X [c] and Y [e], GeCsI Compton image [b], X [d], Y [f].

Detector	Sep(mm)	X(mm),Y(mm)	Rec X(mm)	Error(mm)	Rec Y(mm)	Error(mm)
GeGe	30	30,30	29.8	2.0	29.9	2.0
	50	30,30	29.9	2.0	29.9	2.0
	100	30,30	29.6	2.0	29.6	2.0
GeCsI	30	30,30	35.2	2.0	34.8	2.0
	50	30,30	34.8	2.0	34.3	2.0
	100	30,30	32.8	2.0	32.5	2.0

Table 5.6: Reconstructed positions(mm) for a 1.332 MeV point source positioned at the centre (X = Y = 30mm) of the scatter detector face at differing detector separations.

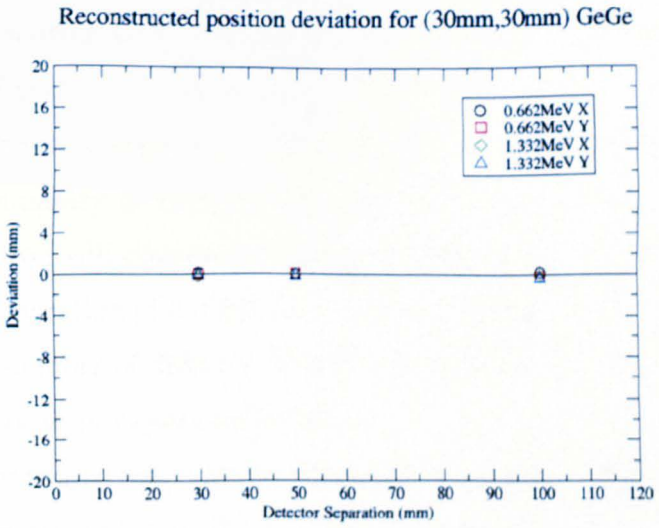

[a]

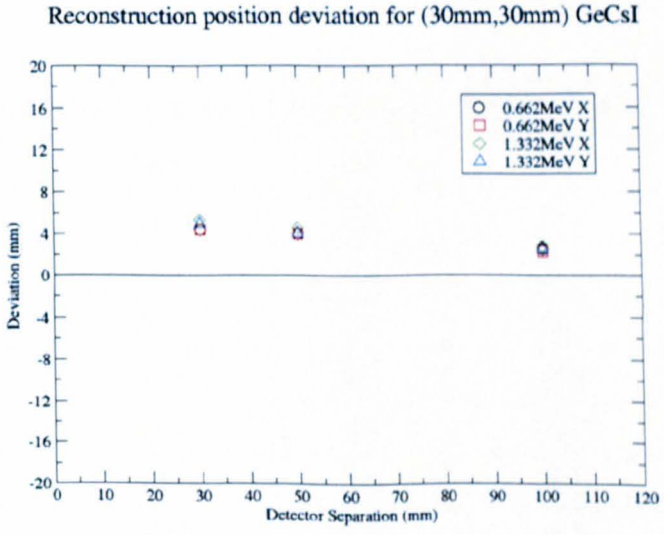

[b]

Figure 5.21: Reconstructed position deviation as a function of detector separation for both 0.662 MeV and 1.332 MeV for GeGe [a] and GeCsI [b].

5.3.6 Detector grid imaging

Section 4.3.3 discusses the improving image FWHM as a function of detector separation of two experimental measurements, including the positioning of 0.662 MeV and 1.332 MeV point sources at X = 10mm and Y = 50mm across the scatter detector face. It was found that even though there was an improvement in the image FWHM as a function of detector separation there seemed to be an asymmetry in the final images. This asymmetry is visually more prominent at the detector separation of 100mm. This section will discuss the effects on the imaging and image FWHM at 100mm detector separation of a 0.662 MeV point source positioned across the scatter detector face in a number of different X and Y locations. This assesment is to clarify whether asymmetry is an experimental effect.

A 0.662 MeV point source was positioned across the scatter detector face over a number of different locations at Z = 45mm. These locations are given in Table 5.8 along with all of the reconstructed positions. The source positions are illustrated in Figure 5.22.

X(mm),Y(mm)	FWHM X(mm)	Error(mm)	FWHM Y(mm)	Error(mm)
10,50	18.2	2.0	16.8	2.0
30,50	15.1	2.0	15.0	2.0
50,50	17.1	2.0	17.5	2.0
10,30	15.4	2.0	14.4	2.0
30,30	12.6	2.0	12.8	2.0
50,30	14.9	2.0	14.1	2.0
10,10	17.4	2.0	18.1	2.0
30,10	16.2	2.0	15.7	2.0
50,10	16.1	2.0	18.2	2.0

Table 5.7: Reconstructed image FWHM(mm) for a 0.662 MeV point source positioned across the scatter detector face over a number of different locations. Detector separation = 100mm.

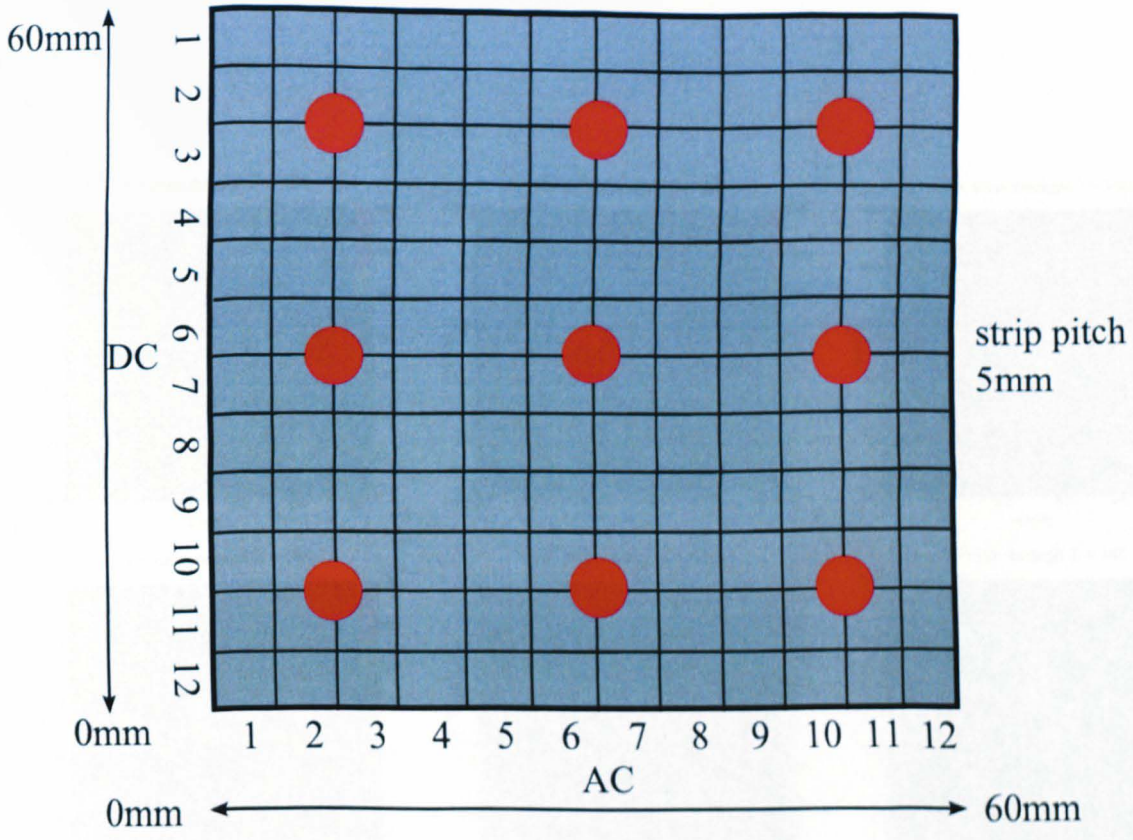

Figure 5.22: Schematic illustration of the multiple source positions across the scatter detector face.

The image FWHM for the X and Y projections of all of the simulated images are given by Table 5.7. It can be seen that there is some variation in image FWHM when the source is positioned near the outer edges of the scatter detector face. These simulated results show a similar asymmetry to the experimental results. This suggests that the asymmetry at the edge of the detector face is not governed by any experimental effects and can be seen to come from the source location and the detector positioning when reconstructing an image. All the reconstructed images and the X and Y projections are shown in Figure 5.23, Figure 5.24 and Figure 5.25 respectively.

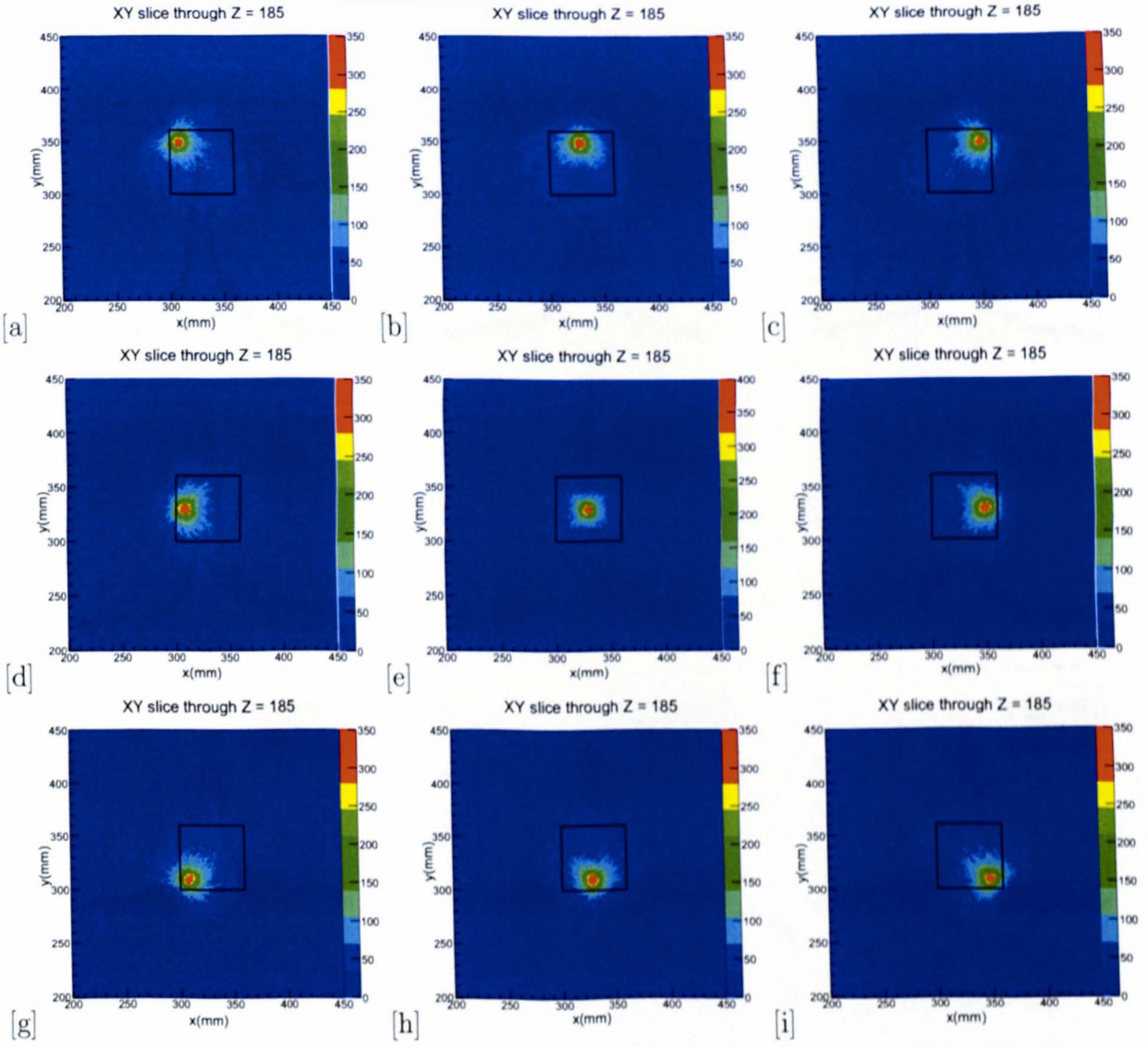

Figure 5.23: 0.662 MeV point source images. Source positions are (X,Y) 10mm,50mm [a], 30mm,50mm [b], 50mm,50mm [c], 10mm,30mm [d], 30mm,30mm [e], 50mm,30mm [f], 10mm,10mm [g], 30mm,10mm [h] and 50mm,10mm [i].

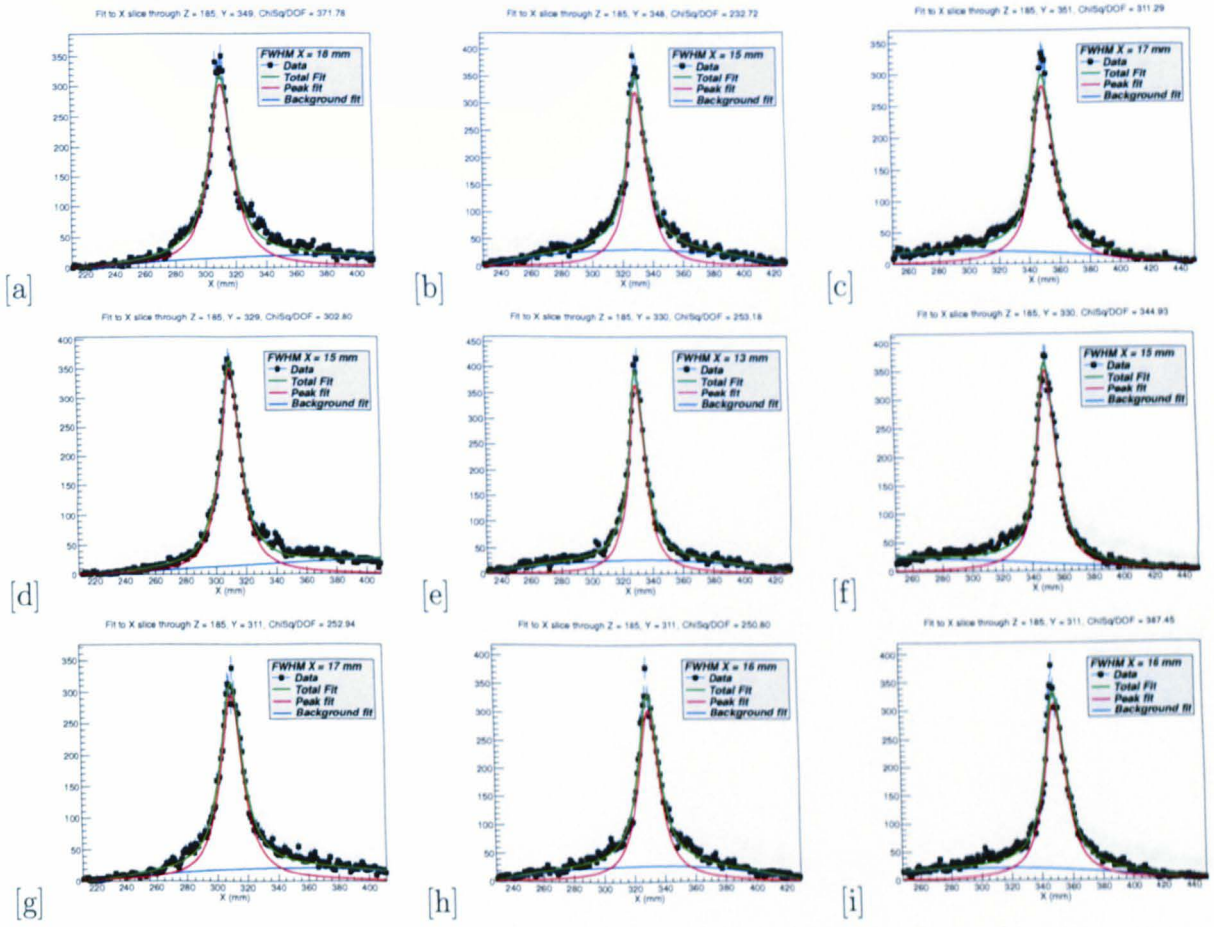

Figure 5.24: 0.662 MeV X projections. source positions are (X,Y) 10mm,50mm [a], 30mm,50mm [b], 50mm,50mm [c], 10mm,30mm [d], 30mm,30mm [e], 50mm,30mm [f], 10mm,10mm [g], 30mm,10mm [h] and 50mm,10mm [i].

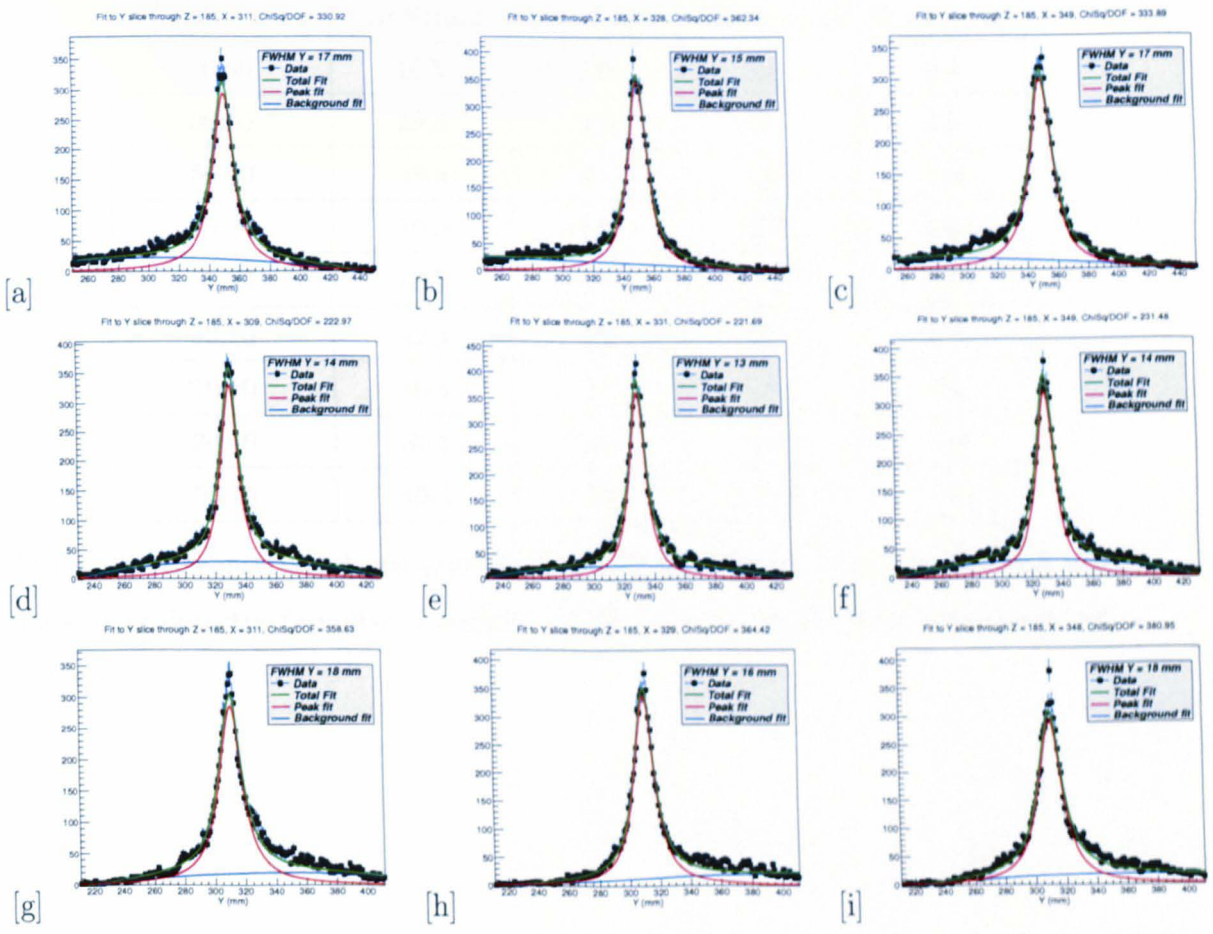

Figure 5.25: 0.662 MeV Y projections. source positions are (X,Y) 10mm,50mm [a], 30mm,50mm [b], 50mm,50mm [c], 10mm,30mm [d], 30mm,30mm [e], 50mm,30mm [f], 10mm,10mm [g], 30mm,10mm [h] and 50mm,10mm [i].

The reconstructed source positions are given below by Table 5.8. It can be seen that there isn't much deviation from the original source position. The reconstructed position deviations of a 0.662 MeV point source using GeGe over a range of different source positions is illustrated by Figure 5.26 and Figure 5.27.

X(mm),Y(mm)	Rec X(mm)	Error(mm)	Rec Y(mm)	Error(mm)
10,50	10.5	2.0	49.5	2.0
30,50	29.5	2.0	49.7	2.0
50,50	49.5	2.0	49.2	2.0
10,30	10.3	2.0	29.9	2.0
30,30	30.2	2.0	29.7	2.0
50,30	49.5	2.0	29.9	2.0
10,10	10.4	2.0	10.7	2.0
30,10	30.2	2.0	10.2	2.0
50,10	49.4	2.0	10.2	2.0

Table 5.8: Reconstructed positions for a 0.662 MeV point source positioned across the scatter detector face over a number of different locations. Detector separation = 100mm.

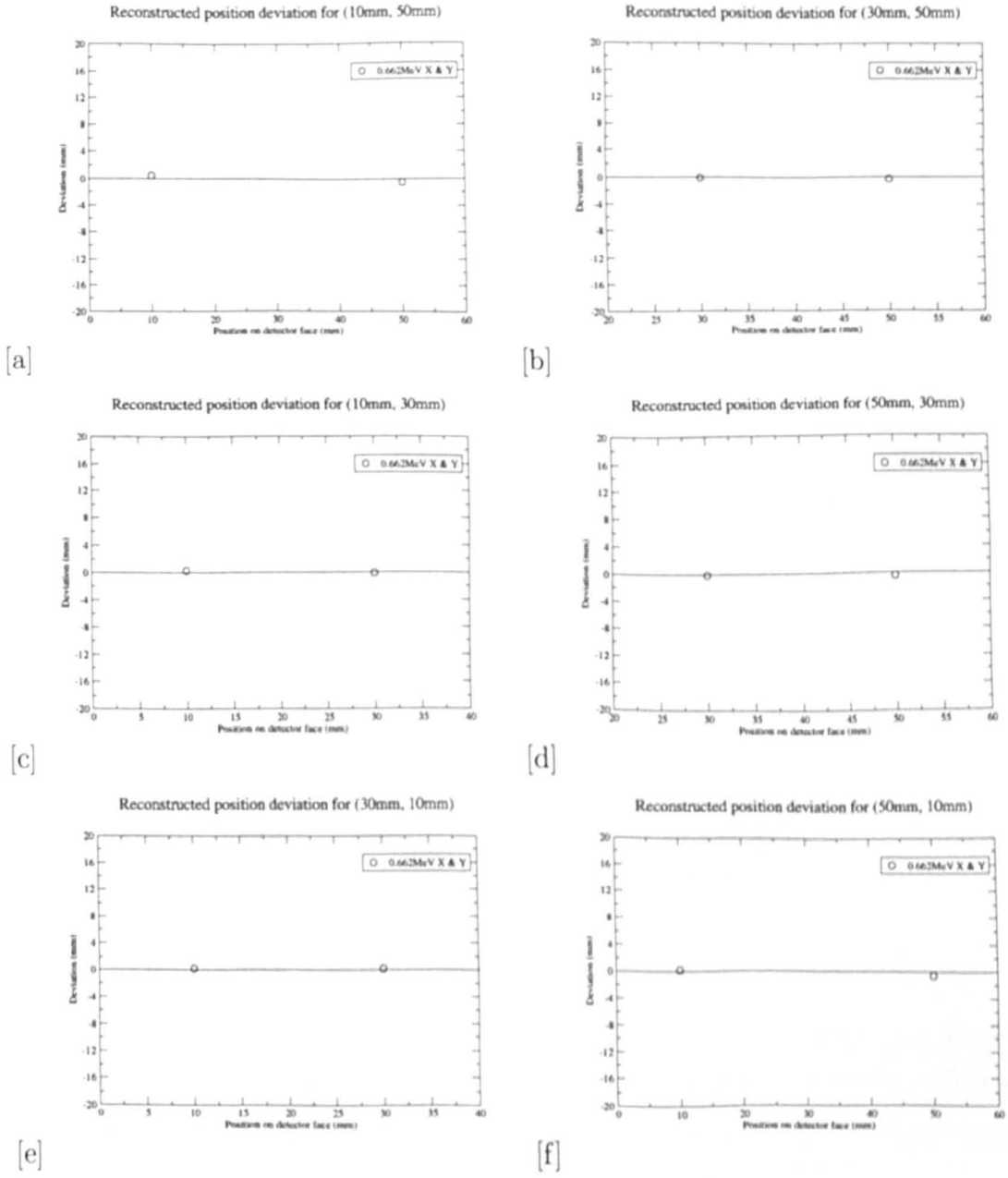

Figure 5.26: Reconstruction position deviations over a range of different 0.662 MeV source positions. They are 10mm,50mm [a], 30mm,50mm [b], 10mm,30mm [c], 50mm,30mm [d], 30mm,10mm [e], and 50mm,10mm [f].

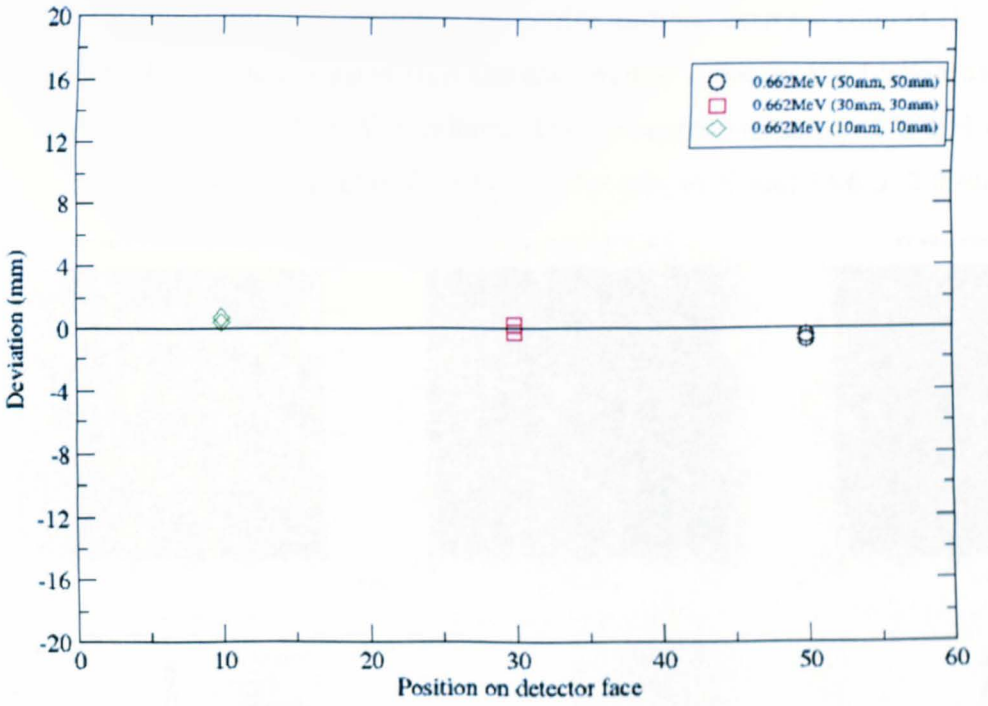

Figure 5.27: Reconstruction position deviations over a range of different 0.662MeV source positions. They are 10mm,10mm, 30mm,30mm and 50mm,50mm.

5.3.7 Assessing asymmetry

Section 5.3.6 discusses the asymmetry of the reconstructed Compton images and image FWHM as the 0.662 MeV point source is positioned away from the centre at X = Y = 30mm in a number of other positions closer to the edge of the scatter detector face. The reconstructed image FWHM values show a clear asymmetry compared to the image FWHM when the source is positioned at X = Y = 30mm. To check if the asymmetry is a feature only at the outer edges of the scatter detector face, the 0.662 MeV point source was positioned at an intermediate position between X = Y = 30mm and X = 10mm, Y = 50mm. The source was positioned at X = 20mm, Y =

40mm. The reconstructed images and the X and Y projections are given by Figure 5.28. Figure 5.28 shows that there is a small amount of asymmetry when the source has been positioned part way between the centre and the extreme edge of the scatter detector face. This would suggest that the asymmetry increases the further away the position of a source from X = Y = 30mm. The reconstructed image FWHM at X = 20mm and Y = 40mm is calculated as 14.1 ± 2.0 mm in X and 14.6 ± 2.0 mm.

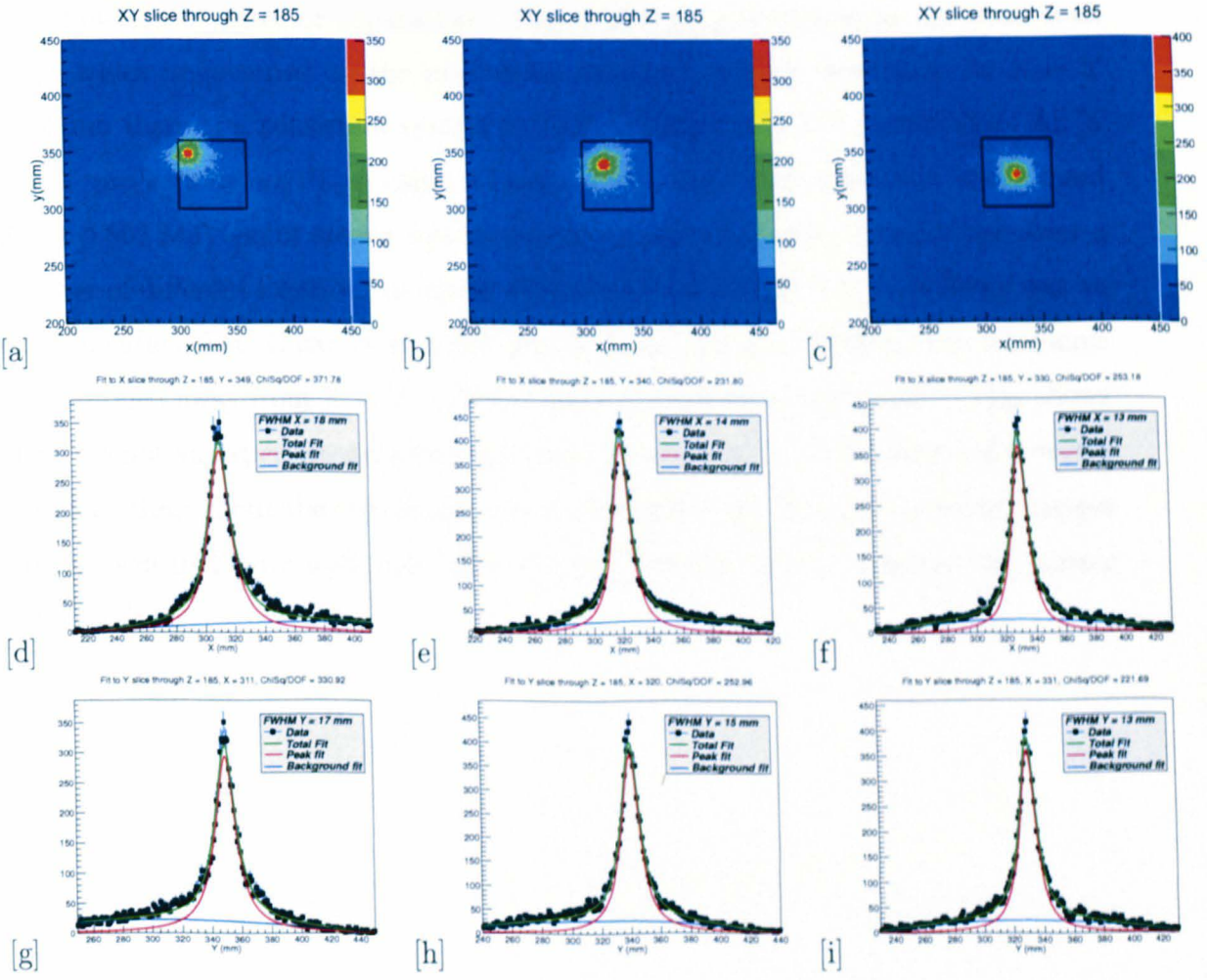

Figure 5.28: Reconstructed Compton images of a 0.662 MeV point source and their respective X and Y projections. The positions are X = 10mm, Y = 50mm [a],[d],[g], X = 20mm, Y = 40mm [b],[e],[h] and X = Y = 30mm [c],[f],[i].

5.4 Summary of lower energy simulated point source imaging

Simulated Compton images have been successfully reconstructed for 0.662 MeV and 1.332 MeV point sources at X = Y = 30mm for detector separations of 30mm, 50mm and 100mm. For both sets of simulations it is seen that the image FWHM improves as a function of detector separation. This is due to a reduction in the cone apex angle which is governed by the interaction positions in both detectors. At X = Y = 30mm there is a consistent symmetry in the images and X,Y projections. All X and Y projections are fitted using a Lorentzian peak fit and quadratic background fit. A 0.662 MeV point source was positioned across the scatter detector face over a number of different locations to assess whether the image and X,Y ssymmetry was an experimental effect. It can be seen in Figure 5.23 and Figure 5.28 that when the source is positioned away from X = Y = 30mm there is an obvious asymmetry. This shows that it is not an experimental effect and that it is governed by the source and detector positions throughout the experiments and the simulations. The reconstructed images can be seen in Figure 5.23 and Table 5.8 for all source positions across the scatter detector face.

Chapter 6

Intermediate energy GEANT4 Compton imaging

The 1:1 Compton effiency of both GeGe and GeCsI detector configurations as a function of detector separation, has been discussed in Chapter 5. The number of 1:1 Compton events for every 200 million primary gamma rays can be seen in Table 5.2 for GeGe and Table 5.3 for GeCsI. The GeCsI system is consistently more efficient than the GeGe system yet at higher energies and in particular with larger detector separations the number of 1:1 events is inherantly low in both systems. In chapter 3, Figure 3.2 shows that to reconstruct a good enough image then there should be as close as possible to 1000 1:1 Compton events. The number of 1:1 events yielded from the 200 million gamma ray simulations has been assessed and it was concluded that a lot of the simulations needed a lot more primary gamma rays to be able to generate enough 1:1 events to reconstruct any images. Most simulations were subject to 1billion primary gamma rays and the efficiency of the systems at intermediate energies produced enough 1:1 events for reconstruction. Simulations of 4.430MeV - 6.130MeV at the larger detector separations were run with 2billion primary gamma rays as the efficiency of 1:1 events is so low.

Geant4 has an inbuilt limit of the number of events that a simulation can run for at any time. This number is just above 2billion events. That being said, a number

of the simulations at larger detector separations yielded less than 1000 1:1 Compton events. This chapter discusses the intermediate energy range from 1.640 MeV to 4.430 MeV and the Compton imaging results as a function of detector separation. To have a direct comparison between the performance of the GeGe system with the GeCsI system then the same number of events must be reconstructed in both. The number of events reconstructed for each energy at each detector separation is given in Table 6.1

Energy (MeV)	Sep(mm)	No of events
1.640	30	4000
	50	2400
	100	1700
2.310	30	2200
	50	1250
	100	1090
4.430	30	1650
	50	1250
	100	902
5.110	30	1500
	50	1500
	100	603
6.130	30	1000
	50	820
	100	281

Table 6.1: The number of events reconstructed for both detector configurations for all energies at each detector separation.

6.1 1.640 MeV - 4.430 MeV Compton imaging

Every point source with its own independant energy was positioned at X = Y = 30mm across the scatter detector face. 45mm away in Z for both GeGe and GeCsI over 30mm, 50mm and 100mm detector separations. All energy and position information was input into the reconstruction algorithm and an ellipse at a distance of Z = 45mm from the scatter detector face is created. Images have been reconstructed projecting the number of events for each energy and each separation listed in the Table 6.1. The image FWHM (mm) in the X and Y projections has been calculated for every image for Z = 45mm. Every image has been translated 30mm in X and 300mm in Y and the detector position is always defined by the black box. The final reconstructed source position in X and Y is calculated for both GeGe and GeCsI and given by Table 6.4 and Table 6.5 respectively. For the intermediate energies of 1.640 MeV - 4.430 MeV, the image FWHM for the X and Y projections is given by Table 6.2 for GeGe and Table 6.3 for GeCsI. The reconstructed image FWHM as a function detector separation for 1.640 MeV can be visualised in Figure 6.4. The image FWHM of the GeGe system for 1.640 MeV improves from 19.6 ± 2.0 mm and 19.6 ± 2.0 mm at 30mm to 12.5 ± 2.0 mm and 13.8 ± 2.0 mm at 100mm. The image FWHM from the GeCsI system for 1.640 MeV improves from 26.4mm±0.9mm and 25.0mm±0.8mm at 30mm to 12.5mm±0.5mm and 16.1mm±0.6mm at 100mm. For the GeGe system at 2.310 MeV the image FWHM improves from 17.5 ± 2.0 mm and 21.4 ± 2.0 mm at 30mm to 13.0 ± 2.0 and 12.4 ± 2.0mm at 100mm. For the GeCsI system at 2.310 MeV the image FWHM improves from 21.9 ± 2.0 mm and 23.0 ± 2.0mm at 30mm to 11.1 ± 2.0 mm and 12.5 ± 2.0 mm at 100mm. For the GeGe system at 4.430 MeV the image FWHM improves from 15.5 ± 2.0 mm and 17.7 ± 2.0 mm at 30mm to 10.7 ± 2.0 mm and 12.8 ± 2.0 mm at 100mm. For the GeCsI system the image FWHM improves from 19.3 ± 2.0 mm and 20.9 ± 2.0 mm at 30mm detector separation to 11.1 ± 2.0 mm and 11.0 ± 2.0 mm at 100mm detector separation.

All reconstructed images, along with their respective X and Y projections as a function of detector separation are given by the following Figures:

- Images and X Y projections of 1.640 MeV = Figure 6.1, Figure 6.2, Figure 6.3
- Image FWHM (mm) of 1.640 MeV = Figure 6.4
- Images and X Y projections of 2.310 MeV = Figure 6.5, Figure 6.6, Figure 6.7
- Image FWHM (mm) of 2.310 MeV = Figure 6.8
- Images and X Y projections of 4.430 MeV = Figure 6.9, Figure 6.10, Figure 6.11
- Image FWHM (mm) of 4.430 MeV = Figure 6.12

The reconstructed source positions for GeGe and GeCsI are given by Table 6.4 and Table 6.5 respectively. It can be seen there is some reconstructed position deviation from the original position of X = Y = 30mm. The reconstructed position deviation for both detector configurations as a function of detector separation is given by Figure 6.13.

Energy (MeV)	Sep(mm)	FWHM X(mm)	Error(mm)	FWHM Y(mm)	Error(mm)
1.640	30	19.6	2.0	19.6	2.0
	50	20.3	2.0	17.8	2.0
	100	12.5	2.0	13.8	2.0
2.310	30	17.5	2.0	21.4	2.0
	50	13.9	2.0	13.4	2.0
	100	13.0	2.0	12.4	2.0
4.430	30	15.5	2.0	17.7	2.0
	50	17.1	2.0	15.9	2.0
	100	10.7	2.0	12.8	2.0

Table 6.2: GeGe Reconstructed image FWHM(mm) for 1.640 MeV - 4.430 MeV point sources positioned at the centre (X = Y = 30mm) of the scatter detector face at differing detector separations.

Energy (MeV)	Sep(mm)	FWHM X(mm)	Error(mm)	FWHM Y(mm)	Error(mm)
1.640	30	19.5	2.0	19.3	2.0
	50	14.3	2.0	14.5	2.0
	100	11.2	2.0	13.1	2.0
2.310	30	21.9	2.0	23.0	2.0
	50	16.6	2.0	14.9	2.0
	100	11.1	2.0	12.5	2.0
4.430	30	19.3	2.0	20.9	2.0
	50	13.6	2.0	15.4	2.0
	100	11.1	2.0	11.0	2.0

Table 6.3: GeCsI Reconstructed image FWHM(mm) for 1.640 MeV - 4.430 MeV point sources positioned at the centre (X = Y = 30mm) of the scatter detector face at differing detector separations.

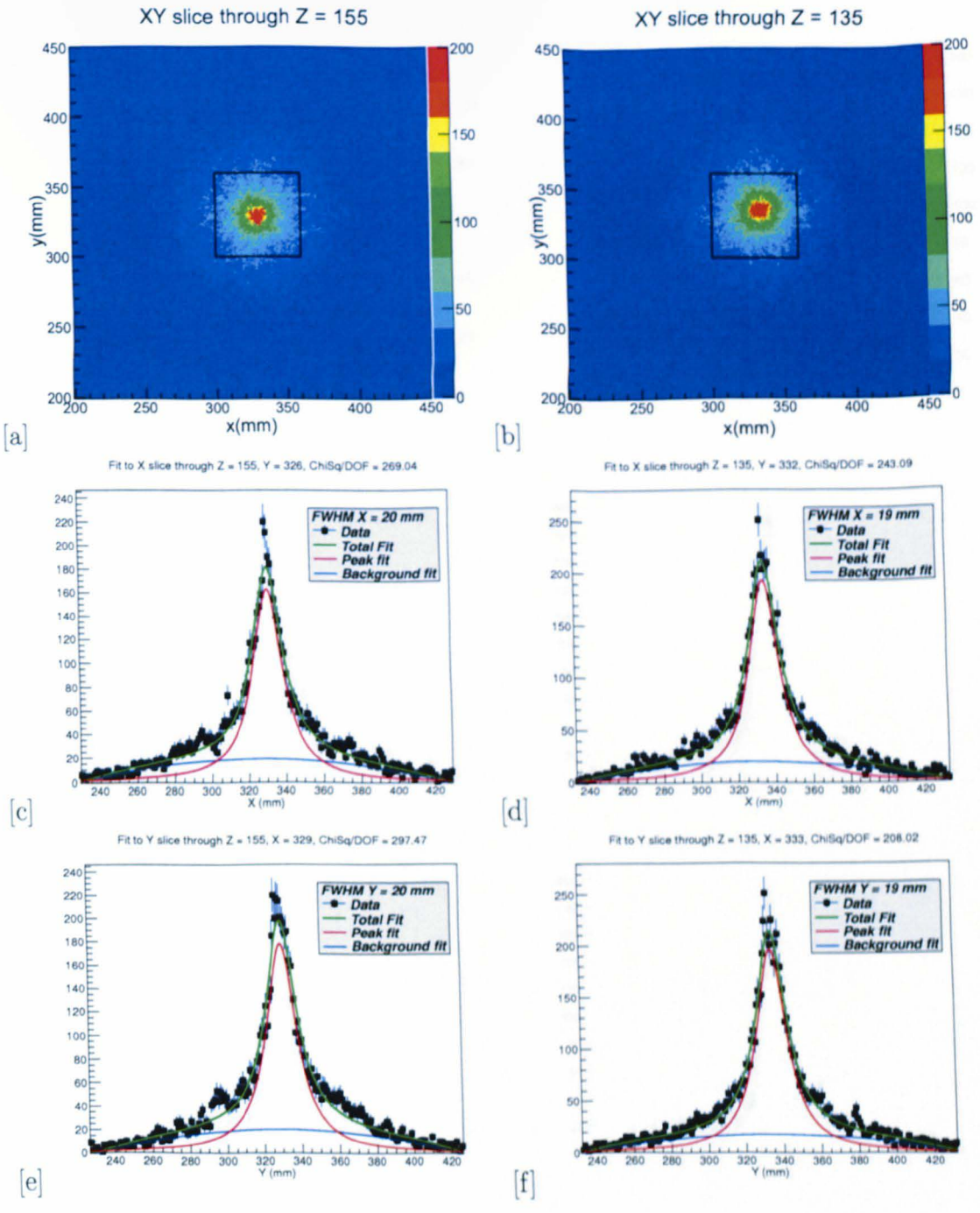

Figure 6.1: Simulated images and X,Y projections of a 1.640 MeV point source positioned 45mm from the scatter detector with X = Y = 30mm with a detector separation of 30mm. GeGe is [a],[c],[e]. GeCsI is [b],[d],[f].

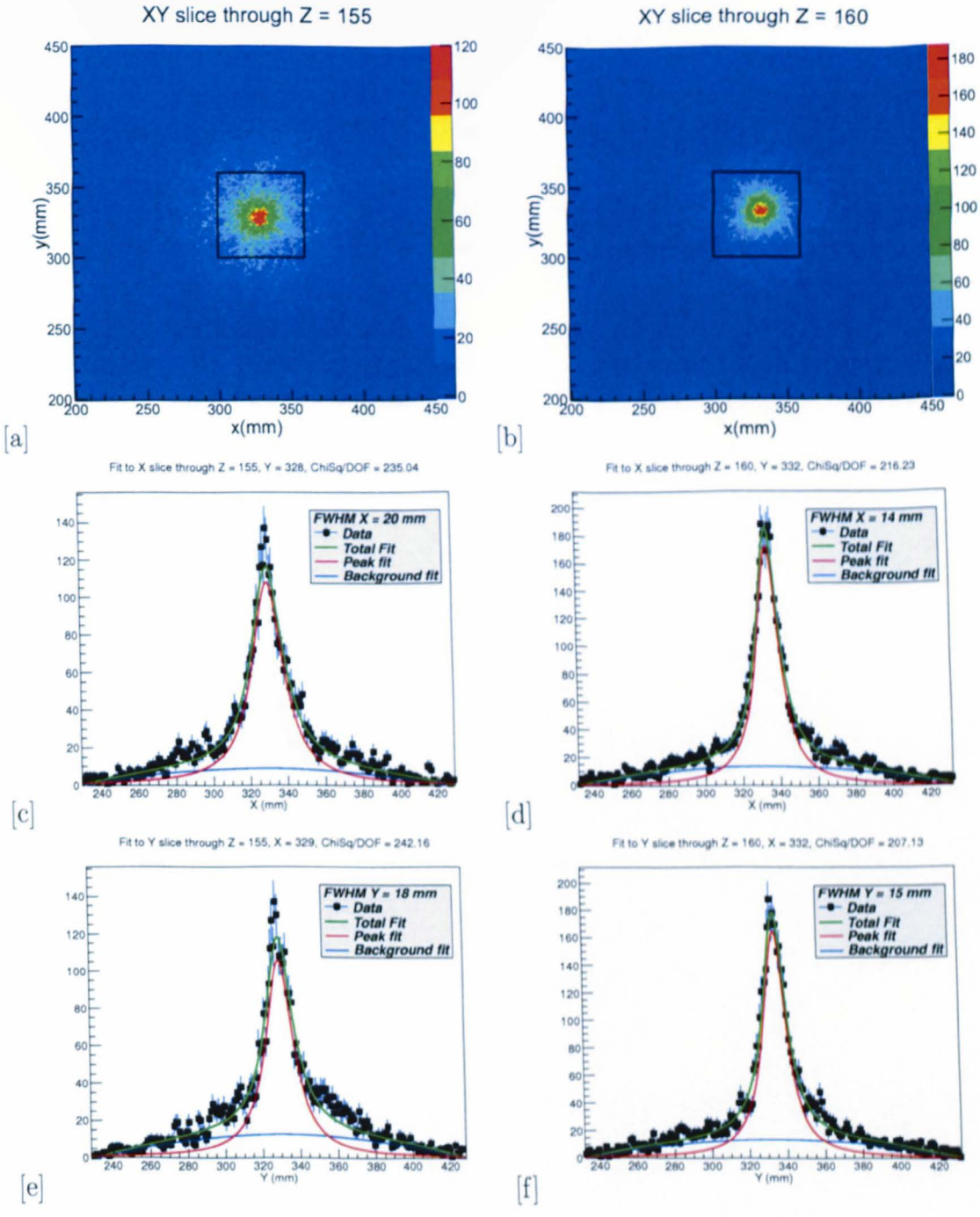

Figure 6.2: Simulated images and X,Y projections of a 1.640 MeV point source positioned 45mm from the scatter detector with X = Y = 30mm with a detector separation of 50mm. GeGe is [a],[c],[e]. GeCsI is [b],[d],[f].

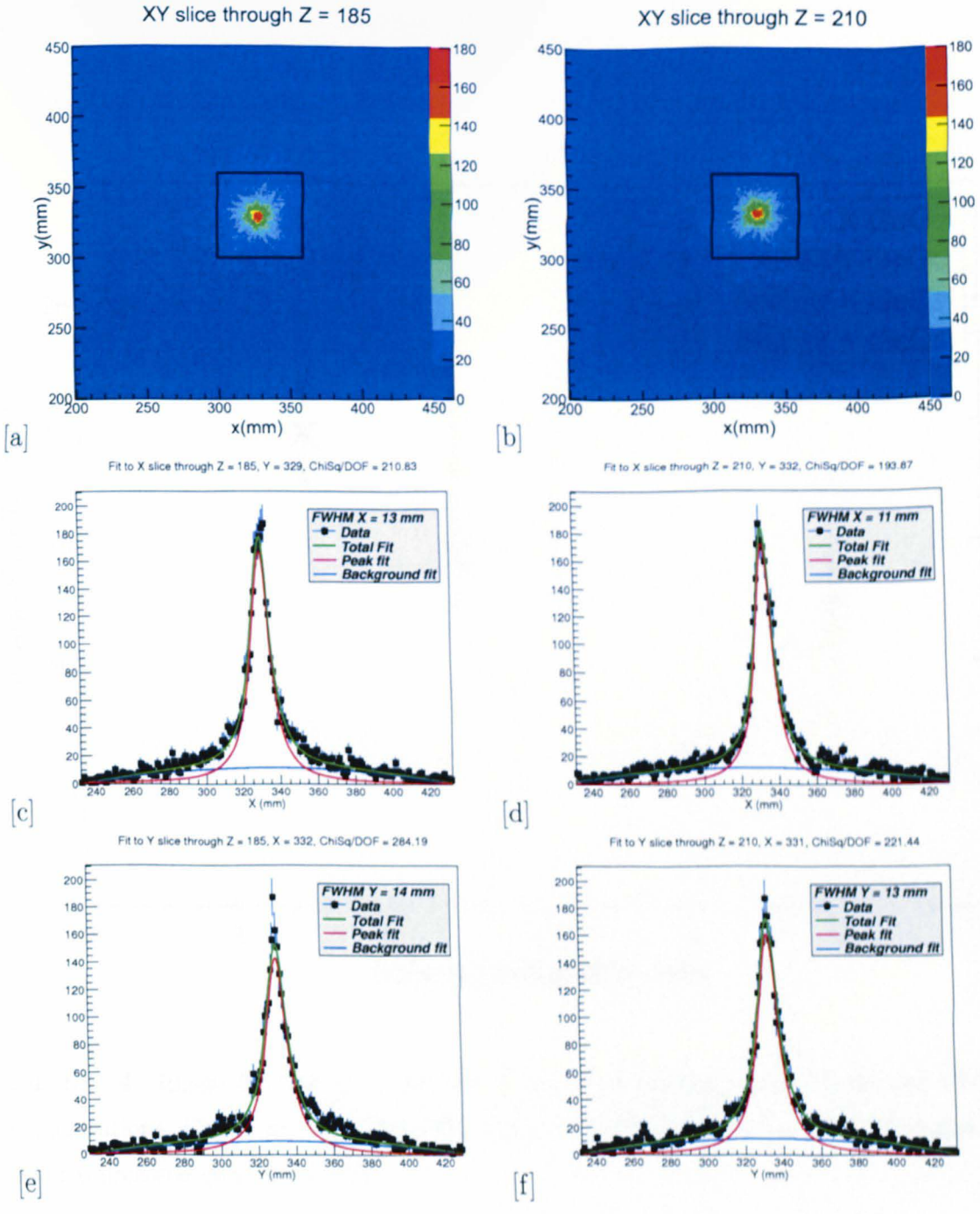

Figure 6.3: Simulated images and X,Y projections of a 1.640 MeV point source positioned 45mm from the scatter detector with X = Y = 30mm with a detector separation of 100mm. GeGe is [a],[c],[e]. GeCsI is [b],[d],[f].

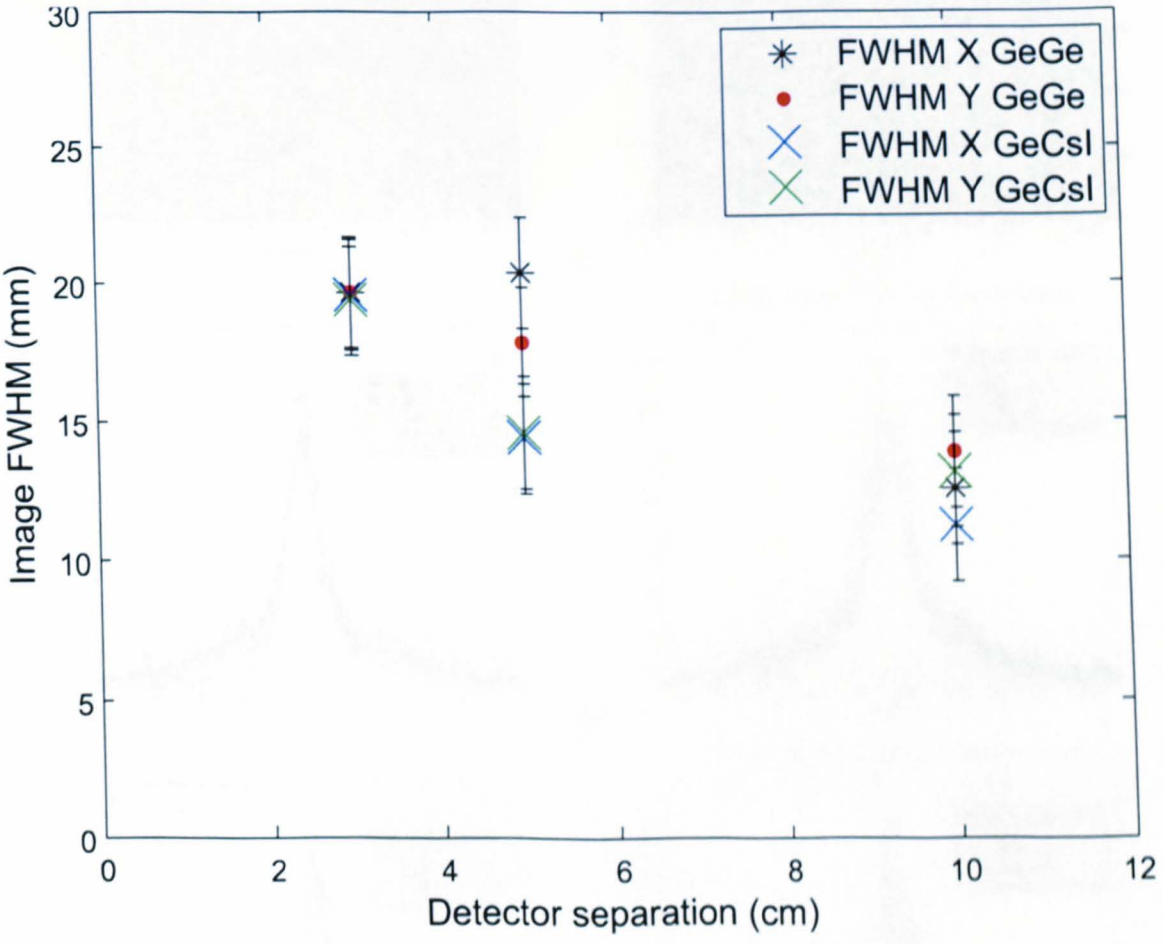

Figure 6.4: Image FWHM (mm) for the X and Y projections of the GeGe and GeCsI configurations. Given over the 30mm, 50mm and 100mm detector separations. The gamma point source energy is 1.640 MeV

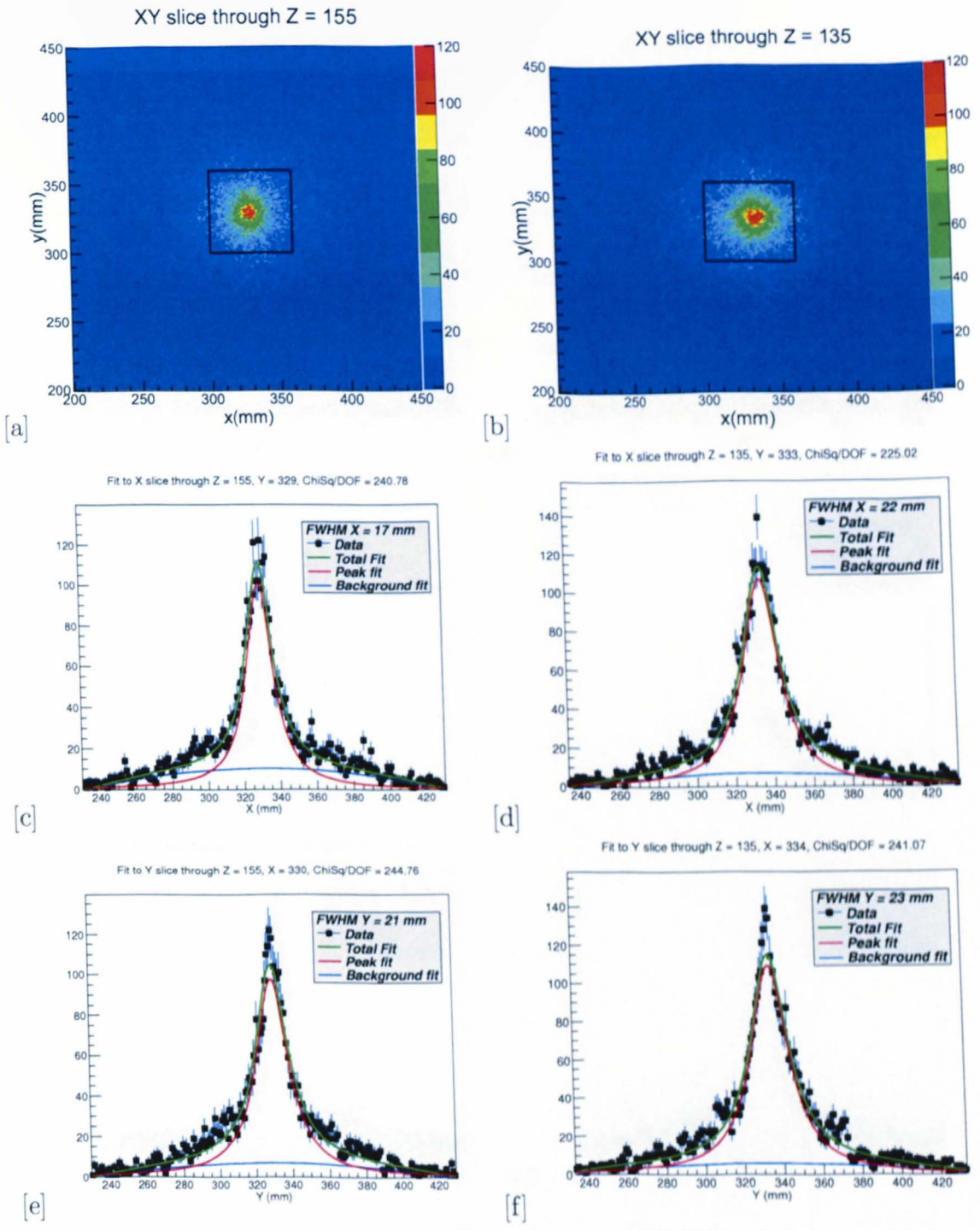

Figure 6.5: Simulated images and X,Y projections of a 2.310 MeV point source positioned 45mm from the scatter detector with X = Y = 330mm with a detector separation of 30mm. GeGe is [a],[c],[e]. GeCsI is [b],[d],[f].

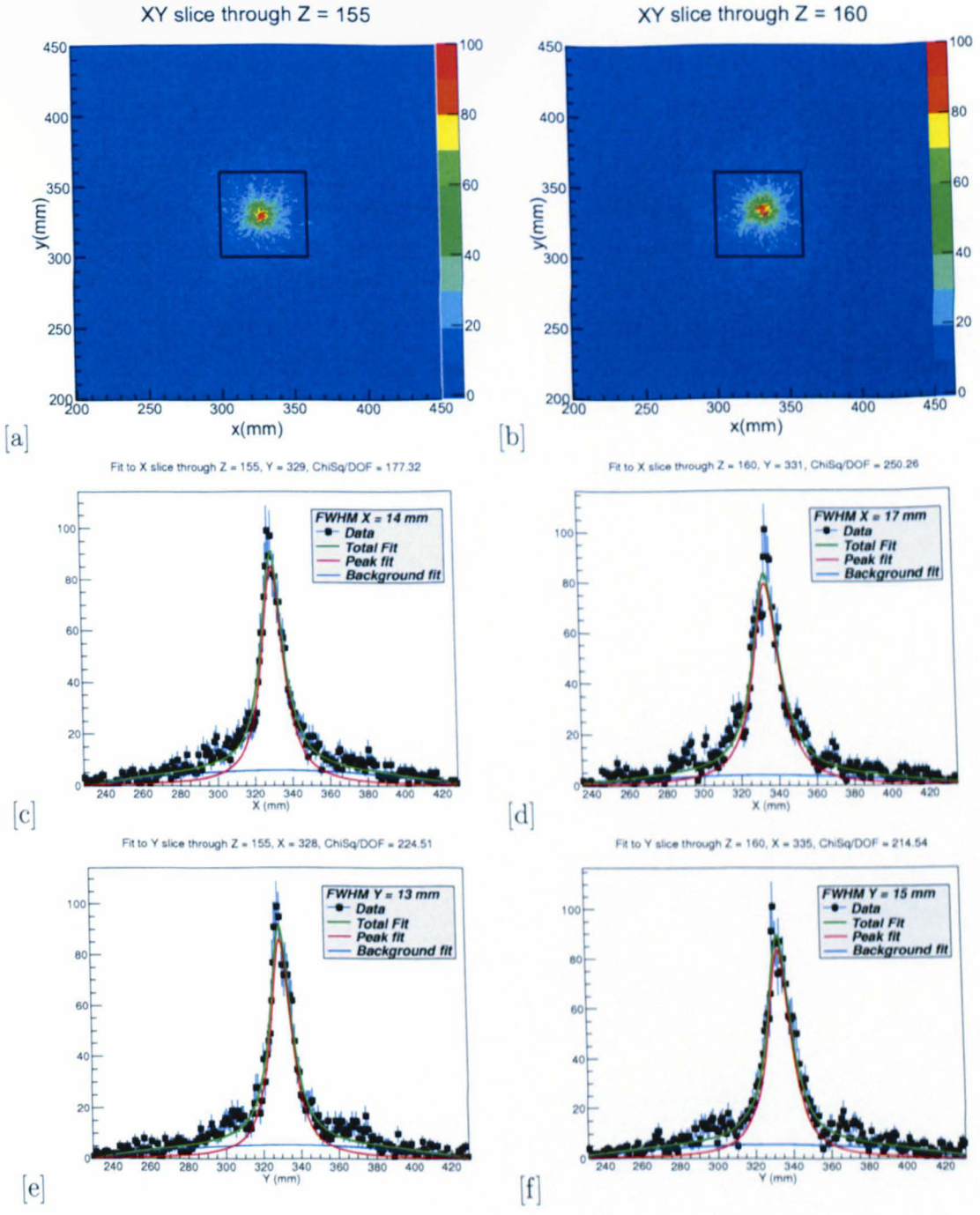

Figure 6.6: Simulated images and X,Y projections of a 2.310 MeV point source positioned 45mm from the scatter detector with X = Y = 330mm with a detector separation of 50mm. GeGe is [a],[c],[e]. GeCsI is [b],[d],[f].

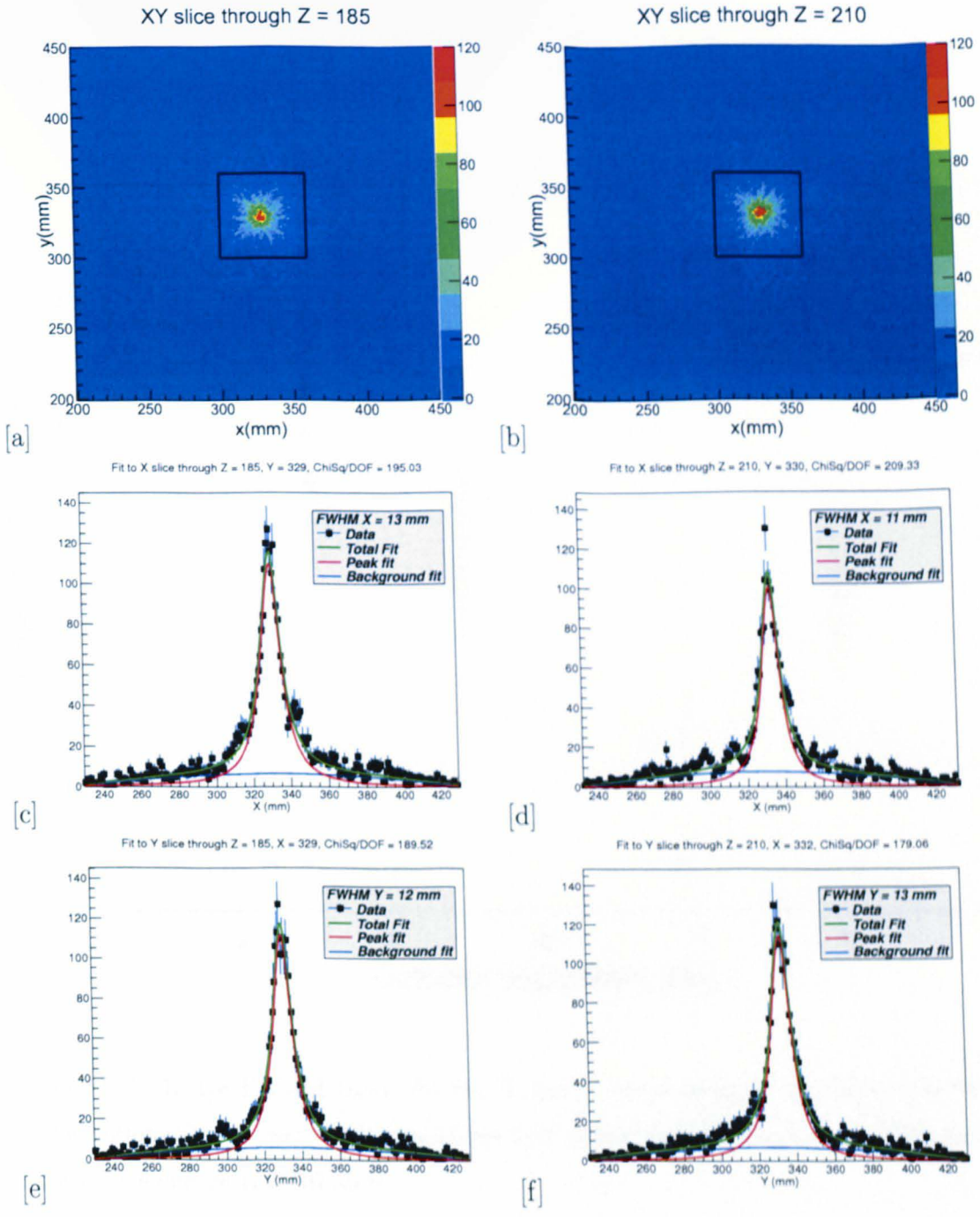

Figure 6.7: Simulated images and X,Y projections of a 2.310 MeV point source positioned 45mm from the scatter detector with X = Y = 330mm with a detector separation of 100mm. GeGe is [a],[c],[e]. GeCsI is [b],[d],[f].

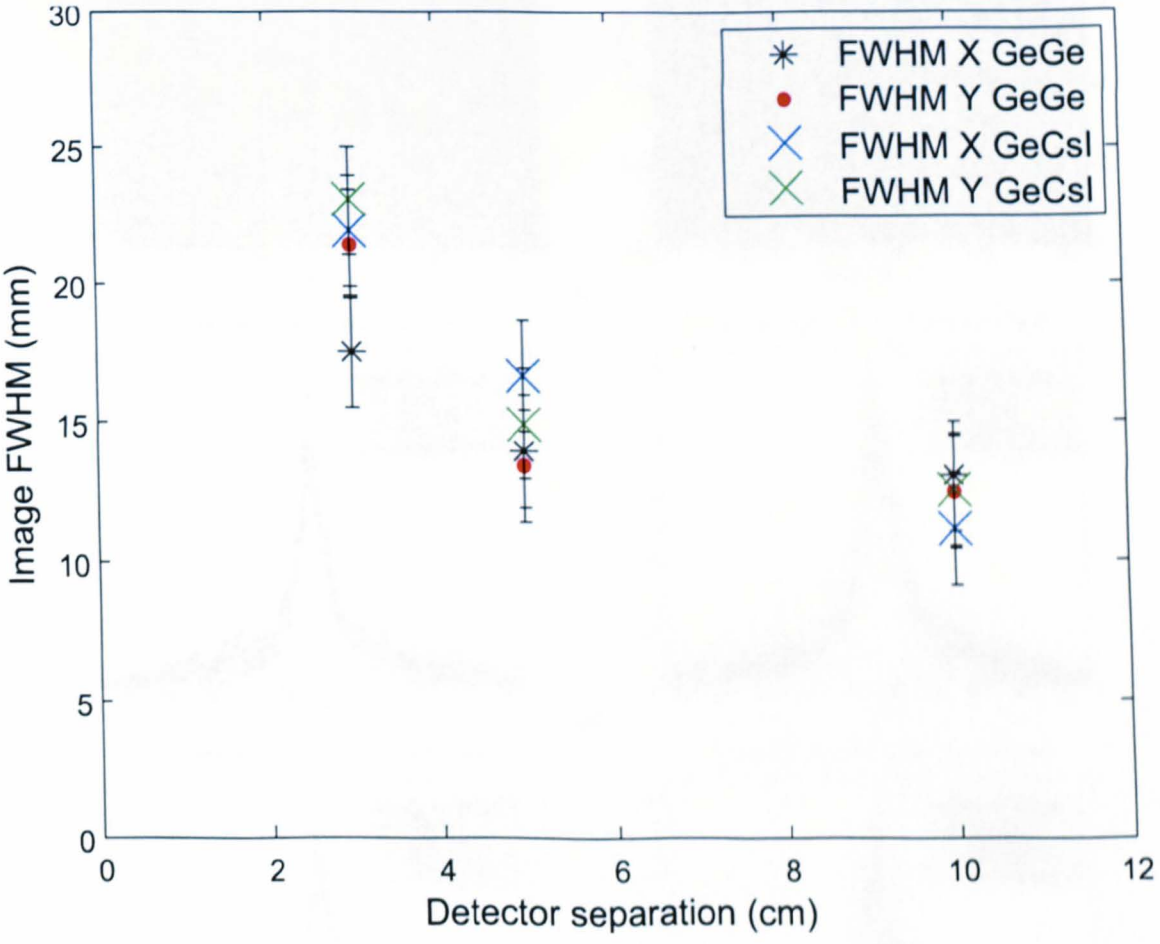

Figure 6.8: Image FWHM (mm) for the X and Y projections of the GeGe and GeCsI configurations. Given over the 30mm, 50mm and 100mm detector separations. The gamma point source energy is 2.310 MeV

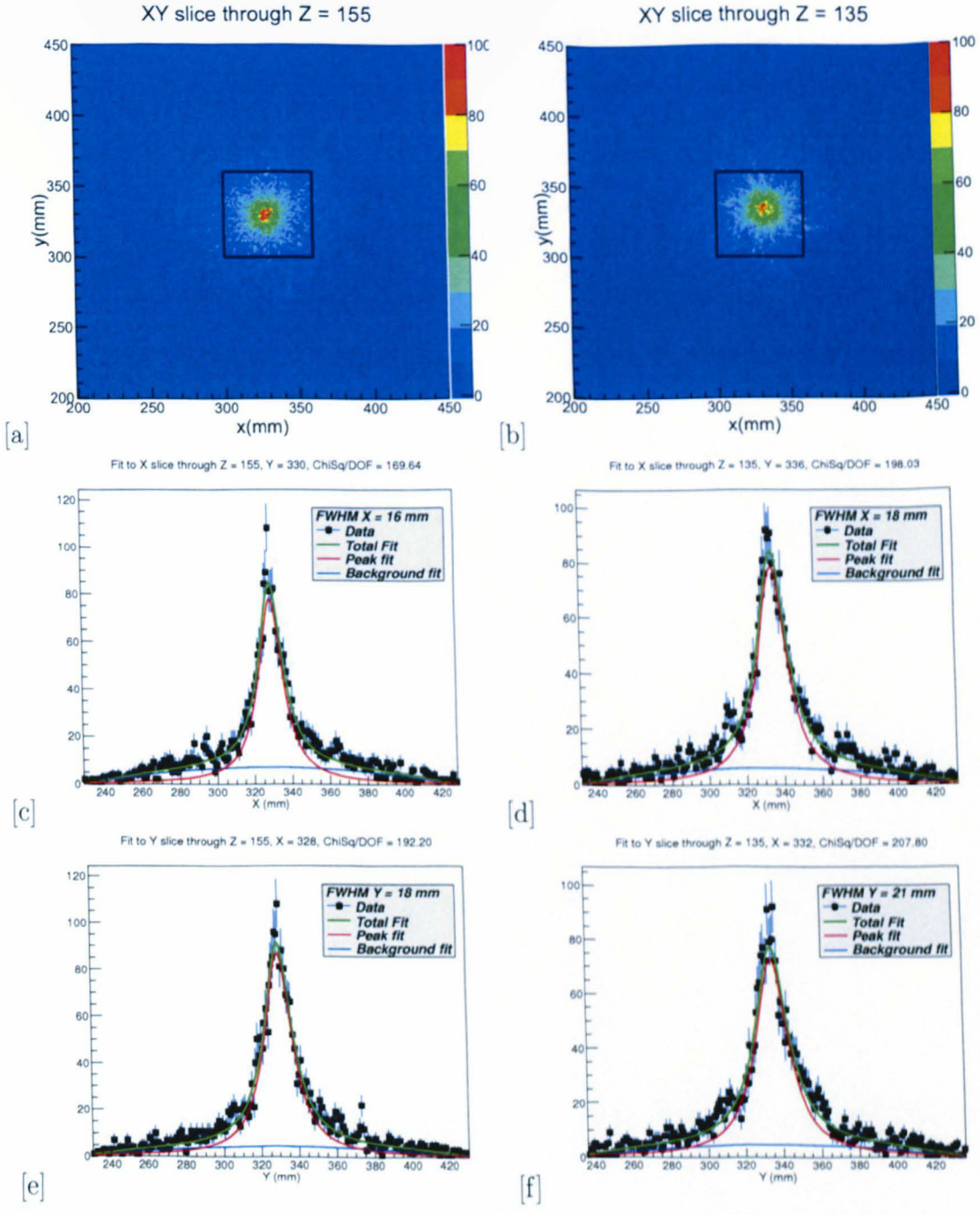

Figure 6.9: Simulated images and X,Y projections of a 4.430 MeV point source positioned 45mm from the scatter detector with X = Y = 330mm with a detector separation of 30mm. GeGe is [a],[c],[e]. GeCsI is [b],[d],[f].

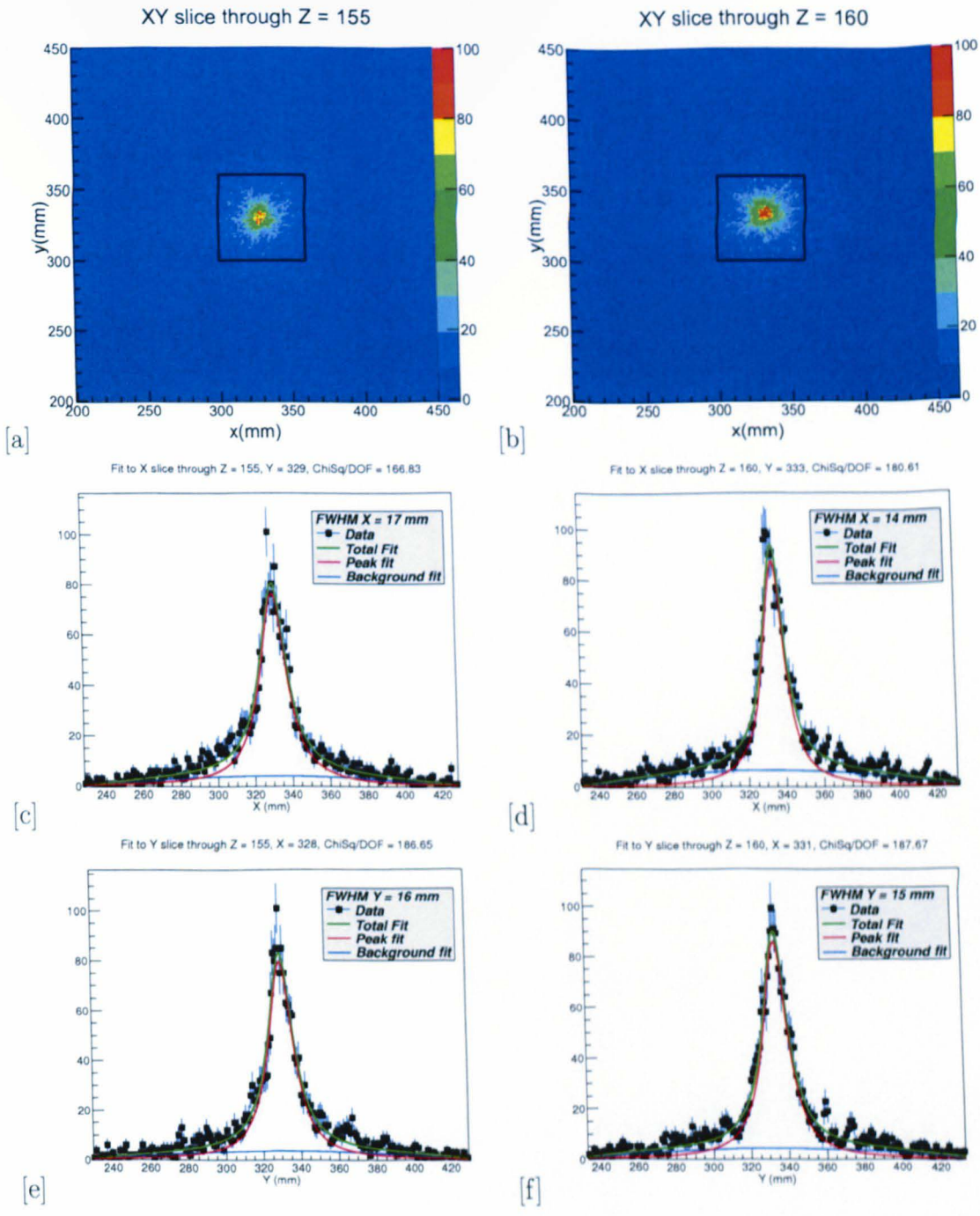

Figure 6.10: Simulated images and X,Y projections of a 4.430 MeV point source positioned 45mm from the scatter detector with X = Y = 330mm with a detector separation of 50mm. GeGe is [a],[c],[e]. GeCsI is [b],[d],[f].

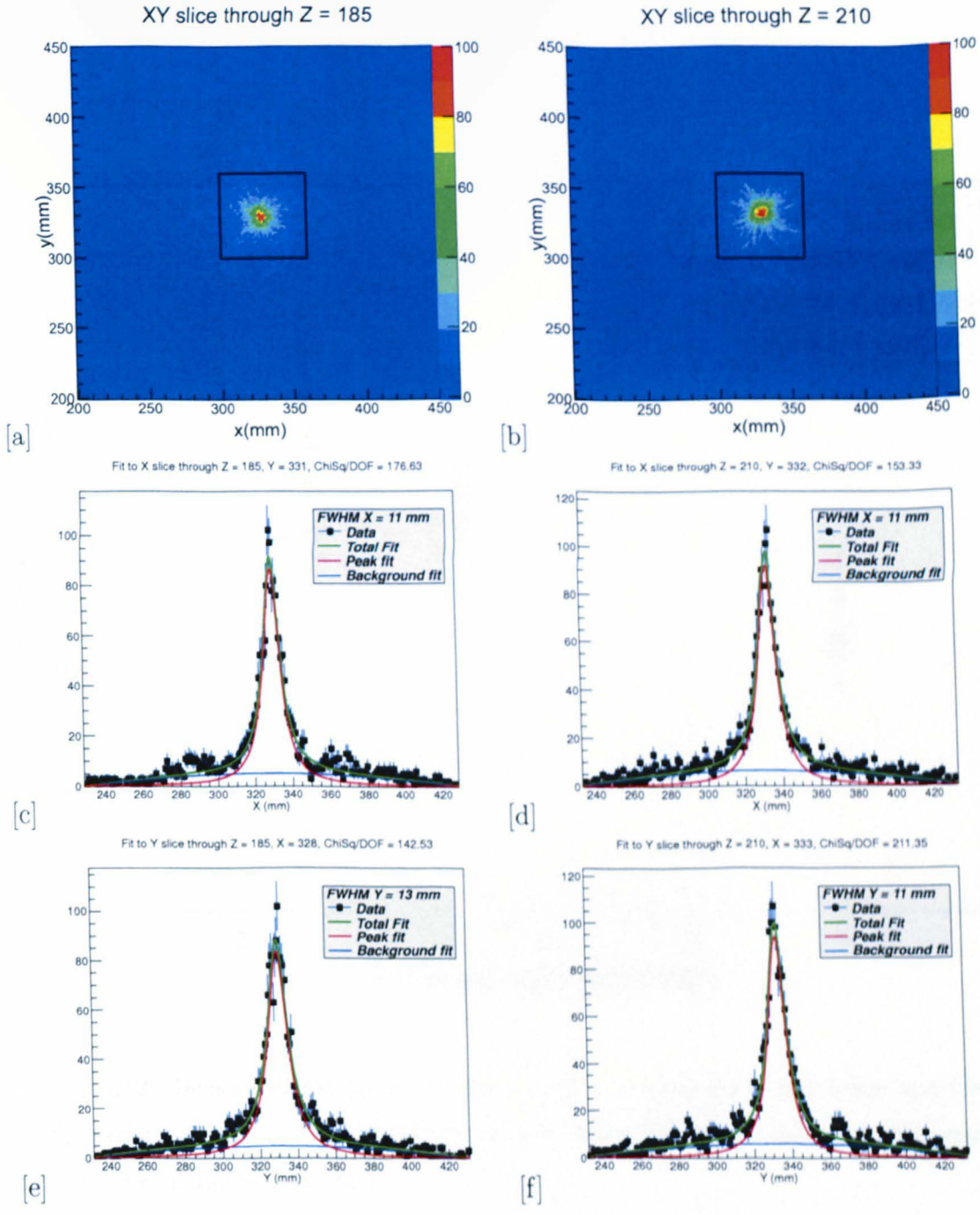

Figure 6.11: Simulated images and X,Y projections of a 4.430 MeV point source positioned 45mm from the scatter detector with X = Y = 30mm with a detector separation of 100mm. GeGe is [a],[c],[e]. GeCsI is [b],[d],[f].

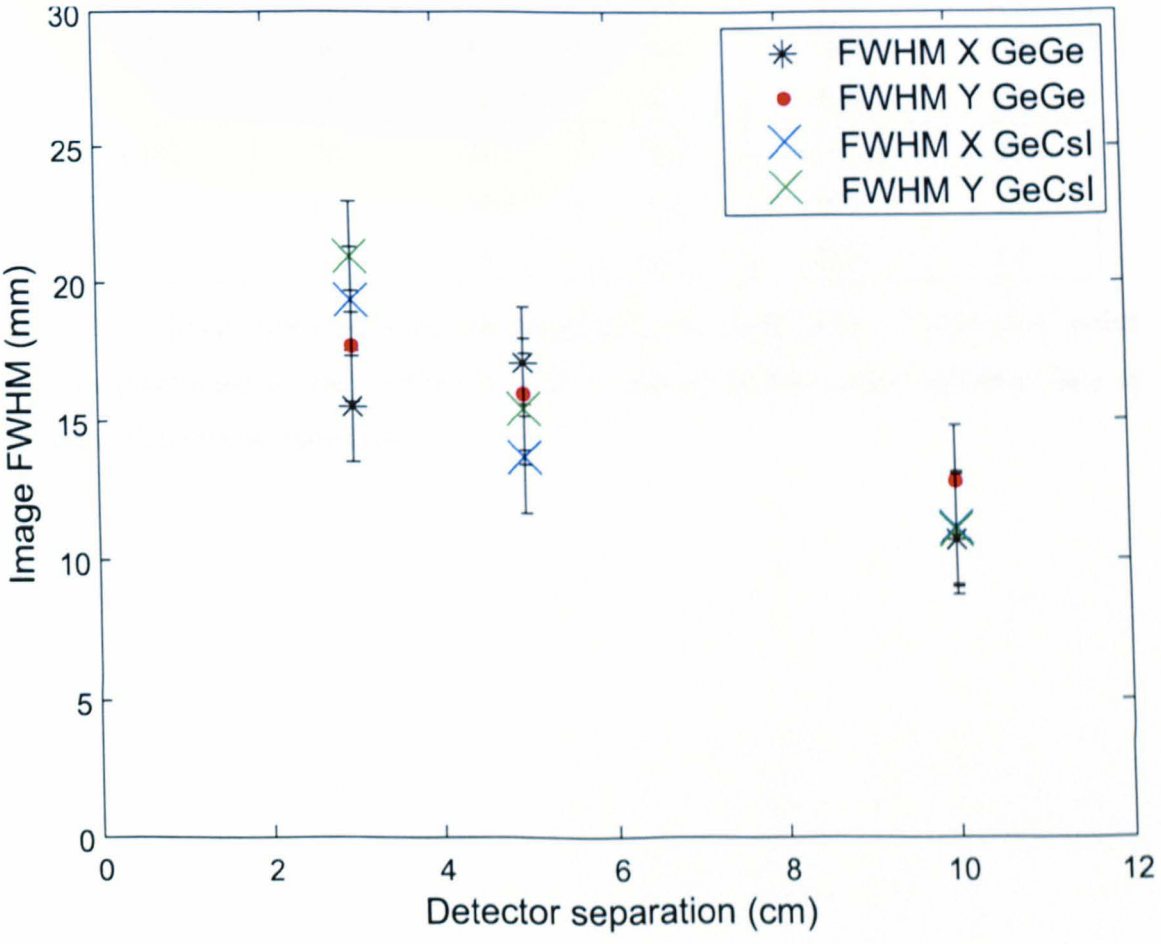

Figure 6.12: Image FWHM (mm) for the X and Y projections of the GeGe and GeCsI configurations. Given over the 30mm, 50mm and 100mm detector separations. The gamma point source energy is 4.430 MeV

Energy (MeV)	Sep(mm)	Rec X(mm)	Error(mm)	Rec Y(mm)	Error(mm)
1.640	30	30.2	2.0	29.7	2.0
	50	30.3	2.0	29.6	2.0
	100	29.6	2.0	30.03	2.0
2.310	30	29.1	2.0	29.4	2.0
	50	30.4	2.0	30.2	2.0
	100	29.9	2.0	30.6	2.0
4.430	30	29.5	2.0	29.8	2.0
	50	30.6	2.0	30.1	2.0
	100	30.1	2.0	29.6	2.0

Table 6.4: GeGe Reconstructed positions(mm) for 1.640 MeV - 4.430 MeV point sources positioned at the centre (X = Y = 30mm) of the scatter detector face at differing detector separations.

Energy (MeV)	Sep(mm)	Rec X(mm)	Error(mm)	Rec Y(mm)	Error(mm)
1.640	30	34.3	2.0	34.3	2.0
	50	34.1	2.0	34.1	2.0
	100	32.7	2.0	32.7	2.0
2.310	30	33.8	2.0	33.7	2.0
	50	34.3	2.0	33.3	2.0
	100	33.2	2.0	32.6	2.0
4.430	30	34.3	2.0	34.7	2.0
	50	34.4	2.0	43.0	2.0
	100	32.1	2.0	33.0	2.0

Table 6.5: GeCsI Reconstructed positions(mm) for 1.640 MeV - 4.430 MeV point sources positioned at the centre (X = Y = 30mm) of the scatter detector face at differing detector separations.

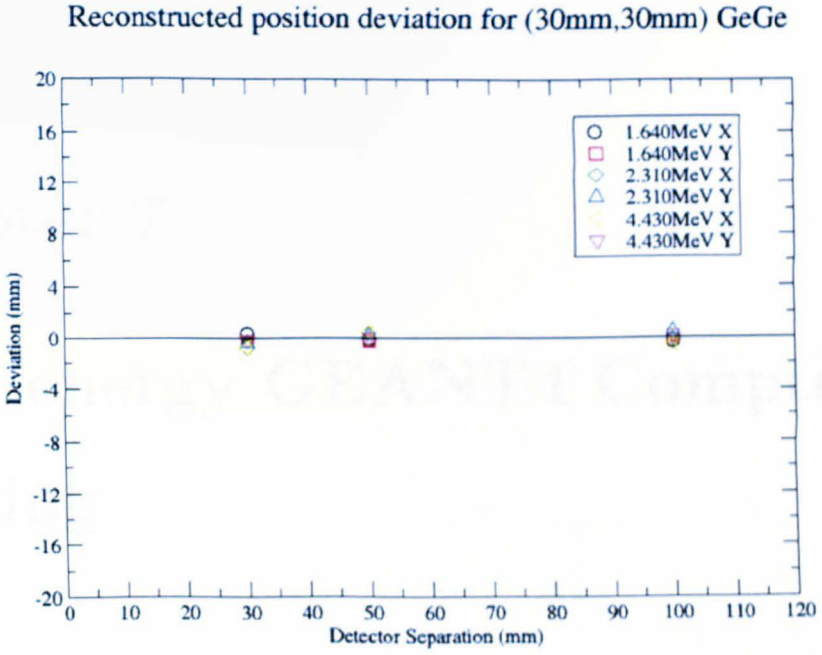

[a]

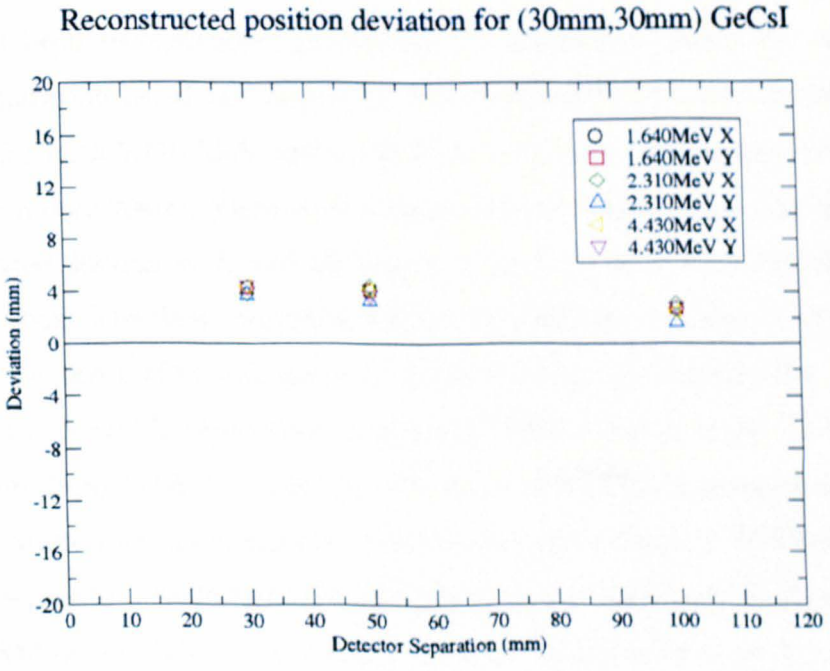

[b]

Figure 6.13: Reconstructed position deviation as a function of detector separation for 1.640 MeV to 4.430 MeV for GeGe [a] and GeCsI [b].

Chapter 7

High energy GEANT4 Compton imaging

7.1 5.110 MeV - 6.130 MeV Compton imaging

Images have been reconstructed projecting the number of events for each energy and each separation listed in Chapter 6. The image FWHM (mm) in the X and Y projections for both 5.110 MeV and 6.130 MeV have been calculated for every image for Z = 45mm over 30mm, 50mm and 100mm detector separations. Every image has been translated 300mm in X and 300mm in Y and the detector position is defined by the black box. The final reconstructed source positions in X and Y are calculated for both GeGe and GeCsI and given by Table 7.3 and 7.4 respectively. The image FWHM for the X and Y projections is given by Table 7.1 and Table 7.2 respectively. It can be seen from Table 7.1 that agin the image FWHM improves as a function of detector separation for both energies. The reconstructed image FWHM as a function of detector separation for both GeGe and GeCsI can be visualised in Figure 7.4. The image FWHM of the GeGe system for 5.110 MeV improves from 18.3 ± 2.0 mm and 18.1 ± 2.0 mm at 30mm to 10.6 ± 2.0 mm and 11.3 ± 2.0 mm at 100mm. The image FWHM from the GeCsI system for 5.110 MeV improves from 20.5 ± 2.0 mm and 17.9 ± 2.0 mm at 30mm to 11.2 ± 2.0 mm and 14.4 ± 2.0 mm at 100mm. For the GeGe

system at 6.130 MeV the image FWHM improves from 19.2 ± 2.0 mm and 18.2 ± 2.0 mm at 30mm to 8.4 ± 2.0 and 11.0 ± 2.0mm at 100mm. For the GeCsI system at 6.130 MeV the image FWHM improves from 28.8 ± 2.0 mm and 19.9 ± 2.0mm at 30mm to 13.4 ± 2.0 mm and 12.1 ± 2.0 mm at 100mm.

All reconstructed images, along with their respective X and Y projections as a function of detector separation are given by the following Figures:

- Images and X Y projections of 5.110 MeV = Figure 7.1, Figure 7.2, Figure 7.3
- Image FWHM (mm) of 5.110 MeV = Figure 7.4
- Images and X Y projections of 6.130 MeV = Figure 7.5, Figure 7.6, Figure 7.7
- Image FWHM (mm) of 6.130 MeV = Figure 7.8

The reconstructed source positions for GeGe and GeCsI are given by Table 7.3 and Table 7.4 respectively. It can be seen as with the lower energy simulations that there is some small reconstructed position deviation from the original position of X = Y = 30mm. The reconstruction position deviation for 5.110 MeV and 6.130 MeV is given by Figure 7.8.

Energy (MeV)	Sep(mm)	FWHM X(mm)	Error(mm)	FWHM Y(mm)	Error(mm)
5.110	30	18.3	2.0	18.1	2.0
	50	15.9	2.0	12.8	2.0
	100	10.6	2.0	11.3	2.0
6.130	30	19.2	2.0	18.2	2.0
	50	14.5	2.0	14.7	2.0
	100	8.4	2.0	11.0	2.0

Table 7.1: GeGe Reconstructed image FWHM(mm) for 5.110MeV - 6.130MeV point sources positioned at the centre (X = Y = 30mm) of the scatter detector face at differing detector separations.

Energy (MeV)	Sep(mm)	FWHM X(mm)	Error(mm)	FWHM Y(mm)	Error(mm)
5.110	30	20.5	2.0	17.9	2.0
	50	17.5	2.0	16.8	2.0
	100	11.2	2.0	14.4	2.0
6.130	30	28.8	2.0	19.9	2.0
	50	12.6	2.0	18.9	2.0
	100	13.4	2.0	12.1	2.0

Table 7.2: GeCsI Reconstructed image FWHM(mm) for 5.110 MeV - 6.130 MeV point sources positioned at the centre (X = Y = 30mm) of the scatter detector face at differing detector separations.

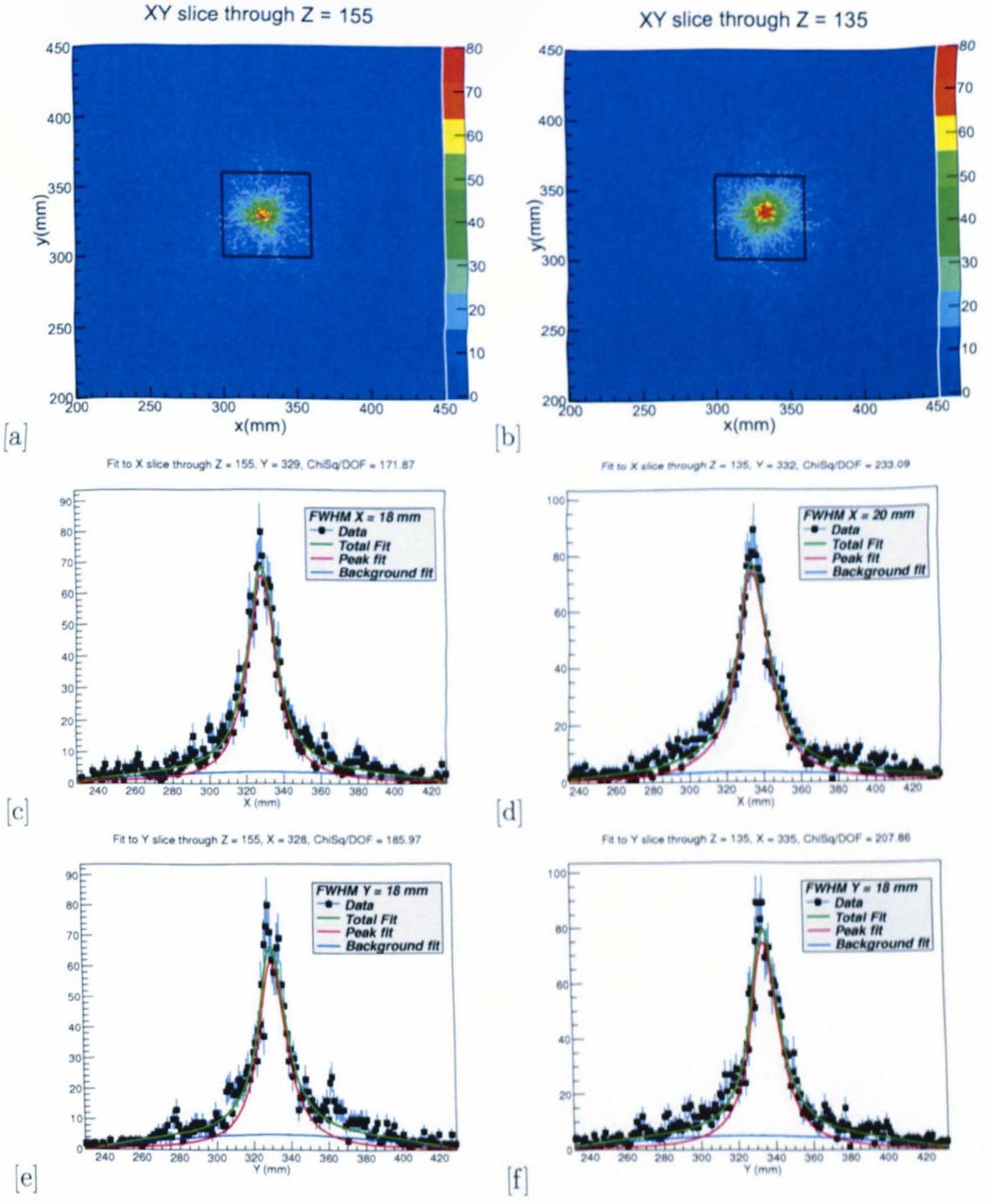

Figure 7.1: Simulated images and X,Y projections of a 5.110 MeV point source positioned 45mm from the scatter detector with X = Y = 30mm with a detector separation of 30mm. GeGe is [a],[c],[e]. GeCsI is [b],[d],[f].

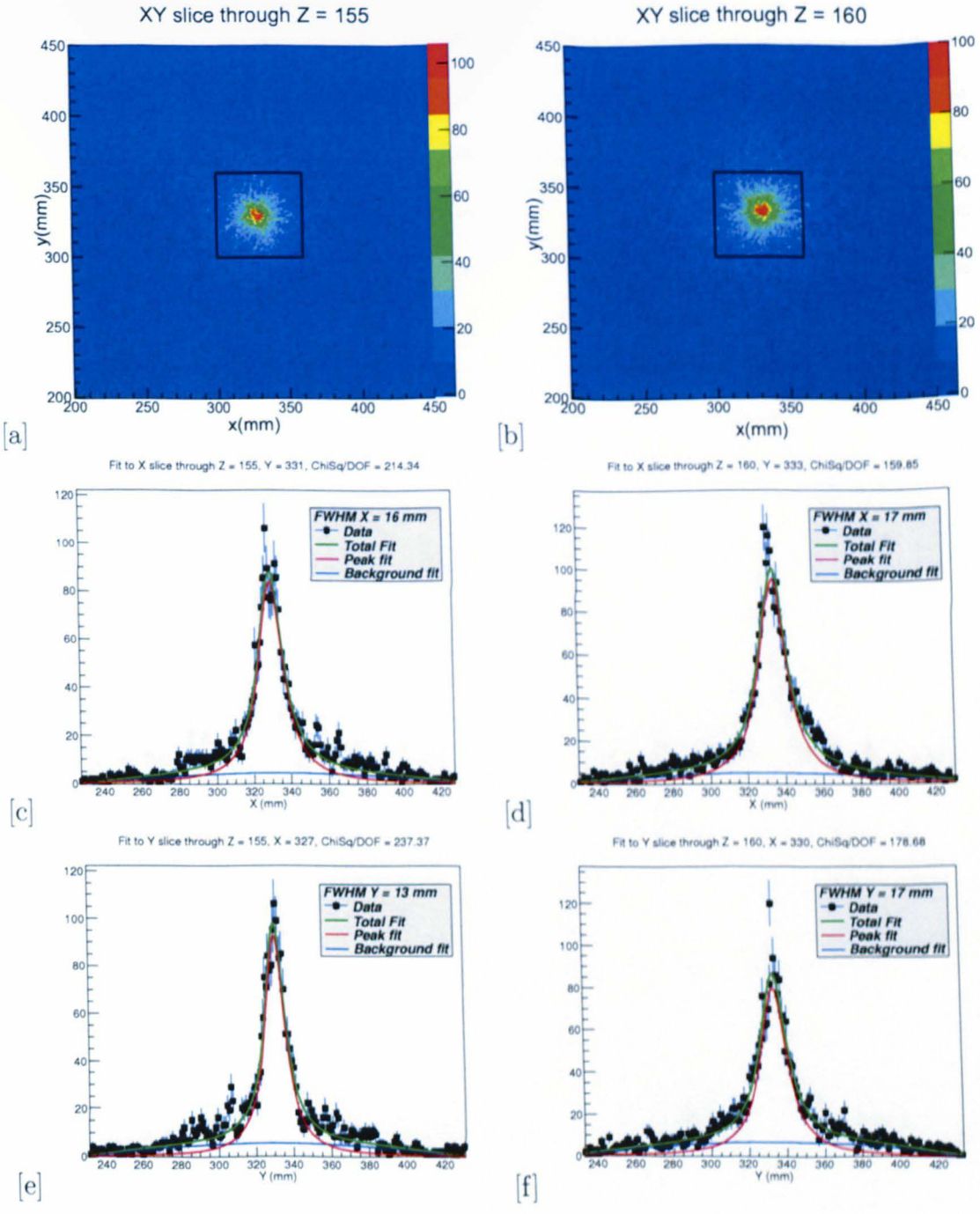

Figure 7.2: Simulated images and X,Y projections of a 5.110 MeV point source positioned 45mm from the scatter detector with X = Y = 30mm with a detector separation of 50mm. GeGe is [a],[c],[e]. GeCsI is [b],[d],[f].

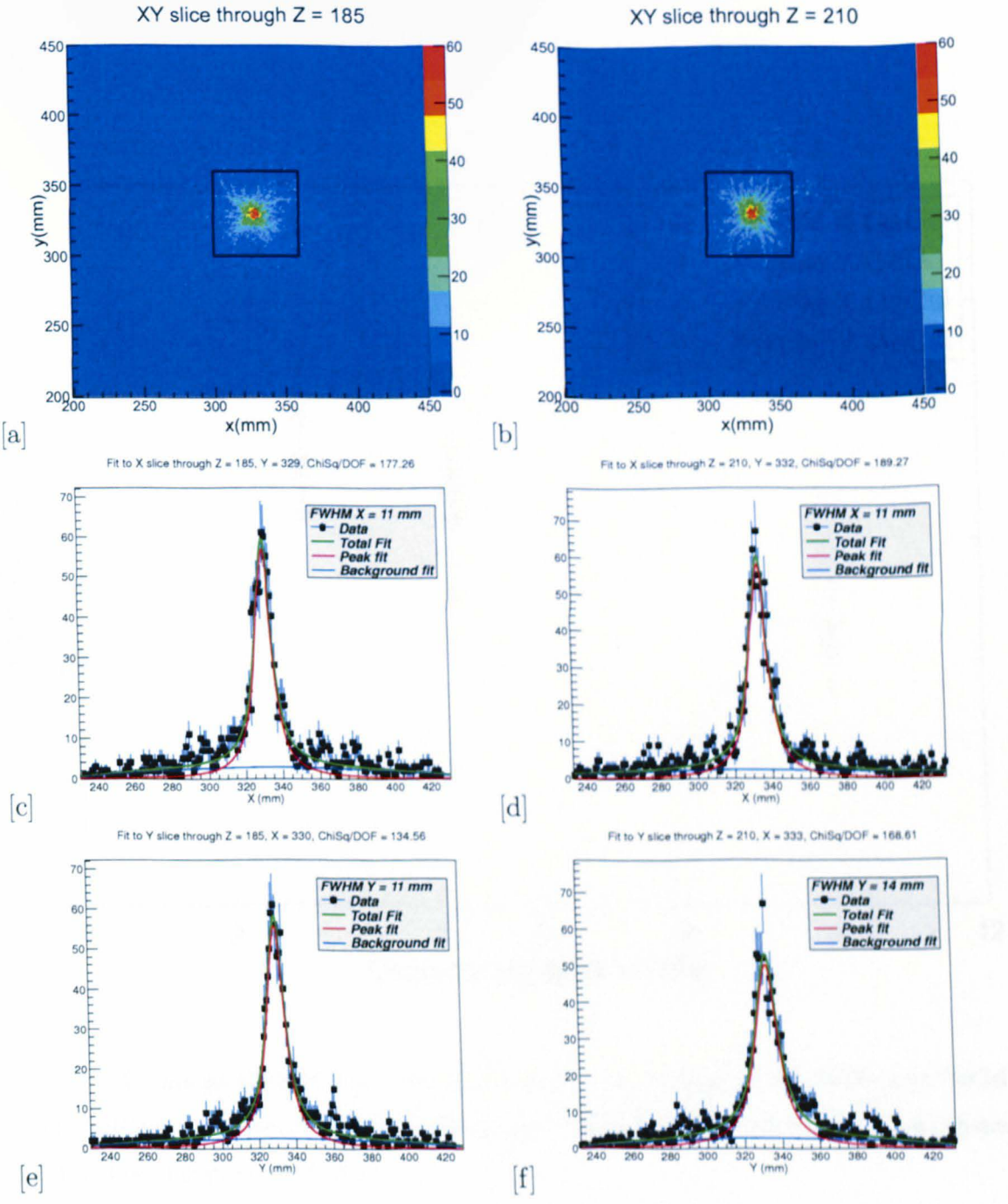

Figure 7.3: Simulated images and X,Y projections of a 5.110 MeV point source positioned 45mm from the scatter detector with X = Y = 30mm with a detector separation of 100mm. GeGe is [a],[c],[e]. GeCsI is [b],[d],[f].

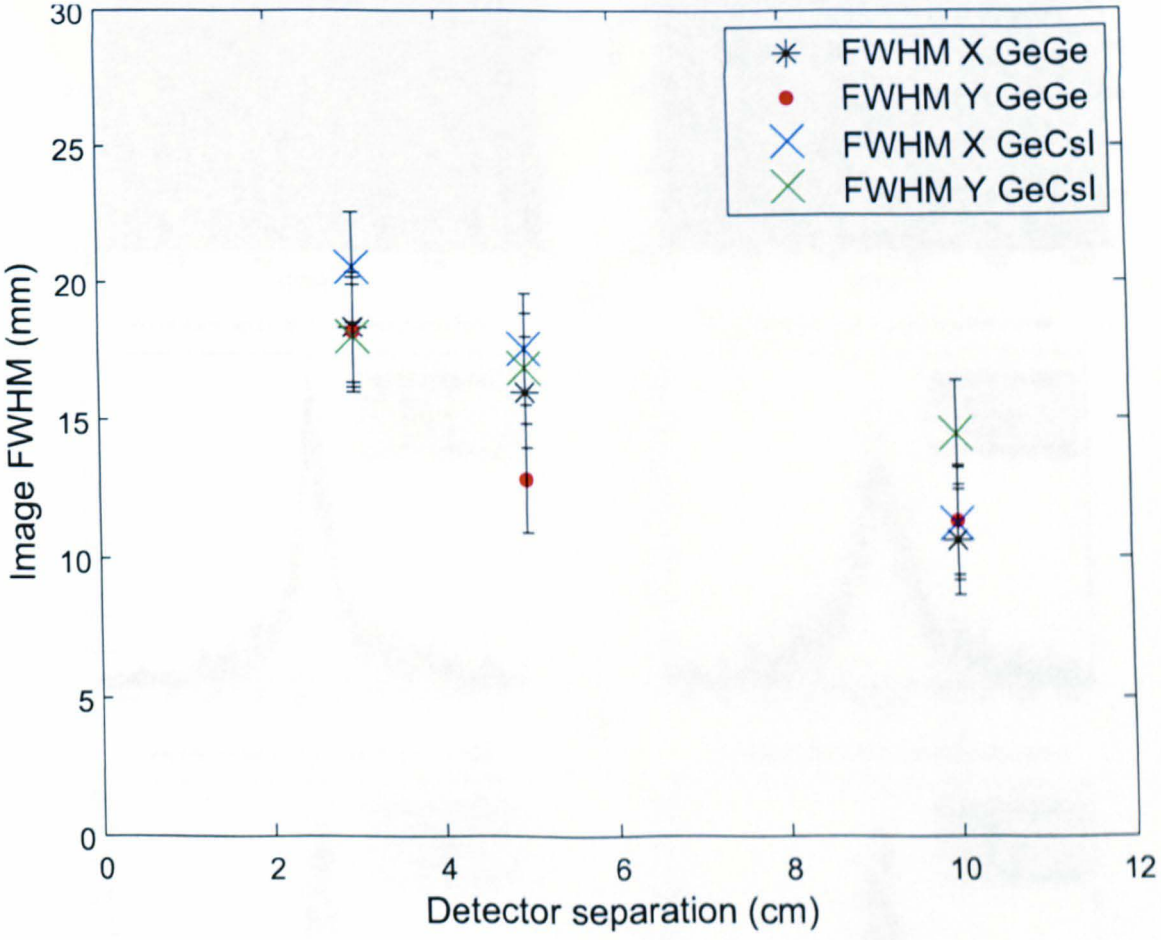

Figure 7.4: Image FWHM (mm) for the X and Y projections of the GeGe and GeCsI configurations. Given over the 30mm, 50mm and 100mm detector separations. The gamma point source energy is 5.110 MeV

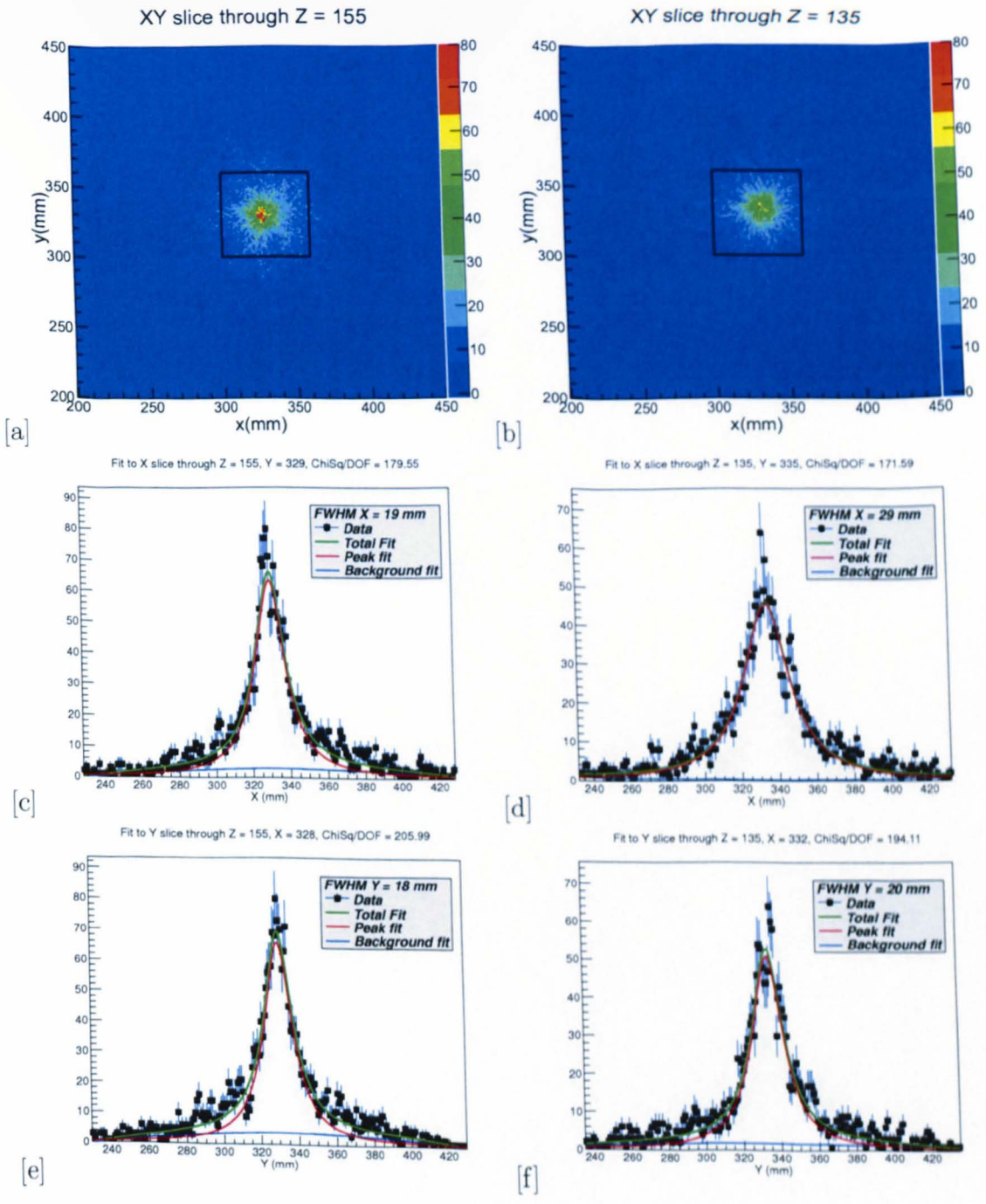

Figure 7.5: Simulated images and X,Y projections of a 6.130 MeV point source positioned 45mm from the scatter detector with X = Y = 30mm with a detector separation of 30mm. GeGe is [a],[c],[e]. GeCsI is [b],[d],[f].

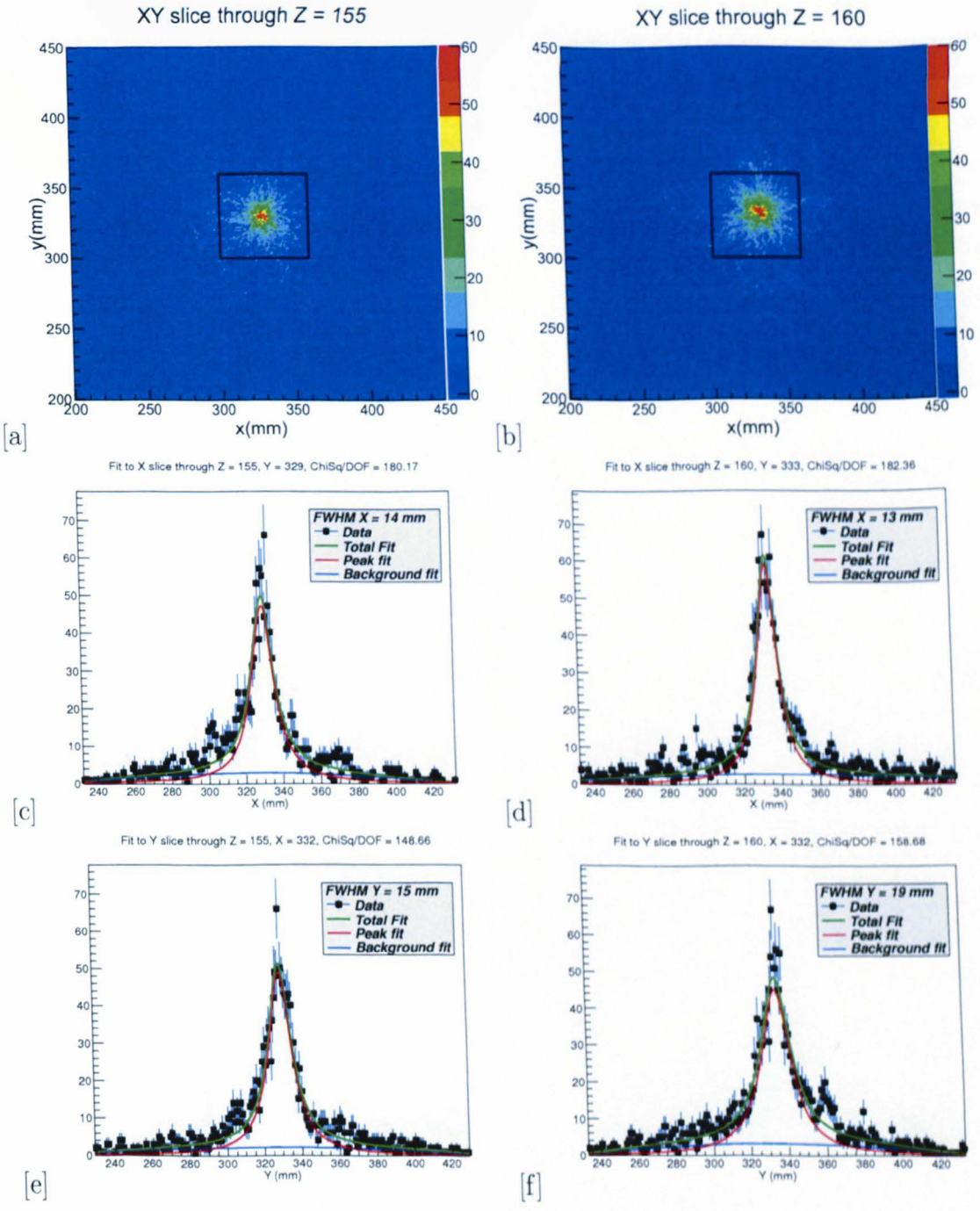

Figure 7.6: Simulated images and X,Y projections of a 6.130 MeV point source positioned 45mm from the scatter detector with X = Y = 30mm with a detector separation of 50mm. GeGe is [a],[c],[e]. GeCsI is [b],[d],[f].

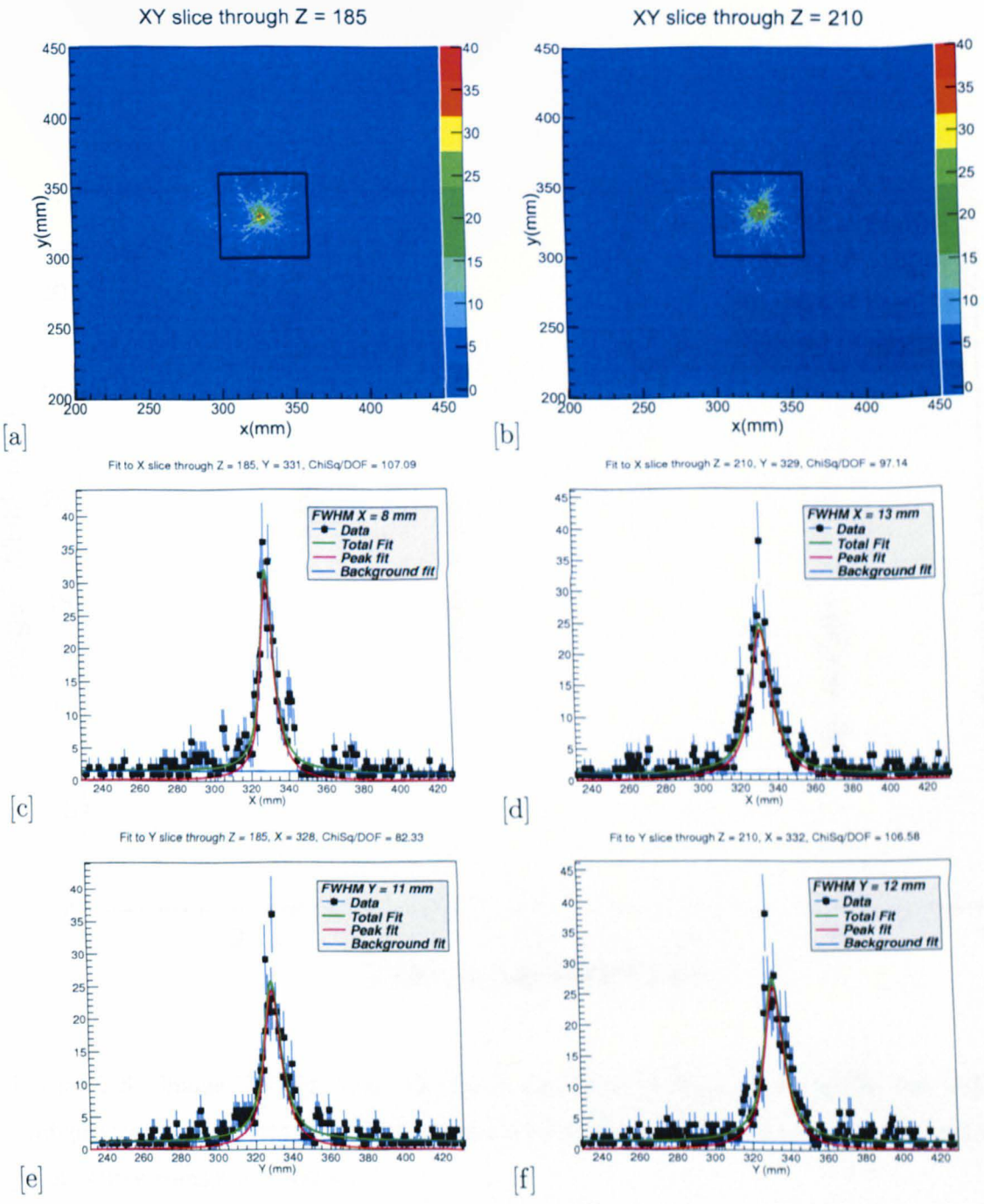

Figure 7.7: Simulated images and X,Y projections of a 6.130 MeV point source positioned 45mm from the scatter detector with X = Y = 30mm with a detector separation of 100mm. GeGe is [a],[c],[e]. GeCsI is [b],[d],[f].

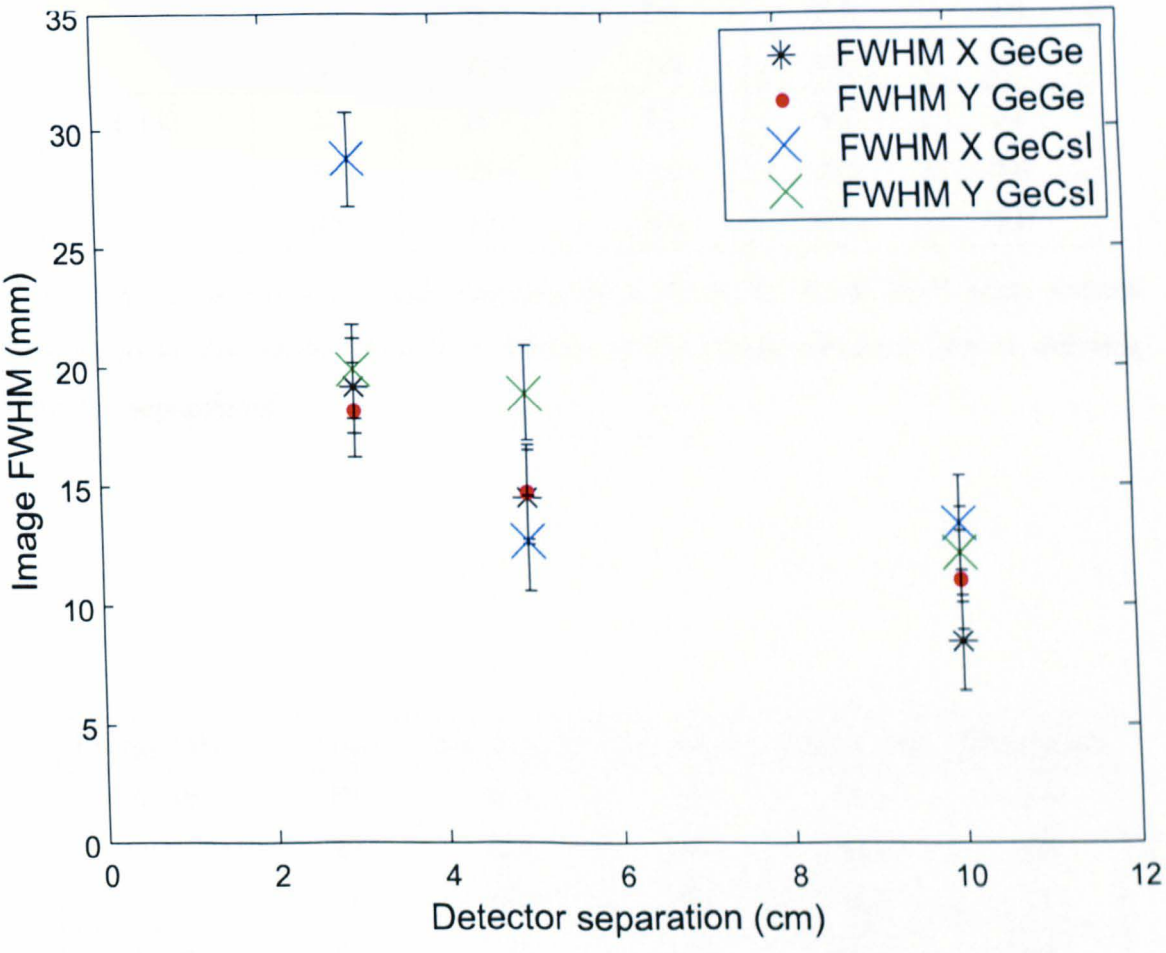

Figure 7.8: Image FWHM (mm) for the X and Y projections of the GeGe and GeCsI configurations. Given over the 30mm, 50mm and 100mm detector separations. The gamma point source energy is 6.130 MeV

Energy (MeV)	Sep(mm)	Rec X(mm)	Error(mm)	Rec Y(mm)	Error(mm)
5.110	30	28.7	2.0	30.9	2.0
	50	29.9	2.0	30.7	2.0
	100	30.4	2.0	30.1	2.0
6.130	30	28.7	2.0	29.7	2.0
	50	29.6	2.0	29.2	2.0
	100	29.6	2.0	30.2	2.0

Table 7.3: GeGe Reconstructed positions for 5.110 MeV - 6.130 MeV point sources positioned at the centre (X = Y = 30mm) of the scatter detector face at differing detector separations.

Energy (MeV)	Sep(mm)	Rec X(mm)	Error(mm)	Rec Y(mm)	Error(mm)
5.110	30	34.0	2.0	35.2	2.0
	50	33.8	2.0	33.6	2.0
	100	33.2	2.0	32.6	2.0
6.130	30	33.7	2.0	35.2	2.0
	50	33.0	2.0	33.8	2.0
	100	32.1	2.0	32.4	2.0

Table 7.4: GeCsI Reconstructed positions for 5.110 MeV - 6.130 MeV point sources positioned at the centre (X = Y = 30mm) of the scatter detector face at differing detector separations.

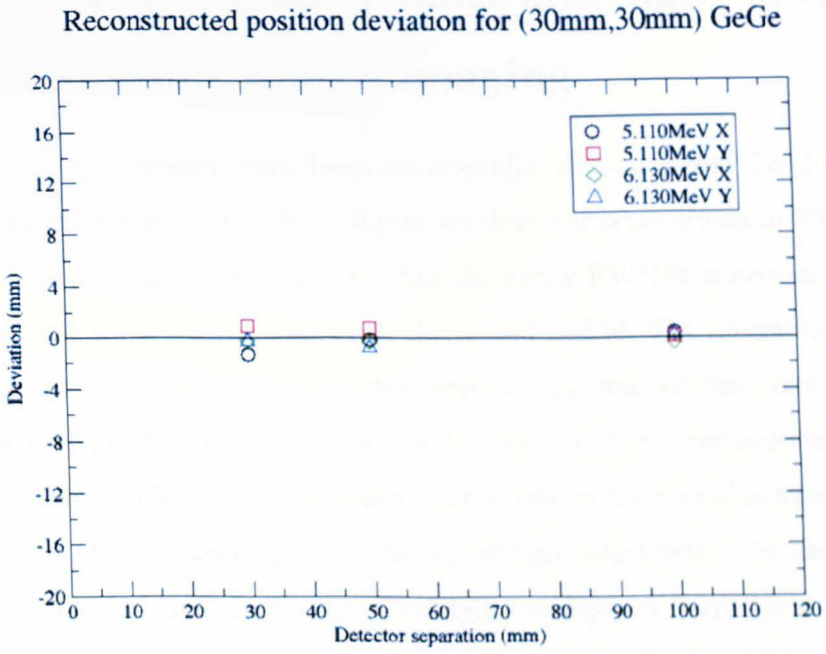

[a]

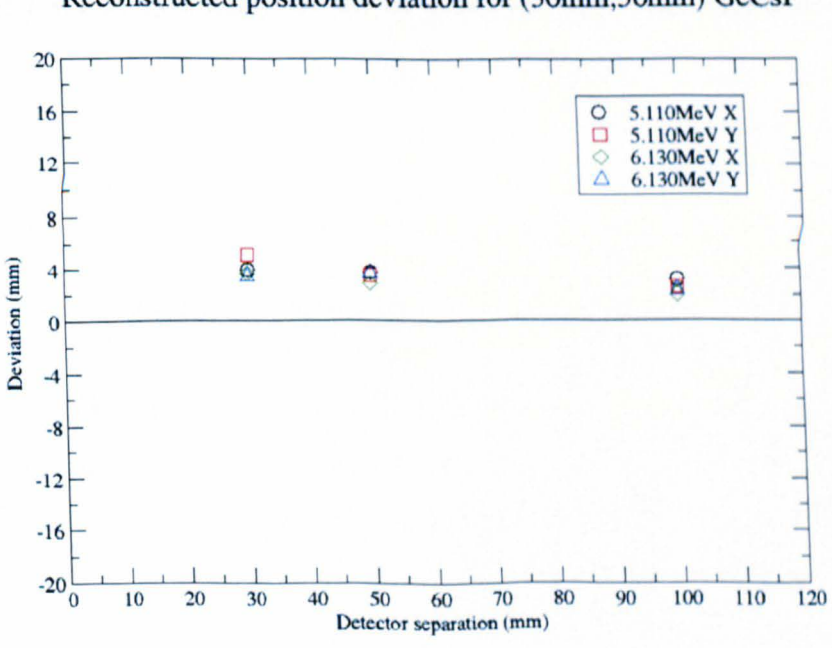

[b]

Figure 7.9: Reconstructed position deviation as a function of detector separation for 5.110 MeV to 6.130 MeV for GeGe [a] and GeCsI [b].

7.2 Summary of intermediate and high energy simulated point source imaging

Simulated Compton images have been successfully reconstructed for 1.640 MeV - 6.130 MeV point sources at X = Y = 30mm for detector separations of 30mm, 50mm and 100mm. For all simulations it is seen that the image FWHM improves generally as a function of detector separation for both GeGe and GeCsI. The interaction positions within the scatter and absorber detector governs the size of the cone apex angle and the image FWHM improvement is due to this. At the intermediate energies of 1.640 MeV - 4.430 MeV the images show a typically symmetrical shape throughout the varying detector separations with no significant degredation in image FWHM between the GeGe and GeCsI systems. The higher energies of 5.110 MeV - 6.130 MeV, particularly at shorter detector separation show a varying and asymmetric image FWHM. This is due to the lack of statistics at such high energies. An improvement in the image FWHM symmetry would be expected were there a larger number of events.

Chapter 8

Conclusions and future work

The main aims of this thesis were to assess the experimental image FWHM of a semiconductor Compton imaging device using the current image reconstruction algorithm, to investigate the image reconstruction limitations. Predominantly, the focus was a performance assessment of a novel Compton imaging device, where features such as Compton efficiency, event reconstruction and image resolution were determined experimentally. A deeper investigation was made possible by use of a dedicated GEANT4 simulation of the setup, where the performance of image reconstruction algorithms could be assessed and optimised.

8.1 Experimental results

Experimental images have been produced of 20,000 events using a simple back projection cone beam reconstruction algorithm, that has been developed by [Jud11]. This reconstruction code processes data faster than other existing Compton reconstruction codes.. It incorporates a fitting routine for a Lorentzian peak fit with a quadratic background fit, utilising a least squares minimisation fit to give a total peak fit for all X and Y projections throughout this work. The image FWHM of 0.662 MeV and 1.332 MeV point sources has been assessed as a function of increasing detector separation and it is concluded that it consistently improves but at a cost to efficiency.

The point sources were separately positioned at X = Y = 30mm across the scatter detector face. Both the point sources were also separately positioned at X = 10mm and Y = 50mm. Although there is an improvement in the image FWHM at both source positions as a function of detector separation, an image asymmetry was seen, more significantly at 100mm detector separation. It was not understood whether this was an experimental effect and so the same experimental source positions were carried out through Geant4 simulations. A 0.662 MeV point source was placed at X = Y = 30mm, X = 80mm and X = 130mm to assess the image reconstruction limitations and see how the image FWHM would vary as the source was positioned further away from the central position in X. The detectors were separated by 30mm and the source was positioned 95mm in Z from the scatter detector. It was found that as a function of position in X the image FWHM increased in both X and Y. The Compton images have been successfully reconstructed in the correct source positions and despite degradation of the X and Y projections' image FWHM, the images retain good clarity. The degradation in image FWHM in X and Y is due to a large possibility of scattering angles through the scatter detector which leads to an increased cone apex angle in producing any reconstructable images. This result suggests that the performance of the Compton imaging device is governed by the positioning of the source above the scatter detector. These results demonstrate show that not only is it possible to image successfully and efficiently a simple point source positioned in the centre of the scatter detector face, but also to reconstruct each of the sources in the correct positions when positioned across the scatter detector face.

8.2 Comparison to GEANT4 simulations

Dedicated GEANT4 simulations were performed to enable a more precide investigation of the GeGe experimental system. The system geometry was simulated to replicate the experimental geometry as closely as possible. A comparison of the Compton imaging performance when imaging with a 0.662MeV point source has been carried

out the image FWHM performance as a function of detector separation is shown in Figure 8.1.

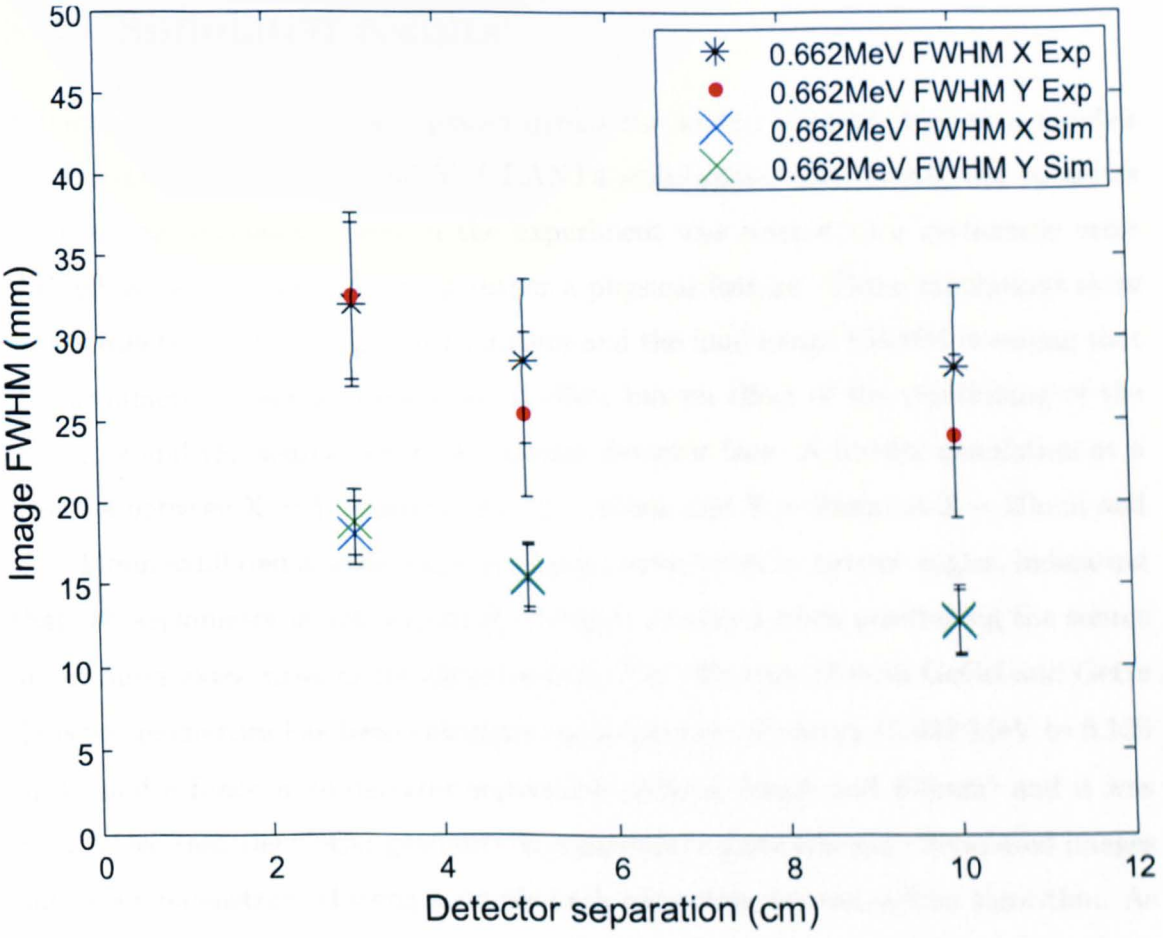

Figure 8.1: Image FWHM (mm) for the X and Y projections of the GeGe configurations both experimentally and simulated. Given over the 30mm, 50mm and 100mm detector separations. The gamma point source energy is 0.662 MeV

It is clear to see that the image FWHM of the experimental configuration is significantly worse than that of the image FWHM for the comparable simulation. This is due to the non exact definition of the interaction positions within the scatter and absorber detectors. Whereas throughout all of the simulated work, the exact interaction positions within the detectors is always defined. The experimental work used analogue electronics which means that an assumption is made on the interaction positions

introducing larger uncertainties and in turn, degrading the final image FWHM.

8.3 Simulated results

A 0.662MeV point source was placed across the scatter detector face at a number of different positions in X and Y. GEANT4 simulations were carried out to assess whether the asymmetry seen in the experiment was related to a systematic error within the experimental setup, or rather a physical feature. These simulations show an asymmetry in the reconstructed images and the final image FWHM revealing that the asymmetry is not an experimental effect but an effect of the positioning of the detectors and the source across the scatter detector face. A further simulation at a position between X = Y = 30mm and X = 10mm and Y = 50mm at X = 20mm and Y = 40mm exhibited a small amount of asymmetry even at narrow angles, indicating that the asymmetry is not restricted to events obtained when positioning the source at the outer extremities of the detector face. The efficiency of both GeCsI and GeGe detector geometries has been calculated as a function of energy (0.662 MeV to 6.130 MeV) and a function of detector separation (30mm, 50mm and 100mm) and it was clear to see that the GeCsI geometry is consistently more efficient. Simulated images have been reconstructed using a simple back projection reconstruction algorithm. As previously discussed, the GeCsI system was systematically more efficient throughout the simulations. These simulated results of image FWHM and reconstruction images show that even though the energy resolution of a CsI detector is worse than that of a Ge detector, it can be used as an absorber detector without too much degredation to the final image. It has been shown that images can be reconstructed at higher energies and the reconstruction position deviation is very minimal even at very low Compton efficiencies. At higher energies of 5.110 MeV and 6.130 MeV the image FWHM for both the GeGe and GeCsI systems show an asymmetry, (visible in the images) suggesting that there is a need for greater statistics to help improve the image quality. The GEANT4 simulated imaging results, comparing the GeGe and GeCsI systems

allow a conclusion that the GeCsI system is the preferred device for the project.

8.4 Future work

Higher statistic simulations need to be investigated at higher energies to be able to assess the full imaging ability of a GeCsI Compton imaging system. An in depth simulation of the different event types needs to be carried out and an assesment of the possible increase in Compton efficiency from 1:1 Compton events to 1:2 Compton events needs to be addressed and how these events affect the image FWHM performance. Another prospect could be to use GEANT4 event biasing. [GEANT4]. The image FWHM performance in experimental imaging shows there is a need for improvement when trying to identify as closely as possible the exact interaction positions within the scatter and absorber detectors. This can be developed by utilising parametric Pulse Shape Analysis (PSA) which will help define more accurately the interaction positions within a semiconductor device. Further simulations of recently developed scintillator materials such as LaBr [Kur10] and GYGAG(Ce) [Che11], along with a full array imaging system as opposed to just one single imaging device.

Bibliography

[Ago03] S. Agostinelli. "'GEANT4 - a simulation toolkit". Nucl. Instr. and Meth. in Phys. Res. A, vol. 506, pp. 250-303. (2003).

[Ang64] H. Anger. "Scintillation Camera with Multichannel Collimators", Journal of Nuclear Medicine 5:515-531, (1964).

[Che11] N.J. Cherepy. "Scintillator Materials", Lawrence Livermore National Laboratory. LLNL-PRES-469519. (2011)

[Eng80] Ralph. W. Engstrom. "Photomultiplier Handbook", RCA/Burle, (1980).

[Cha04] S. Chauvie et al. "Geant4 low energy electromagnetic physics". IEEE Trans. Nucl. Sci. 3 1881 (2004).

[Cha07] S. Chauvie. "Geant4 physics processes for microdosimetry simulation: design foundation and implementation of the first set of models". IEEE Transactions on Nuclear Science, Vol. 54, 2619-2628. (2007).

[Coo07] R.J. Cooper. "Performance of the SmartPET Positron Emission Tomography System for Small Animal Imaging". PhD Thesis. The University of Liverpool. (2007).

[Coo08] R.J. Cooper et al. "Charge collection performance of a segmented planar high-purity germanium detector". Nucl. Instr. and Meth. A, Vol.595, 401-409. (2008).

[Du01] Y.F. Du et al., Nucl. Instr. and Meth. A, Vol. 475, 203-211 (2001).

[Eve77] D. B. Everett, J. S. Fleming, R. W. Todd, and J. M. Nightingale, "Gamma-radiation imaging system based on the Compton effect", Proc. ZEE, Vol. 124, pp. 995-1000, (1977).

[Far07] M. Farahmand et al. "Detection of explosive substances by tomographic inspection using neutron and gamma-ray spectroscopy", NIMB 261 396-400. (2007).

[Gas09] IEEE tranasction on nuclear science, Vol. 56, No.3. (2009).

[GEANT4] http://geant4.cern.ch

[Goz94] T. Gozani, "Novel applications of fast neutron interrogation methods", Nucl. Instr. and Meth. A. 353 (1994) 635.

[Gur95] S.V. Guru et al., IEEE transaction on nuclear science, Vol, 42, No4. (1995).

[Gur96] S.V. Guru et al., Nucl. Instr. and Meth. A, Vol. 378, 612-619 (1996).

[Har09] L.J. Harkness. "Development of a ProSPECTus Semiconductor Compton Camera for Medical Imaging". IEEE medical imaging conference record. (2009).

[Har10] L.J. Harkness. "A Design Study of the Semiconductor Sensor Head for the ProSPECTus Compton Camera". PhD Thesis. University of Liverpool. (2010).

[Jud11] Analytical Image reconstruction algorithm. The University of Liverpool. Developed 2011.

[Kam03] T. Kamae. "GLAST Large Area Telescope - daily survey of high energy sky". Nucl. Phys. B - Proceedings Supplments, vol. 125, pp. 179-186. (2003).

[Kir09] A.E. Kiryunin. "GEANT4 physics evaluation with testbeam data of the ATLAS hadronic end-cap calorimeter" J. Phys.: Conf. Ser. 160 012075 doi: 10.1088/1742-6596/160/1/012075. (2009).

[Kit76] Introduction to Solid State Physics, Fifth Edition, C. Kittel (1976).

[Kno00] G.F. Knoll, "Radiation detection and measurement", third edition, (2000).

[Kur10] S. Kurosawa et al., "Development of an 8x8 array of LaBr3(Ce) scintillator pixels for a gaseous Compton gamma-ray camera", Nucl. Instr. and Meth. in Phys. Res. A, vol. 623 pp. 249-251. (2010).

[Leh03] C.E. Lehner et al., IEEE Transactions on nuclear science, Vol, 50, No4. (2003).

[Len08] M. Lenti. "A 3-D imaging device using Compton scattering off the body". Nucl. Instr. and Meth. in Phys. Res. A, vol. 588 pp. 457-462. (2008).

[Lut01] G. Lutz, "Semiconductor Radiation Detectors, Device Physics", (2001).

[MATLAB] http://mathworks.co.uk

[Midas] http://npg.dl.ac.uk/MIDAS/

[Mih09] L.Mihailescu et al., IEEE transactions on nuclear science, Vol, 56, No2 (2009).

[NIST] http://physics.nist.gov/PhysRefData/Xcom/Text/XCOM.html

[NUC] http://www.nucsafe.com

[Ord97] Ordonez et al., Doppler broadening of energy spectra in Compton cameras, Proceedings of IEEE Nuclear Science Symposium, Vol. 2, 1361-1365 (1997).

[Ott75] G. Ottaviani. "Charge carrier transport properties of semiconductor materials suitable for nuclear radiation detectors", IEEE Transactions on Nuclear Science, Vol. Ns-22, 192-204. (1975).

[Oxl10] D.C. Oxley. "A Quantitative Assessment of the Performance of a Planar Germanium Detector for PET Imaging". PhD Thesis. The University of Liverpool. (2010).

[ROOT] Root Analysis Package, CERN, http://www.root.cern.ch/root/doc/RootDoc.htm

[Ryn99] J. Rynes. "Gamma ray and neutron radiography as part of a pulsed fast neutron analysis inspection system". Nucl. Instr. and Meth. in Phys. Res. A, vol. 422 pp. 895-899. (1999).

[Sca01] L. Scarsi. "The extreme universe of cosmic rays: Observations from space". Il Nuovo Cimento C, vol. 24, pp. 471-482. (2001).

[Sch93] V. Schonfelder. "Instrument description and performance of the imaging gamma-ray telescope Comptel aboard the Compton gamma-ray observatory". The Astrophysical journal supplement series. 86:657-691. (1993).

[SCIONIX] www.scionix.nl

[Scr07] D.P. Scraggs. "Digital signal processing techniques for semiconductor Compton cameras". PhD Thesis. The University of Liverpool. (2007).

[Sze02] Semiconductor Devices Physics and Technology, 2nd Edition, S.M. Sze (2002).

[Tod74] R.W. Todd. "A Proposed gamma camera". Nature Vol. 251. (1974).

[Vet00] K. Vetter et al., Nucl. Instr. and Meth. A, Vol. 452, 223 (2000).

[Vet07] K. Vetter, M. Burks, C. Cork, M. Cunningham, D. Chivers, E. Hull, T. Krings, H. Manini, L. Mihailescu, K. Nelson, D. Protic, J. Valentine and D. Wright, "High-sensitivity Compton imaging with position-sensitive Si and Ge detectors". Nucl. Instr. Meth. A 579 363. (2007).

[Vou01] G. Vourvopoulos, P.C. Womble. "Pulsed Fast/Thermal Neutron Analysis: A Technique for Explosives detection". Talanta 54 459-468, Elsevier. (2001).

[Wah11] C.G. Wahl., IEEE transaction on nuclear science, Vol, 58, No3. (2011).

[Zen01] G.L. Zeng., "Image reconstruction - a tutorial", Computerized Medical Imaging and Graphics 25, 97-103. (2001).